The Dissertation Committee for Zhen Wei Certifies that this is the approved version of the following dissertation:

Spin-Transfer-Torque Effect in Ferromagnets and Antiferromagnets

Committee:

Maxim Tsoi, Supervisor

Zhen Yao

John Markert

Xiaoqin Li

Paulo Ferreira

Spin-Transfer-Torque Effect in Ferromagnets and Antiferromagnets

by

Zhen Wei, B.S.

Dissertation

Presented to the Faculty of the Graduate School of
The University of Texas at Austin
in Partial Fulfillment
of the Requirements
for the Degree of

Doctor of Philosophy

The University of Texas at Austin
December 2008

To my wife and parents

Acknowledgments

I would like to sincerely thank my advisor Maxim Tsoi who deeply motivated me to strive harder and reach higher. He gave me tremendous support and invaluable advice for me to finish the graduate study. I have benefited a lot from his continuous encouragement. I am also very impressed by his diligence and enthusiasm for the scientific pursuit. It was very fortunate for me to join his group and his advice will continue to guide me throughout the career.

I would also like to acknowledge our group members Dr. Carl Knutson and Brian O’Gorman. They gave me great support for my research. I specially thank Brian O’Gorman for reading my dissertation and providing invaluable suggestions. Also I thank Dr. Kang Luo, Dr. Junwei Huang, and Dr. Wei Lu for their help over the years. Thanks as well go to my three best friends: Hualiang Shi, Yiwei Cai and Jinze Qiu, for all the happy hours with them. I must also acknowledge Dr. Jack Bass and Amit Sharma at Michigan State University. They helped me to make thin film samples and gave great comments on my projects.

Finally I would thank my wife Shu Chen and my parents for all their love, understanding and support during my time at UT.

Spin-Transfer-Torque Effect in Ferromagnets and Antiferromagnets

Publication No._____________

Zhen Wei, Ph.D
The University of Texas at Austin, 2008

Supervisor: Maxim Tsoi

Spintronics in metallic multilayers, composed of ferromagnetic (F) and non-magnetic (N) metals, grew out of two complementary discoveries. The first, Giant Magnetoresistance (GMR), refers to a change in multilayer resistance when the relative orientation of magnetic moments in adjacent F-layers is altered by an applied magnetic field. The second, Spin-Transfer-Torque (STT), involves a change in the relative orientation of F-layer moments by an electrical current. This novel physical phenomenon offers unprecedented spatial and temporal control over the magnetic state of a ferromagnet and has tremendous potential in a broad range of technologies, including magnetic memory and recording.

Because of its small size (<10nm), point contact is a very efficient probe of electrical transport properties in extremely small sample volumes yet inaccessible with other techniques. We have observed the point-contact excitations in magnetic multilayers at room temperature and extended the capabilities of our point-contact technique to include the sensitivity to wavelengths of the current-induced spin waves.

Recently MacDonald and coworkers have predicted that similar to ferromagnetic multilayers, the magnetic state of an antiferromagnetic (AFM) system can affect its transport properties and result in antiferromagnetic analogue of giant magnetoresistance (GMR) = AGMR; while high enough electrical current density can affect the magnetic state of the system via spin-transfer-torque effect. We show that a high density dc current injected from a point contact into an exchange-biased spin valve (EBSV) can systematically change the exchange bias, increasing or decreasing it depending on the current direction. This is the first evidence for current-induced effects on magnetic moments in antiferromagnetic (FeMn or IrMn) metals.

We searched for AGMR in multilayers containing different combinations of AFM=FeMn and F=CoFe layers. At low currents, no magnetoresistance (MR) was observed in any samples suggesting that no AGMR is present in these samples. In samples containing F-layers, high current densities sometimes produced a small positive MR – largest resistance at high fields. For a given contact resistance, this MR was usually larger for thicker F-layers, and for a given current, it was usually larger for larger contact resistances (smaller contacts). We tentatively attribute this positive MR to suppression at high currents of spin accumulation induced around and within the F-layers.

Table of Contents

List of Tables

List of Figures

Chapter 1

Introduction

1.1 Ferromagnetism and Antiferromagnetism

The magnetic moments in atoms originate from the angular momenta of their unpaired electrons. There are two momenta contributing to the electronic angular momenta: orbital angular momentum and electron spin momentum. From quantum mechanics, the electron has orbital quantum number $\boldsymbol{L}$, spin quantum number $\boldsymbol{S}$, and the total angular momentum is $\boldsymbol{J}=\boldsymbol{L}+\boldsymbol{S}$. From Hund's rule, the spin momentum $\boldsymbol{S}$ should be maximized in order to minimize the energy at specific orbital number $\boldsymbol{L}$. At the same time, Pauli's principle forbids two electrons from having the same quantum numbers. So electrons with parallel spins have to avoid each other and lower the coulomb repulsion between them. This results in a non-zero spin momentum for an individual atom.

The magnetic materials are those formed from atoms which have nonzero magnetic moments. The two types of magnetic materials which will be considered in this thesis are ferromagnets and antiferromagnets.

Magnetic materials can be either ferromagnetic or antiferromagnetic due to exchange interaction, an interaction of electrostatic origin that results from the indistinguishability of the electrons in the incomplete shells. This interaction may be of short range (direct exchange interaction) or of long range (indirect exchange interaction). Heisenberg generalized the atomic exchange interaction and developed the very powerful Heisenberg Hamiltonian to describe magnetic interactions by explicitly coupling pairs of spins or atomic moments. In the Heisenberg Hamiltonian, the exchange integral, J_{ex}, is positive for the ferromagnetic (parallel) coupling and negative for antiferromagnetic (antiparallel) coupling. For direct inter-atomic exchange, the atomic moments are close and have sufficient overlap of their wave functions. Then the sign of the exchange integral J_{ex} is determined by the competing Coulomb and kinetic energies. Figure 1.1 shows the Bethe-Slater curve which represents the magnitude of the direct exchange as a function of interatomic distance. Here, r_a is the interatomic distance, which is the distance between two nearby atoms. The orbital radius for 3d electrons is r_{3d}. Fe, Co and Ni have a positive exchange integral, which is why they are ferromagnetic. Mn has negative exchange integral and is antiferromagnetic.

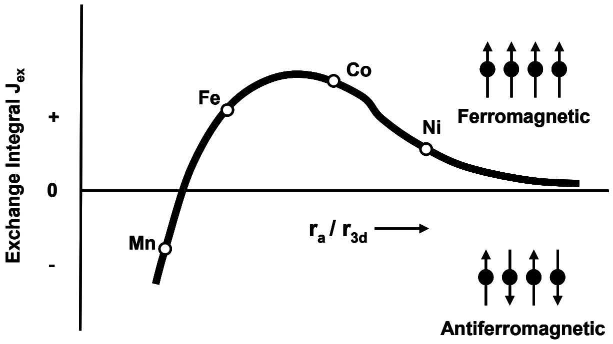

Figure 1.1 Bethe-Slater curve.

Ferromagnetism is characterized by a spontaneous parallel alignment of atomic magnetic moments. This order disappears when temperature rises above a certain point, called the *Curie temperature*. Below this temperature, the magnetic interactions overcome thermal agitation and show a *spontaneous magnetization* in the absence of an applied magnetic field. Despite the spontaneous magnetization, a piece of ferromagnetic material may not be fully magnetized. This is because of the existence of magnetic domains. Each domain contains a large number of atoms that are spontaneously magnetized. However magnetization directions of individual domains can vary and result in zero net magnetization of a multi-domain sample. Under the influence of an applied magnetic field, the distribution of domains can change and the sample magnetization can be saturated at high enough field. This magnetization saturation process is not reversible and causes a hysteresis loop in the magnetization curve (magnetization vs field), which is a characteristic of ferromagnetic materials.

The most widely used simple ferromagnetic materials are iron Fe, cobalt Co and nickel Ni. They are called transition metals because their atoms have incomplete d sub-shells. In transition metals, 3d electrons are responsible for magnetism, while 4s electrons give a smaller contribution [1]. We can calculate the expected magnetic moments for a transition metal by considering both the spin and orbital magnetic moments. Based on the occupation of 3d shells, Table 1.1 lists the angular momenta $S = \left|\sum s_z\right|, L = \left|\sum l_z\right|$ and $J = L + S$ from Hund's rules. The total magnetic moment due to the 3d shell electrons is $m_{J_z} = g_J J \mu_B$, where g_J is the Lande g-factor. We use the convention $s_z = +1/2 = \uparrow$ and $s_z = -1/2 = \downarrow$.

*moments are in units of [μ_B]

metal	$m_l \rightarrow$	+2	+1	0	-1	-2	***S***	***L***	***J***	g_J	m_{Jz}^{*}
Fe	d^6	↑↓	↓	↓	↓	↓	2	2	4	3/2	6
Co	d^7	↑↓	↑↓	↓	↓	↓	3/2	3	9/2	4/3	6
Ni	d^8	↑↓	↑↓	↑↓	↓	↓	1	3	4	5/4	5

Table 1.1 Occupation of 3d orbitals with quantum numbers m_l for d^6(Fe), d^7(Co) and d^8(Ni) [2].

From this localized magnetic moment calculation, we can see the atomic moments for transition metals are integers. However, from the measured spontaneous magnetization, M, in Fe, Co and Ni, the atomic moments m =2.216 for Fe, 1.715 for Co, and 0.616 for Ni. Comparing these experimental results of odd fractions with spin moments and orbital moments, we find that the 3d electrons are not strictly localized and the orbital moments are severely overestimated. Indeed, when we put the isolated atoms together to form a transition metal, the originally sharp atomic energy states are broadened and become quasi-continuously distributed. So in a transition metal, the 3d electrons or itinerant electrons are actually located in energy bands and affected by the bonding in the metallic lattice of the crystal.

Around 1935, Mott [3], Slater [4, 5], and Stoner [6, 7] developed the band theory to explain ferromagnetic metal properties. This band-like model for ferromagnetic metals is called the Stoner model. The Stoner model assumes that the interaction between 3d electrons causes a smearing of energy into a band. Electrons with two different spin directions, which are usually called spin-up and spin-down states, fill the energy states up to Fermi energy, E_F at T=0 K. As shown in Figure 1.2, in an external magnetic field, the electrons in the area of the shaded region in the spin-down subbands transfer to the top of spin-up subbands. The spin-up subbands with larger electrons population are called *majority band* and spin-down subbands with smaller population are *minority band*. This energy band shift or asymmetry of spin states causes the magnetization. From Pauli's principle, two electrons with opposite spin states will on average repel each other more than two electrons with the same spins, because latter feel each other less due to the inhibition for them to be in the same energy state. The Stoner model postulates repulsion between electrons with opposite spins is larger than that with the same spins by an amount, **U**. Then the interaction energy between electrons is of the form $UN_{\uparrow}(E)N_{\downarrow}(E)$, where $N_{\uparrow}(E)$ and $N_{\downarrow}(E)$ are the density of electron states for the two spin directions. The change of total energy includes the change of kinetic energy $\Delta E_k = N(E_F)(\delta E)^2$ and interaction energy $\Delta E_i = -UN^2(E_F)(\delta E)^2$. So the total energy change is:

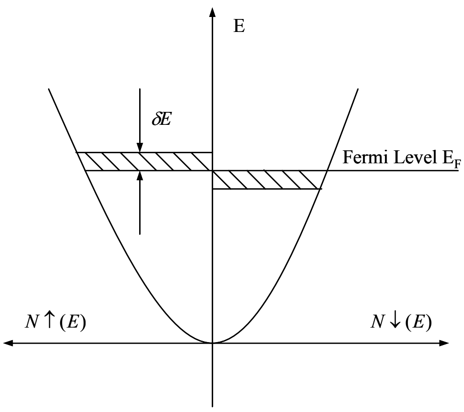

Figure 1.2 Density of states for electrons with spin ↑and spin ↓.

$$\Delta E = N(E_F)(\delta E)^2[1 - UN(E_F)] \tag{1.1}$$

where δE is the energy band displacement, which indicates how strong the ferromagnetism is. From the more realistic density of states, the calculated energy shifts is about 2.2eV in Fe, 1.7eV in Co and 0.6eV in Ni [8].

If $1\text{-}UN(E_F)>0$, then ΔE is minimum for zero magnetization ($\delta E=0$). It's in a nonmagnetic state. If $1\text{-}UN(E_F)<0$, then ΔE is minimum for nonzero magnetization ($\delta E\neq 0$). It has a different number of spin-up and spin-down electrons, which implies ferromagnetism. The condition of $1\text{-}UN(E_F)<0$ is the very famous *Stoner criterion* for ferromagnetism. From this condition, we see that ferromagnetism is favored for strong electron interactions (large U) and high density of states $N(E_F)$ at the Fermi level. Overall, the Stoner model very successfully predicted some magnetic properties of transition metals.

Unlike ferromagnetism, antiferromagnetism is a state in which the atomic magnetic moments are ideally aligned but the individual moments are equal and opposite, or self-compensated. So the overall spontaneous magnetization is zero. Antiferromagnetism occurs when the exchange interaction is negative which arranges the neighboring magnetic moments antiparallel. This interaction is strong and works against the external magnetic field which would tend to align all the moments parallel. Néel was the first to show that an antiferromagnetism system has a critical temperature, called the Néel temperature (T_N), above which the moments are disordered paramagnetically as in a ferromagnet above the Curie temperature.

One of the most important applications of antiferromagnets in spintronic devices is to induce the exchange bias at an interface with a ferromagnetic thin film, which will be discussed in detail in Chapter 4.

1.2 Giant Magnetoresistance (GMR)

Magnetoresistance (MR) is the change in electrical resistance of a conductor in the presence of an applied magnetic field. For instance, a well known magnetoresistive effect in ferromagnetic conductors is anisotropic MR = AMR. It was found that resistance of a ferromagnetic conductor depends on the angle between its magnetization and an applied electric current. Usually, when the magnetization vector is parallel to the current's direction, the resistance is highest and when they are perpendicular the resistance is lowest.

Today many different magnetoresistive effects are known, such as giant magnetoresistance [9, 10], tunnel magnetoresistance [11], colossal magnetoresistance [12], and ballistic magnetoresistance [13]. Among them, giant magnetoresistance (GMR) is the most famous for its tremendous applications in magnetic memory technology. In most of the experiments presented throughout this thesis, the GMR effect is the main experimental tool for detecting magnetic dynamics and configuration in our systems.

Giant magnetoresistance was first discovered in Fe/Cr multilayers independently by Fert [9] and Grünberg [10] in 1988. For this great contribution to science, they were awarded the 2007 Nobel Prize in Physics. The main observation in these multilayers was that with a magnetic field aligning the relative magnetization directions of the constituent Fe layers, the resistance of the multilayer decreases dramatically. The magnetoresistance curves at 4.2K for Fe/Cr multilayers are shown in Figure 1.3. At zero applied magnetic field, the neighboring Fe layers are coupled antiferromagnetically (antiparallel) for a certain Cr thickness and the resistance is highest. The saturation field H_s is the field required to overcome the interlayer coupling between Fe layers and align their magnetizations parallel to each other, and here the resistance drops to lowest value. The GMR is usually defined as the ratio of the resistance change to the resistance in parallel configuration: $GMR = \frac{R_{AP} - R_P}{R_P}$. From the experimental results in various systems, the magnitude of GMR can vary from a few percent to 220% [14].

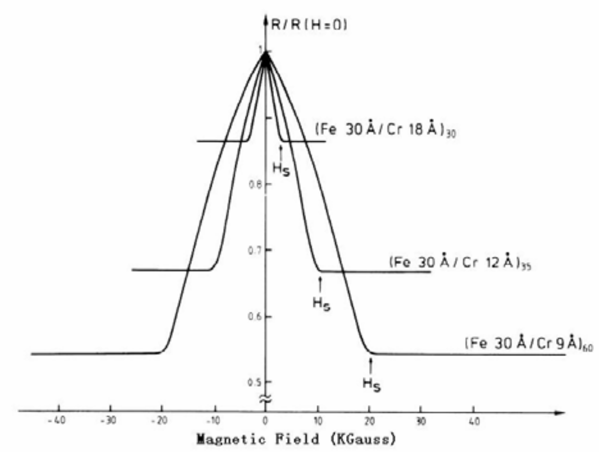

Figure 1.3 Magnetoresistance curves at 4.2K for Fe/Cr multilayers [9]. The current and magnetic field are parallel to the plane of the film.

The discovery of GMR has triggered extensive experimental and theoretical studies. Right after the first observation, Parkin et al. [15] succeeded in reproducing similar GMR in Co/Ru, and Co/Cr multilayers with sputtered polycrystalline samples. Parkin [16] and Mosca [17] also extensively studied the GMR oscillations where the GMR effect exists for antiferromagnetic interlayer coupling and vanishes when the coupling is ferromagnetic depending on the nonmagnetic spacer thickness. GMR effects have been observed not only in exchange coupled magnetic multilayers but also in other structures, such as uncoupled multilayers combining soft and hard magnetic layers to give different switching fields [18. 19], multilayered nanowires [20], and well known spin-valve structures [21]. We will describe in detail the spin-valve structure and its magnetoresistance curve in Chapter 4.

In the simple picture for understanding GMR, the first concept to know is the two-current model for conduction in ferromagnets. In 1936, Mott [22] assumed that in transition metals the s-electrons carry the electric current and the electrical resistance is due to the scattering processes when electrons jump from an s-band to d-band. For those with more d-band states available, there is stronger scattering and higher resistance. In 1968, Fert explicitly introduced the idea of a two current model [23]. At low temperature, no magnons are excited and the spin-flip scattering is negligible. Hence the s-band electrons with majority spin (up) and minority spin (down) will jump to the d-states of the same spin selectively without mutual interaction. As a result, spin up and spin down electrons carry the current independently and in parallel. The total resistivity of a ferromagnet from spin-dependent scattering can be expressed as $\rho = \frac{\rho_{\uparrow}\rho_{\downarrow}}{\rho_{\uparrow}+\rho_{\downarrow}}$, where $\rho_{\uparrow}$ is the resistivity for spin up channel and $\rho_{\downarrow}$ for spin down channel. At high temperatures, there is electron-magnon scattering, which will transfer momentum between the two current channels, called spin-mixing. Therefore the spin-mixing resistivity, $\rho_{\uparrow\downarrow}$, should be introduced that results in a more general expression for the total resistivity [24].

In ferromagnets the scattering probability is proportional to the density of vacant d-states. Generally the electrons with majority spin have less vacant d-states and minority electrons have more d-states available. Figure 1.4 illustrates GMR from spin-dependent scattering for two current channels. We consider the simplest structure with two ferromagnetic layers (F) separated by a non-magnetic spacer (N). When the external magnetic field aligns the two magnetizations of the F layers, the electrons with majority spin have less scattering in both layers while the minority electrons are scattered strongly in both layers. So in the equivalent resistance network, two series smaller resistances r (majority spin resistance) are parallel with two series bigger resistances R (minority spin resistance). The resulting total resistance for a parallel configuration is $R_P = \frac{2rR}{r+R}$. When the two F magnetizations are in an antiparallel state, the electrons with majority and minority spins are scattered strongly in alternate F layers. So in the resistance network, they both give one small resistance r and one big resistance R. The total resistance for an antiparallel configuration is $R_{AP} = \frac{r+R}{2}$, which is bigger than R_P. This gives the GMR ratio of

$$GMR = \frac{R_{AP} - R_P}{R_P} = \frac{(R-r)^2}{4rR} \qquad (1.2)$$

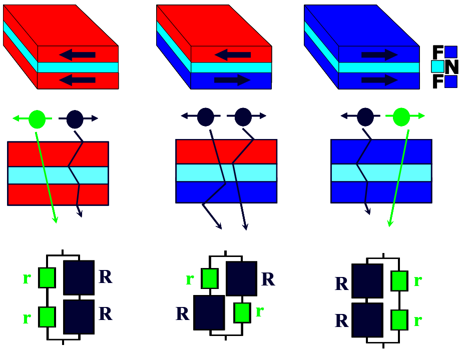

Figure 1.4 Schematic picture of the GMR mechanism. F is ferromagnetic layer and N is nonmagnetic spacer. For two F magnetizations parallel, electrons of one spin direction are scattered strongly in both layers, however electrons of the other spin are not in any layers. For antiparallel state, electrons of each spins are scattered strongly in alternate layers.

All the initial measurements of GMR were made with the current parallel to the plane of the thin film layers. That's called Current-In-Plane (CIP) geometry. GMR effects can also be obtained in the Current-Perpendicular-to-Plane (CPP) geometry. The first measurement of GMR in CPP geometry was done by Pratt et al. in sputtered Co/Cu multilayers [25]. In the CIP geometry, the current flows parallel to the layers. But from the simple picture above, the GMR effect requires a spin-related connection perpendicular to the layers. So if the mean free path of electrons in the N-layer spacer is much shorter than the N layer thickness, the electrons cannot communicate across the N layer, and thus can't sense the relative orientation of F-layer magnetizations. In CPP geometry, all the electrons pass perpendicularly through every F layer and the total resistance is simply the sum of the contributions from each layer. Hence the parallel and antiparallel states can be clearly distinct. As a result, CPP geometry provides a clear physical picture of the GMR phenomenon and higher GMR ratios required by industrial applications [26].

The detailed theory for CPP GMR was originally built by Fert [27]. Starting from the Boltzmann equation, he calculated both volume and interfacial spin-dependent scattering contributions to resistance. Assuming that the spin-diffusion length is much longer than the mean free path, the concept of spin relaxation was introduced in this theory to balance the spin accumulation effect at F/N interfaces. It's convenient to use the electrostatic chemical potential, μ, which is equivalent to the negative of the potential energy, $q\varphi$, of a test charge q in electrostatic field $E = -\nabla\varphi$. For an electron, $q = -e$, $\mu = e\varphi$. From the two current model, the electrostatic chemical potentials for spin-up and spin-down electrons are $\mu_\uparrow$ and $\mu_\downarrow$. The spin averaged chemical potential is defined as $\mu_0 = (\mu_\uparrow + \mu_\downarrow)/2$. The total conductivity is simply $\sigma = \sigma_\uparrow + \sigma_\downarrow$ and current density is $j = j_\uparrow + j_\downarrow$. In a nonmagnetic material, the two current channels have the same conductivity and carry same current density. However in a ferromagnetic material, the two spin states have different behaviors and we should include the asymmetry for both conductivity and current density as

$$\sigma_\uparrow = \alpha\sigma \quad \text{and} \quad \sigma_\downarrow = (1-\alpha)\sigma \qquad (1.3)$$

$$j_\uparrow = \beta j \quad \text{and} \quad j_\downarrow = (1-\beta) j \qquad (1.4)$$

where α and β are asymmetry parameters and both vary between 0 and 1. The conductivity asymmetry parameter, α, can change abruptly at the F/N interface. In the N layer, the two spin states are symmetric, so $\alpha_N = 0.5$, while in the F layer, the majority spin electrons have higher conductivity and $\alpha_F > 0.5$. The current density asymmetry parameter β has to be continuous at the F/N interface under the assumption of no interfacial spin-flip scattering. So, far away from the interface, $\beta_F = \alpha_F$ and $\beta_N = 0.5$. Close to the interface, β is not equal 0.5 in both F and N. The chemical potential is related to conductivity and current density as:

$$\partial\mu_{\uparrow,\downarrow} / \partial x = -(e/\sigma_{\uparrow,\downarrow}) j_{\uparrow,\downarrow} \qquad (1.5)$$

$$\partial\mu_0 / \partial x = -(e/\sigma) j \qquad (1.6)$$

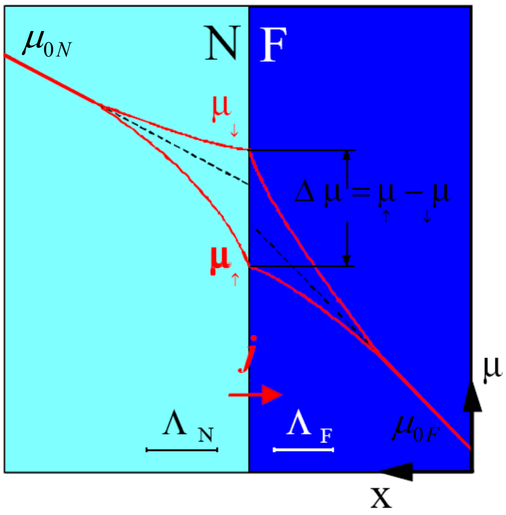

Figure 1.5 The electrostatic chemical potential $\mu_\uparrow$ (majority spins) and $\mu_\downarrow$ (minority spins) at the interface between ferromagnetic layer (F) and nonmagnetic layer (N) with a current flow in x direction. Dashed line is the spin averaged potential, it has a jump at the interface.

As shown in Figure 1.5, with the boundary condition that α is discontinuous at the interface (x=0), the spin averaged chemical potential μ_0 has a jump which is called the spin accumulation voltage: $V_{sc} = \mu_{0N} - \mu_{0F}(x=0)$. Therefore the interface resistance can be calculated as:

$$R_B = V_{sc} / j(x=0) \qquad (1.7)$$

The other boundary condition – the chemical potentials $\mu_\uparrow$ and $\mu_\downarrow$ are continuous at the F/N interface. This condition together with equation (1.5) results in a difference between the two chemical potentials $\Delta\mu = \mu_\uparrow - \mu_\downarrow$. This potential difference actually reflects the number of electrons out of equilibrium in the two current channels. It decays from the interface and obeys a diffusion equation [28]:

$$(\mu_\uparrow - \mu_\downarrow)/\tau_{sf} = D\partial^2(\mu_\uparrow - \mu_\downarrow)/\partial x^2 \qquad (1.8)$$

where τ_{sf} is the spin flip rate, $D = 1/3 v_F l$ (v_F is the Fermi velocity and l is the electron mean free path) is the diffusion constant. From the solution of (1.8), the potential difference decays exponentially on the scale of the spin flip diffusion length $\Lambda = \sqrt{D\tau_{sf}}$.

Now, consider the simple structure with two Fs separated by an N spacer, in the antiparallel state, the structure resistance includes the bulk resistances from each layer and the interface resistance. However, in the parallel state, the interface resistance is about zero as the spin accumulation on two F/N interfaces are opposite [27]. Finally the calculated GMR is [2]:

$$GMR = \frac{R_{AP} - R_P}{R_P} = \frac{(2\alpha_F - 1)^2}{4\alpha_F(1-\alpha_F)} \frac{\Lambda_F}{t_F} \qquad (1.9)$$

where t_F is the thickness of the F layer.

1.3 Point Contact

A point contact is a very small electrical contact between two metallic electrodes. It is widely used for investigations of electron kinetic properties such as electron-phonon, electron-magnon interactions in metals. Point contact was originally introduced by Sharvin, who used it to inject and detect ballistic carriers in electron focusing experiments. Spectroscopic properties of point contacts were extensively studied by Yanson [29]. He found that the current-voltage characteristics of metallic micro-contacts showed a non-linear behavior at liquid helium temperature and related the second-derivative signal d^2V/dI^2 to the electron-phonon scattering in metals. Very high current densities associated with point contacts were later used by Tsoi et al. to demonstrate spin-transfer-torque interactions in magnetic multilayered systems.

Already in 1904, Maxwell [30] studied the constriction resistance for a small metallic contact. He solved the classical Poisson's equation for the electrostatic potential energy, φ, and got the current I by an integral of the current density, J, over the contact area. The resulting resistance for the point contact is:

$$R_M = \rho / 2a \qquad (1.10)$$

where ρ is metal resistivity and a is point contact radius. Maxwell's calculation is in the regime where the mean free path, l, is much smaller than the contact radius a. In this regime ($l \ll a$), electrons move diffusively through the point-contact constriction and in Maxwell's calculation it is assumed that Ohm's law $(J = \sigma E = (1/\rho e)(\partial\varphi/\partial z))$ is valid (Figure 1.6a). However, with the point-contact size getting extremely small, the mean free path of the electron can be much larger than the contact radius a. In this case the motion of conduction electrons through the point-contact constriction is no longer diffusive and Ohm's law is no longer valid. This problem is analogous to the well known problem in the kinetic gas theory first realized by Knudsen [31]. Hence, the Knudsen ratio $K=l/a$

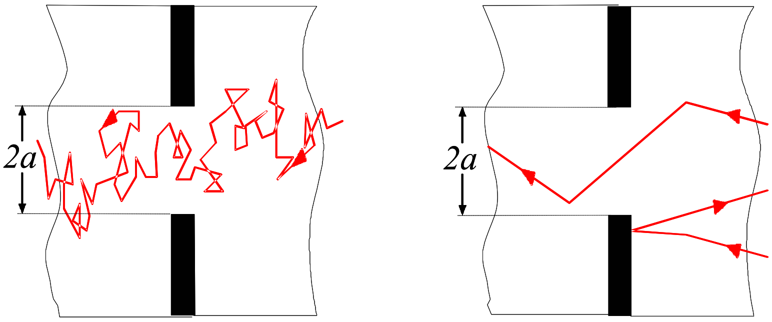

(a) (b)

Figure 1.6 Schematic view of electrons transport through a point contact. l is mean free path, a is point contact radius. a) Diffusive regime ($l<<a$). b) Ballistic regime ($l>>a$).

was used to characterize the different regimes for point contact electron transport. In this regime ($l>>a$), the electrons will be accelerated by an applied voltage, V, for the distance of the mean free path. Thus, an electron can ballistically cross the contact and gain the energy of eV (Figure 1.6b).

Sharvin first discussed this highly non-equilibrium electron transport through contacts (ballistic regime) and calculated the contact resistance with large Knudsen numbers [32]. In Sharvin's calculation, the electron velocity increment crossing the contact is $\Delta v = eV / p_F$, where p_F is the Fermi momentum. Then, the electrical current through the contact is given by $I \cong \pi a^2 n_0 e \Delta v = \pi a^2 (n_0 e^2 / p_F) V$, where n_0 is the electron density. Therefore, the Sharvin resistance for $K=l/a>>1$ of a circular contact is:

$$R_S = 4\rho l / 3\pi a^2 \qquad (1.11)$$

where the resistivity is: $\rho = p_F / n_0 e^2 l$. Sharvin resistance is actually independent of the electron mean free path as expected for electron ballistic transport [33]. For a complete theory of ballistic point contacts one should refer to Ref. [33, 34] where the full non-linear Boltzmann equation formalism was used.

This peculiar transport of current through such a contact in the ballistic regime makes point contacts very efficient tools for studying electron-magnon interactions as well as electron-phonon interactions.

As shown in Figure 1.7a, when applying a voltage, V, on the two electrodes, if there is no point contact, the electrostatic potential energy, $\varphi(z)$, has a linear distribution, which means that when an electron flows for a short distance without collision, it can get only a portion of the total energy eV. However, if there is a point contact connecting the two electrodes, the electrostatic potential energy has almost the entire voltage drop in the region near the contact (Figure 1.7b). Therefore when an electron moves across the contact, it can get and emit energy as high as the total energy eV.

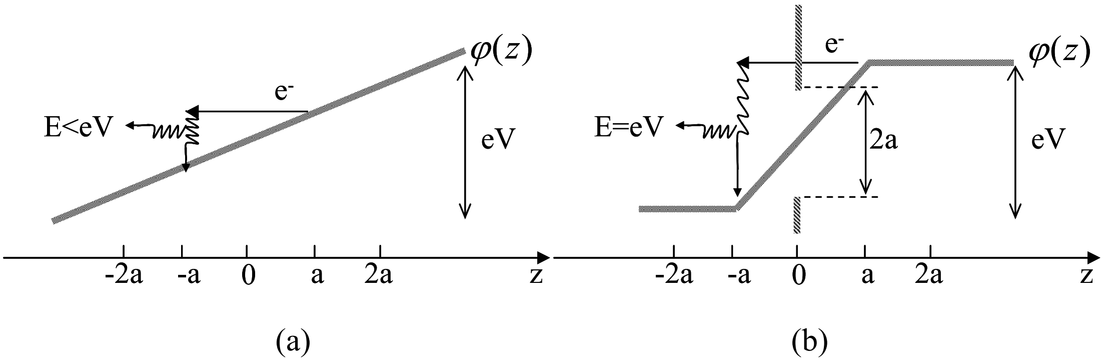

Figure 1.7 Electrostatic potential energy along the z axis. Voltage *V* is applied on two electrodes. a) No contact between two electrodes. Electrostatic potential energy has linear distribution. b) Point contact with diameter *2a* connects the two electrodes. Electrostatic has almost all the drop in the region near contact.

When the mean free path is in between the limits of the Maxwell resistance, R_M ($K<<1$), and the Sharvin resistance, R_S ($K>>1$), a simple formula can be found by interpolating equations (1.10) and (1.11). Wexler [35] has used the variational principle to solve the Boltzmann equation for contact resistance R:

$$R = \frac{4}{3\pi}\frac{\rho l}{a^2} + \Gamma(K)\frac{\rho}{2a} = \frac{4}{3\pi}\frac{\rho l}{a^2}\left(1 + \frac{3\pi}{8}\Gamma(K)\frac{a}{l}\right) \qquad (1.12)$$

where $\Gamma(K)$ is a slowly varying function of the Knudsen number *K*, with $\Gamma(K=0)=1$ and $\Gamma(K=\infty)=0.694$. Equation (1.12) is simplified but very useful for estimating the point contact size from the contact resistance, which is a lot easier to measure in an experiment. For an exact solution of point contact resistance, refer to Ref. [36].

The point contact is an ideal tool to study electron related energetic excitations, such as spin-wave excitations. It's the major tool in our experimental studies of spin-transfer-torque phenomenon. We use some unique techniques to make point contacts to magnetic multilayer samples and are able to achieve very high current densities, which is a key condition for current induced micro-magnetic dynamics as we will discuss in subsequent chapters.

1.4 Spin Transfer

Spin-angular momentum transfer is an interaction between spin polarized current and magnetic moments in a conducting medium. This phenomenon originates from the exchange of angular momentum between magnetic moments and electron spins – a concept which has been researched from since early 1970s and 1980s, with the work of Berger on current-induced domain wall motion [37, 38]. In 1996, Slonczewski and Berger independently predicted that at high enough current densities, the spin-polarized current could generate significant torque on magnetic moments in multilayered systems and induce magnetic excitations or even reversal of magnetization of a whole layer [39, 40]. With the theoretical guidance, the experimental verification moved forward rapidly [41-43] and now it's reasonable to consider the applications of this spin-transfer-torque effect [44].

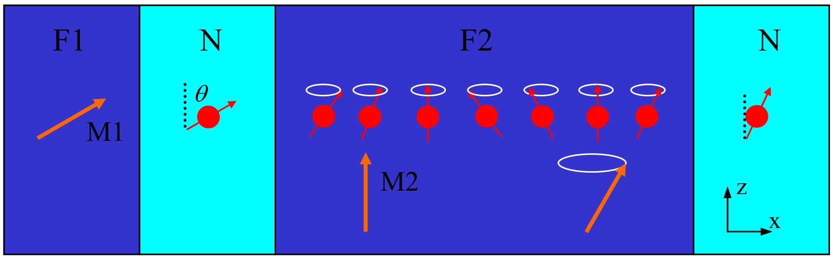

Figure 1.8 Semiclassical picture of a spin polarized electron interacting with magnetic moment in ferromagnetic thin film. The spin-polarized electrons precess when they cross the ferromagnet and undergo angular momentum change. The angular momentum must be compensated from ferromagnetic moments for conservation.

The sketch for the basic idea of the spin-transfer effect is shown in Figure 1.8. We consider a simple structure with two ferromagnetic layers (F1, F2) and two nonmagnetic layers (N) alternatively. The electrons (red) travel from F1 to F2 along the x direction. The orange arrow indicates the ferromagnetic moments. The electron spins are first polarized along F1 at an angle, θ, with the z direction. Then, at the interface between N and F2, some of the electrons will be transmitted. The transmission amplitudes of majority and minority electrons are different: usually, spin-up (majority) electrons have larger transmission amplitude. This difference causes the transmitted electrons to have spin at a smaller angle than incident angle θ. As the electrons travel through the F2, they will have a strong exchange interaction with the magnetic moments in the layers. Assuming the F2 magnetization is in the z direction, than the electron spins are non-collinear with magnetic moments and the electron spins will precess about the z direction. To conserve the total angular momentum, the ferromagnetic moments will also precess. This precession is very fast. For example in Co, electrons can travel only a few lattice spaces in one precession period. For a single electron, when it crosses the F2 after several precession periods, the x, y components of the final spin state can be either positive or negative because electrons travelling at different angles with the x axis will acquire different phase angles. Averaging over all electronic states results in zero net spin-angular momentum in the x and y directions and electron spins are polarized along F2. Now let's compare the initial (incident) spin state of electrons with their final (transmitted) spin state. The incident electrons have spins tilted at angle θ relative to the z direction. They have spin angular momentum with z and x components. The transmitted electrons have spin angular momentum only in the z direction. So the electrons lose the angular momentum component transverse to the original orientation of F2 moment. To conserve momentum, this component must be absorbed by the magnetic film. Suppose the ferromagnet responds as a single domain, then the ferromagnetic moments should rotate. The expected torque should be in the direction that rotates the ferromagnetic moments toward the incident electron spin direction and the torque magnitude is proportional to $\sin\theta$.

Although this semi-classical picture is somewhat oversimplified, it's still useful to understand the origin of spin-transfer-torque in ferromagnetic thin-film structures. A full calculation should include the multiple reflections from F/N interfaces and the angular momentum of reflected electron states. In order to understand the dynamics of ferromagnetic layer moments with the effect from spin transfer, it's necessary to discuss the well known Landau-Lifshitz-Gilbert (LLG) equation. The torques from applied magnetic fields, magnetic anisotropies, and damping, together with spin transfer torque are combined in this equation [39, 45-47]. We consider a simple and symmetric system with the layer structure similar to the one in Figure 1.8. We have F1 as the fixed layer. Electrons are polarized in F1, then come into F2 and transfer spin torque to the F2 magnetization. The F2 layer is considered a free layer and the dynamics of the F2 magnetization under torques is described by the LLG equation [47]:

$$\frac{d\vec{M}}{dt} = -\gamma\vec{M}\times\vec{H}_{eff} + \frac{\alpha}{M_s}\vec{M}\times\frac{d\vec{M}}{dt} + \frac{\gamma a_J}{M_s}\vec{M}\times(\vec{M}\times\hat{M}_p) \qquad (1.13)$$

where $\vec{M}$ is the magnetization of free layer, γ is the gyromagnetic factor, α is Gilbert damping parameter and $\hat{M}_p$ is a unit vector with the direction of the fixed layer's magnetization. The effective field is $\vec{H}_{eff} = \vec{H}_{app} + \vec{H}_{ex} + \vec{H}_a - 4\pi\vec{M}_s$, where $\vec{H}_{app}$ is the externally applied field, $\vec{H}_{ex}$ is the interlayer exchange field, $\vec{H}_a$ is the anisotropy field and $4\pi\vec{M}_s$ is the demagnetization field. The factor a_J depends on the current, spin polarization, *P*, and the angle, θ, between the free and fixed layer magnetizations: $a_J = \frac{\hbar I}{e} g(P,\theta)$ [39], where *g* is a function of *P* and increases with θ [48, 49]. The torques acting on the free layer magnetization are shown in Figure 1.9. The first term on the right side of LLG equation, causes the free layer magnetization ***M*** to precess about the effective field in the case of an initial deviation from the effective field. The second term indicates the damping torque, which accounts for the energy loss of the free layer. With the damping torque, the free layer magnetization will spiral back to the effective field direction to minimize the energy. The third term in the LLG equation

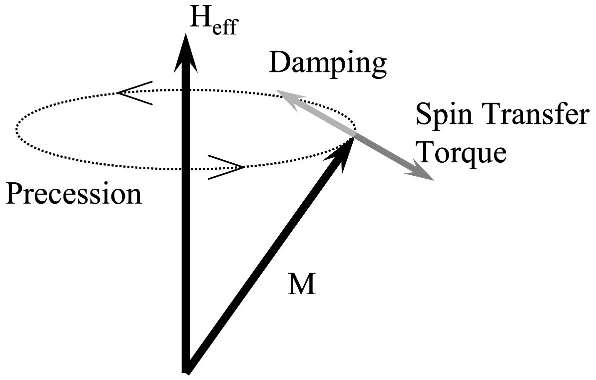

Figure 1.9 Schematic of magnetization dynamics with a spin transfer torque. The torque due to effective field causes precession. The damping torque causes the magnetization spiral back to effective field direction. The current induced spin transfer torque is collinear with the damping. When they are opposite, spin transfer torque can destabilize the magnetization.

is the current-induced spin-transfer-torque term. Usually the fixed layer is aligned with the effective field, so that the spin-transfer torque is collinear with the damping. For one current direction, this spin transfer torque is in the same direction with the damping torque. It enhances the damping and brings the magnetization back towards the effective field direction faster than in the case without current. For another current direction, the spin-transfer torque is opposite to damping. This is the case where all kinds of spin-transfer phenomena happen. If we say the damping torque stabilizes the free layer magnetization, then the spin transfer torque actually destabilizes it. There are basically three forms of dynamics for the magnetization depending on the balance between effective field, damping and spin-transfer torques. For the current lower than some threshold (critical) current, the current-induced spin-transfer torque can't cancel the damping, and the free layer magnetization will spiral back to the applied field direction (although slower than without current), which is called damped motion (Figure 1.10 (b)). For current higher than the critical current, there are two possible motions depending on the magnitude of the applied field and the angular dependence of both damping and current-induced torques. It's possible for the free layer magnetization to have a stable precession, where the energy being lost to damping is compensated by the energy from current (Figure 1.10 (c)). In this motion, the precession frequency can be tens of GHz, which increases with applied field. The

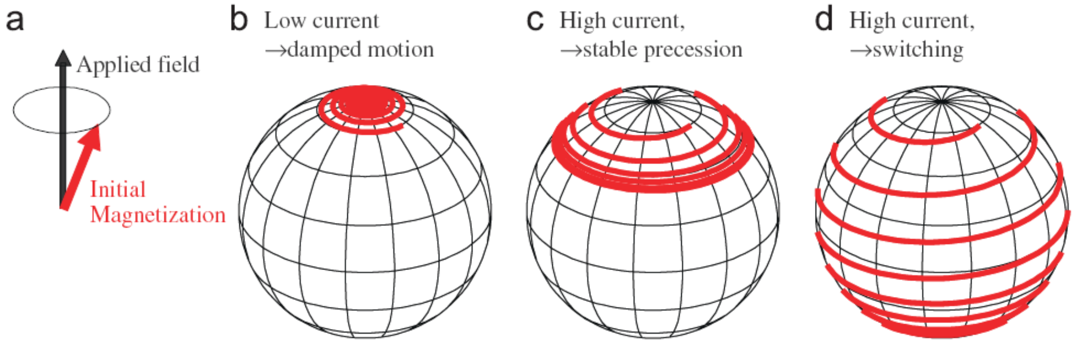

Figure 1.10 Trajectories of spin torque driven dynamics for the free layer magnetization. a) The initial magnetization precesses about the applied field due to the field torque. b) For current below critical current, magnetization spirals back toward the low energy applied field direction on account of damping torque. c) For current larger than critical current, it possible for magnetization to be in a stable precession where the spin transfer torque is balanced with damping. d) At low applied field, the high current can increase the precession angle all the way to π, where the free layer magnetization is switched to be antiparallel with fixed layer [50].

other possible motion is for lower applied fields, where the energy from spin transfer is relatively big and the spin torque can increase the precession angle all the way to $\theta = \pi$ (Figure 1.10 (d)). This is called switching motion, which means that the free layer magnetization is reversed by current to be antiparallel to the fixed layer.

For experimental observation of the spin-transfer-torque effect the density of electric current should be high enough to produce sizable torque on the magnetization of the free layer. Thus one of the most important experimental conditions is that the current flow should be constricted to a very small cross-sectional area. In principle, there are at least two known mechanisms of interactions between the magnetic moment and current: current induced Oersted fields and current induced spin-transfer-torque. The critical currents at which the magnetic moment can be affected for these mechanisms, however, depend differently on the radius r of a circular orifice through which current flows. For a current induced Oersted field, the critical current is proportional to r, while the spin-transfer-torque produces critical current which is proportional to r^2 [51]. So only at small dimensions, is the threshold from the spin-transfer-torque is lower and the spin-transfer effect is dominant. There are several device geometries to produce small enough current constrictions in experiments. Figure 1.11 shows three main types of such devices.

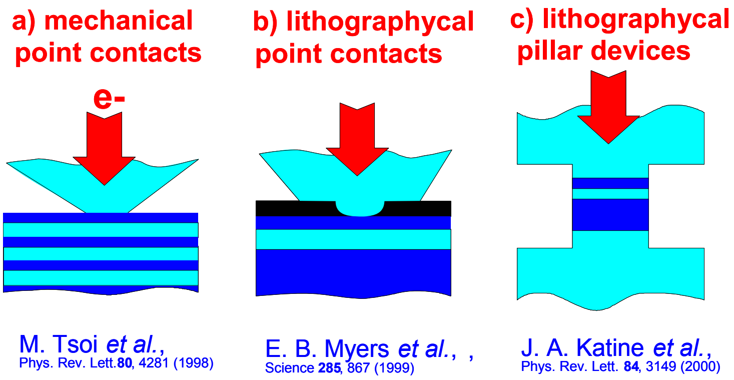

Figure 1.11 Device geometries used in experiments for studying spin transfer effect.

In 1998, Tsoi et al. observed the current-induced spin-wave excitations in magnetic multilayers at high perpendicular field [41]. This was the first experiment, after original predictions by Slonczewski [39] and Berger [40], which demonstrated that an electrical current can affect magnetic state of a ferromagnet. In this experiment, a mechanical point contact was used to inject high current density perpendicular to the multilayer stuck [Figure 1.11 (a)]. Here a sharpened metal tip is carefully brought to the multilayer sample surface to make an extremely small (point) electrical contact with the multilayer. The current density can be greater than 10^8A/cm^2, which is high enough to excite spin waves. Myers et al. [42] used another type of point contact to study the magnetic excitations in a Co/Cu/Co sandwich structure [Figure 1.11 (b)]. They used electron-beam lithography and reactive ion etching to produce a bowl-shaped hole in an insulating layer, which covers the sample, and then fill the hole by evaporated Cu to form the point contact. In both point contact geometries, the excited magnetic moments are within a nanoscale region of the contact's constriction. This region is smaller than 100 nm, so the magnetic moments in this region might be expected to move as a single domain. However the region is still connected to the continuous magnetic film and is coupled with moments around it, which means it usually requires rather large current densities to affect it. Fortunately, point contacts can reach very small sizes of about a few nanometers, and provide high enough current densities. The other very popular device geometry which has a lower critical current density is a so-called magnetic nanopillar. Many experiments showed spin-transfer effects, both free layer switching and spin-wave excitations, in nanopillars with lateral dimensions from ~50 nm to about 200 nm [43, 52-54]. In a nanopillar, the magnetic layers are patterned to a small cross-section so that there is no coupling to a large film around it as in the previous example [Figure 1.11 (c)]. Though the magnetic dynamics in the nanopillar is damped by additional roughness from the walls of the pillar, one might expect a lower less current density for spin-transfer effect to occur, which compensates the relatively big dimension due to technical limitations. The detailed processes for patterning the nanopillar, including evaporation, ion milling, and lithography, are described in detail in Refs. [55, 56].

The spin transfer effect has many exciting applications. The spin-transfer oscillator, where the magnetic moments exhibit a steady precession, has a wide frequency range (up to hundreds of GHz), small size, and fast modulation capability [57]. It can find many applications in wireless communications systems such as a reference oscillator for data transfer. Current induced magnetization switching in Magnetic Tunnel Junction (MTJ) can be used in Magnetoresistive Random Access

Memory (MRAM) [44]. Here MTJ is a device where the two ferromagnetic layers are separated by a dielectric layer such as MgO. In MRAM, the writing current directly flows through the memory bit made of a MTJ and switches the free layer. The information can be read out by reading current across the same MTJ in place of the GMR effect. This spin-transfer-torque (STT) MRAM is a kind of non-volatile memory. Its excellent scalability, ultra fast operation speed and fabrication compatibility make it a promising universal memory in the near future. Spin-transfer-torque is also important for read heads in magnetic storage devices. With the scaling of read heads, the bias current density is getting high enough to induce the spin-transfer effect into reader layers, which may actually increase the reader's noise and destabilize the coupled layers [58].

1.5 References

[1] A.P. Guimaraes, “Magnetism and Magnetic Resonance in Solids” (John Wiley & Sons, Inc. P 92 1998)

[2] J. Stöhr, H. C. Siegmann, *“Magnetism: from fundamentals to nanoscale dynamics”* (Springer Series in Solid-State Sciences, Springer, 2006).

[3] N. F. Mott, Proc. R. Soc. A **117**, 610 (1928)

[4] J. C. Slater, Phys. Rev. 49, 537 (1936)

[5] J. C. Slater, Phys. Rev. 49, 931 (1936)

[6] E. C. Stoner, Proc. Roy. Soc. (London) A **154**, 656 (1936)

[7] E. C. Stoner, Proc. Roy. Soc. (London) A **165**, 372 (1938)

[8] J. Mathon, A. Umerski, in *Physics of Low Dimensional Systems*, ed. by J. Moran-Lopez (Kluwer/Plenum, New York, 2001), p. 363.

[9] M. N. Baibich, J. M. Broto, A. Fert, F. N. V. Dau, F. Petroff, P. Eitenne, G. Creuzet, A. Friederich, J. Chazelas, *Phys. Rev. Lett.* **61**, 2472 (1988)

[10] G. Binasch, P. Grunberg, F. Saurenbach, W. Zinn, *Phys. Rev. B* **39**, 4828 (1989)

[11] J. S. Moodera, L. R. Kinder, T. M. Wong, R. Meservey, *Phys. Rev. Lett.* **74**, 3273 (1995)

[12] Y. Tokura, Y. Tomioka, *J. Magn. Magn. Mater.* **200**, 1 (1999)

[13] N. Garcia, M. Munoz, Y. W. Zhao, *Phys. Rev. Lett.* **82**, 2923 (1999)

[14] R. Schad, C. D. Potter, P. Belien, G. Verbanck, V. V. Moshchalkov, and Y. Bruynseraede, *Appl. Phys. Lett.* **64**, 3500 (1994)

[15]S. S. P. Parkin, N. More, and K. P. Roche, *Rhys. Rev. Lett.* **64**, 2304 (1990)

[16] S. S. P. Parkin, R. Bhadra, and K. P. Roche, *Rhys. Rev. Lett.* **66**, 2152 (1991)

[17] D. H. Mosca, F. Petroff, A. Fert, P. A. Schroeder, W. P. Pratt, and R. Loloee, *J. Magn. Magn. Mater.* **94**, L1 (1991)

[18] J. Barnas, A. Fuss, R. E. Camley, P. Grunberg, and W. Zinn, *Phys. Rev. B* **42**, 8110 (1990)

[19] T. Shinjo, H. Yamamoto, *J. Phys. Soc. Japan* **59**, 3061 (1990)

[20] L. Piraux, J. M. George, J. F. Despres, C. Leroy, E. Ferain, R. Legras, K. Ounadjela, and A. Fert, *Appl. Phys. Lett.* **65**, 2484 (1994)

[21] B. Dieny, V. S. Speriosu, S. S. P. Parkin, B. A. Gurney, D. R. Wilhoit, and D. Mauri, *Phys. Rev. B* **43**, 1297 (1991)

[22] N. F. Mott, *Proc. Phys. Soc.* (London), Ser. A **153**, 699, and **156**, 368 (1936)

[23] A. Fert, and I. A. Campbell, *Phys. Rev. Lett.* **21**, 1190 (1968)

[24] A. Fert, and I. A. Campbell, *J. Phys.* **F6**, 849 (1976)

[25] W. P. Pratt, S. F. Lee, J. M. Slaughter, R. Loloee, P. A. Schroeder, and J. Bass, *Phys. Rev. Lett.* **66**, 3060 (1991)

[26] P. A. Schroeder, J. Bass, P. Holody, S. F. Lee, R. Loloee, W. P. Pratt Jr., and Q. Yang, *Mater. Res. Soc. Symp. Proc.* **313**, 47 (1993)

[27] T. Valet, A. Fert, *Phys. Rev. B* **48**, 10 (1993)

[28] P.C. van Son, H. van Kempen, and P. Wyder, *Phys. Rev. Lett.* **58**, 2271 (1987)

[29] I. K. Yanson, *Zh. Eksp. Teor. Fiz.* **66,** 1035 (1974) (*Sov. Phys. –JETP* **38** 506

1974)

[30] J. C. Maxwell, *A. Treatise on Electricity and Magnetism* (1904) (Oxford: Clarendon)

[31] M. Knudsen, *Kinetic Theory of Gases*, (1934), (London: Methuen)

[32] Yu. V. Sharvin, *Zh. Eksp. Teor. Fiz.* **48**, 984 (1965) (*Sov. Phys. –JETP* **21**, 655)

[33] A. G. M. Jansen, A. P. van Gelder and P. Wyder, *J. Phys. C: Solid State Phys.* **13**, 6073 (1980)

[34] I. O. Kulik, A. N. Omel'yanchuk and R. I. Shekhter, *Fiz. Nizk. Temp.* **3**, 1543 (1977) (Engl. Transl. *Sov. J. Low Temp. Phys.* **3**, 740)

[35] G. Wexler *Proc. Phys. Soc.* **89**, 927 (1966)

[36] B. Nikolic, P. B. Allen, *Phys. Rev. B* **60** 3963 (1999)

[37] L. Berger, *J. Appl. Phys.* **55**, 1954 (1984)

[38] C. –Y. Hung, and L. Berger, *J. Appl. Phys.* **63**, 4276 (1988)

[39] J. C. Slonczewski, *J. Magn. Magn. Mater.* **159**, L1 (1996)

[40] L. Berger, *Phys. Rev. B* **54**, 9353 (1996)

[41] M. Tsoi, A. G. M. Jansen, J. Bass, W. –C. Chiang, M. Seck, V. Tsoi, and P. Wyder, *Phys. Rev. Lett.* **80**, 4281 (1998)

[42] E. B. Myers, D. C. Ralph, J. A. Katine, R. N. Louie, and R. A. Buhrman, *Science* **285**, 867 (1999)

[43] J. A. Katine, F. J. Albert, R. A. Buhrman, E. B. Myers, and D. C. Ralph, *Phys. Rev. Lett.* **84**, 3149 (2000)

[44] Z. Diao, Z. Li, S. Wang, Y. Ding, A. Panchula, E. Chen, L. C. Wang, and Y. Huai, *J. Phys:Condens. Matter.* **19,** 165209 (2007)

[45] J. Z. Sun, *Phys. Rev. B* **62**, 570 (2000)

[46] Y. B. Bazaliy, B. A. Jones, and S. –C. Zhang, *J. Appl. Phys.* **89**, 6793 (2001)

[47] Z. Li, and S. Zhang, *Phys. Rev. B* **68**, 024404 (2003)

[48] M. D. Stiles, and A. Zangwill, *J. Appl. Phys.* **91**, 6812 (2002)

[49] A. Shpiro, P. M. Levy, and S. Zhang, *Phys. Rev. B* **67**, 104430 (2003)

[50] D. C. Ralph, and M. D. Stiles, *J. Magn. Magn. Mater.* **320**, 1190 (2008)

[51] J. Z. Sun, *Handbook of Magnetism and Advanced Magnetic Materials*, **5**, 2595 (2007)

[52] J. Grollier, V. Cros, A. Hamzic, J. M George, H. Jaffres, A. Fert, G. Faini, J. B. Youssef, and H. Legall, *Appl. Phys. Lett.* **78**, 3663 (2001)

[53] M. Tsoi, J. Z. Sun, and S. S. P. Parkin, *Phys. Rev. Lett.* **93**, 036602 (2004)

[54] S. Urazhdin, N. O. Birge, W. P. Pratt, Jr., and J. Bass, *Phys. Rev. Lett.* **91**, 146803 (2003)

[55] J. Z. Sun, D. J. Monsma, D. W. Abraham, M. J. Rooks, and R. H. Koch, *Appl. Phys. Lett.* **81**, 2202 (2002)

[56] F. J. Albert, J. A. Katine, R. A. Buhrman, and D. C. Ralph, *Appl. Phys. Lett.* **77**, 3809 (2000)

[57] M. R. Pufall, W. H. Rippard, and S. Kaka, *Appl. Phys. Lett.* **86**, 082506 (2005)

[58] K. B. Klaasen, J. Peppen, X. Xing, *IEEE Trans. Magn.* **42**, 108 (2006)

Chapter 2
Experimental Setup

This chapter describes the experimental setup and method for exploring spin-transfer phenomena in magnetic thin-film multilayers. These include thin-film deposition with sputtering, sample patterning with focused ion beam milling, point contact fabrication, and the electrical measurement system.

2.1 Multilayer and Spin Valve Deposition

Since the late 1950's, thin films have been extensively studied because of their extensive applications in electronic devices. Nowadays, multilayered thin film-devices are widely used in consumer electronics. In these devices, the layers can be dielectrics, semiconductors, and/or metals. For our spin-transfer related research, most of thin film layers are magnetic and nonmagnetic metals. There are two main methods for thin film deposition: Chemical Vapor Deposition (CVD) and Physical Vapor Deposition (PVD). In CVD, the film is produced by a chemical reaction between the reactant gases and the substrate surface. CVD deposition has better filling and topography coverage. However, CVD is not very good for metal deposition because of contamination from reaction gases. CVD deposition of metal alloys is also difficult. In contrast, PVD deposition techniques are generally more versatile. PVD allows deposition of almost any material. Here, physical methods are used to produce an atomic flux. The target atoms travel a certain distance towards a substrate and there condense to form a thin film. PVD process usually has no reaction and fewer gas-phase collisions between source atoms and the substrate, therefore the source atoms can stick on the substrate without desorbing and redeposition. There are mainly two ways to produce an atomic flux: evaporation and sputtering.

Evaporation is perhaps the simplest method of producing thin films. In the evaporation process, the atomic flux is typically produced by heating the source material until it vaporizes. The source material heater can be a resistance type tungsten filament or a high energy electron beam. The e-beam heater in general can achieve higher temperatures, which allow a wider range of materials to be deposited. In addition, the e-beam process is cleaner than a resistance heater where metal filaments might cause contamination. Evaporation deposition does little damage to the wafer due to low energy particles in the process and the deposited film is rather pure because of low deposition pressures ($<10^{-5}$ Torr). However, it is difficult to combine the evaporation technique with conventional silicon fabrication technology because: (i) when depositing alloys, it is critical to control alloy composition with a very high precision. Since evaporation rates are different for different materials, such a control is hard to achieve with evaporation techniques; (ii) Production of integrated circuits/devices require excellent step coverage, which is harder to achieve with evaporation techniques due to highly collimated fluxes of evaporated atoms in high vacuum [1].

Sputter deposition is now the most widely used PVD deposition technique. In our experiment, all the samples are deposited by sputtering. Here we will describe in detail the physics of sputtering process and the sputtering system we used in our experiments.

When energetic particles, such as accelerated ions, bombard the target surface, they collide with the solid surface atoms, transfer energy and kick these atoms out. This phenomenon is called *sputtering*. The sputtered target atoms produce an atomic flux which can condense on a substrate to form a thin film. There are several sputtering methods including DC diode, RF diode, and magnetron sputtering. The simplest method is the DC sputtering, which is used below to describe the sputtering process.

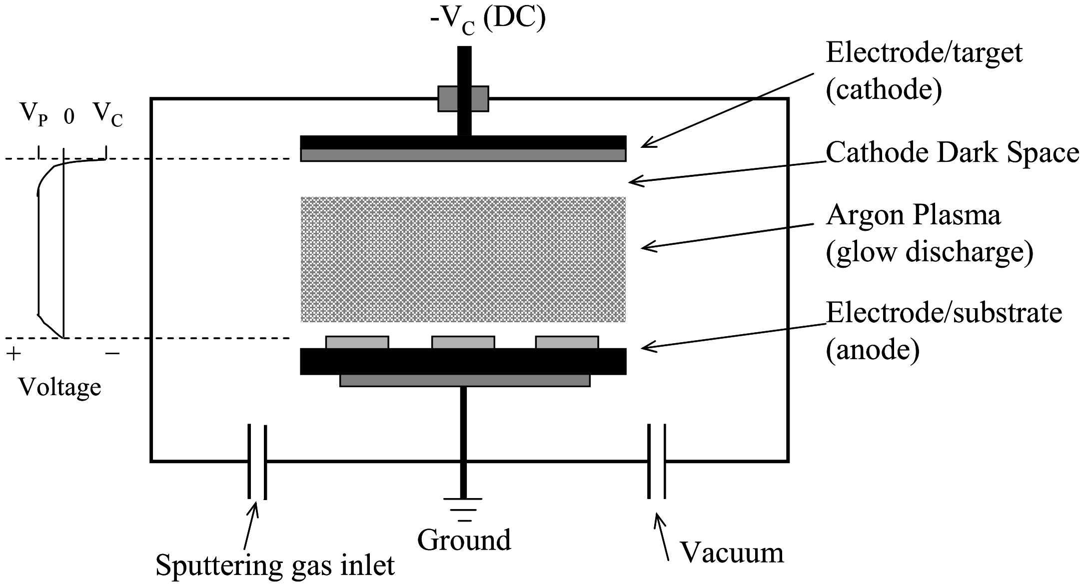

Figure 2.1 Schematic diagram of a DC sputtering system and voltage distribution.

As shown in Figure 2.1, a DC sputtering system is composed of a pair of planar electrodes. The substrate is on the anode, which is usually grounded. The target is on the cathode which is biased at negative 2~5 kV. The sputtering chamber is filled with an inert gas (argon). The working pressure is typically optimized at a few hundred mTorr depending on the bias voltage to provide a high enough deposition rate. At high DC bias voltage, plasma can be created between the two electrodes. The argon plasma contains the neutral argon atoms, positive argon irons, and free electrons. Since the cathode is negatively biased, the positive plasma ions are accelerated towards the cathode. These energetic ions strike the target material and sputter the target atoms. These target atoms then travel across the vacuum chamber to the substrate. There is a region near the cathode called the "dark space" where there is an excess of positive ions and a shortage of electrons. From the distribution of voltage in Figure 2.1, most of the voltage drop in the system occurs across this region. It's dark because there are few collisions between argon atoms and electrons which mean less photon are emitted from excited states. The plasma voltage is fairly constant in the glow discharge region but with a positive value, V_P. This is primarily due to both electrons and argon ions randomly striking the chamber surface and escaping the plasma. Here electrons with less mass and high mobility will strike more often and leave a positively charged plasma. The sputtering deposition process mainly contains two parts: sputtering of atoms from target and thin-film growth (condensation of atoms) on substrate.

Figure 2.2 shows the atom sputtering process near the target at a negative voltage. On the target, the accelerated argon ions strike surface atoms. At the moment of impact, the first thing that happens is an electron exchange when they are angstroms apart. This process occurs in a very short time (10^{-15}s) and results in an electronic excitation. When the distance between the ion and surface atom decreases further, the ion with atomic number Z_1 and surface atom Z_2 evolve into the unstable but united atomic orbital with quasi-atomic number Z_1+Z_2. As the distance shrinks even more, electronic repulsion and the Pauli exclusion principle begin to dominate. Then the collisions separate the atoms and re-ionize the neutrals. This ion impact establishes a train of collision events in the target, leading to the ejection of target atoms, which is sputtering. Since sputtering is the result of momentum and energy transfer, the incoming argon ions should have high enough energy to break the bonds holding the target atom in place. The typical surface binding energy is 5~10 eV. With high enough energy of argon ions, the collision cascade can be 5-10 nm below the target's surface. However, the particles ejected are usually within 1nm of the surface. Only a small fraction of collisions produce sputtering. To measure the efficiency of sputtering, the sputter yield, *S*, is defined as the number of sputtered atoms per incident particle. In a practical sputtering process, the yield is from 0.1 to 10 %. During the collision with the target surface, secondary electrons are emitted. They are accelerated away from the cathode. These electrons then travel back into the argon plasma and collide with the argon atoms, ionizing some of them and sustaining the plasma.

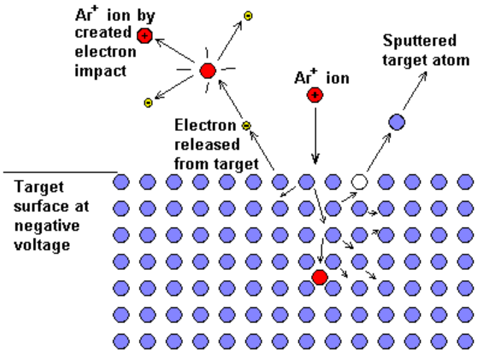

Figure 2.2 Sputtering process at the target/cathode [2].

The thin-film growth process is the other important process in sputtering deposition. When the sputtered target atoms arrive at the substrate, first they lose their perpendicular-to-substrate velocity component and are physically adsorbed on the substrate surface. The adsorbed atoms are not yet in equilibrium. They move over the substrate to form bigger clusters. The clusters adsorb more species and grow to a critical size at which they are thermodynamically stable. This is called nucleation stage. These critical clusters grow in numbers as well as in size. Usually the lateral growth rate is much higher than perpendicular-to-substrate growth rate. The grown clusters are called islands. The next stage is coalescence stage, in which the small islands want to coalesce with each other to reduce the substrate surface area. When the large islands grow together, they form a network structure, leaving channels and holes of uncovered substrate. Finally, filling of the channels and holes gives a continuous film [3]. The temperature of the substrate is important during sputtering deposition since, for the clusters or islands, diffusion and surface energy depend on the temperature. Usually, increasing the substrate temperature will increase the surface mobility and lower the deposition rate, but give high quality film.

A DC sputtering system is only good for conducting metal targets. For insulating materials, positive argon ions will build up on the cathode and can cause up to 10^{12} DC voltage needed for sputtering. An RF sputtering system is used to sputter insulators. Here an RF voltage with typical frequency 13.56MHz is applied between the two electrodes. With the oscillation of electrical field, both electrons and argon ions follow. Electrons have high mobility and can follow at high frequency while heavy argon ions can't. The electrons thus build up a negative bias on the target. The target maintains this self-biasing potential during the deposition and help to attract the heavy argon ions for sputtering. During the RF cycle, there will be also sputtering of the substrate. So the substrate and chamber are connected to make a very large electrode which makes sure that there is not much sputtering off the substrate. In the RF plasma, the electrons gain energy from oscillating RF fields and have more collisions with neutral argon atoms. This means the efficiency of ionization is increased. So for the same deposition rate, an RF sputtering system can operate at lower argon pressures (1-15 mTorr), while DC sputtering requires a few hundred mTorr.

In our lab, we use a magnetron sputtering system. Conventional DC and RF sputtering have rather low efficiency of ionization from the energetic collisions between the electrons and argon atoms. Indeed most electrons lose their energy in non-ionizing collisions or are collected by the electrodes [1]. In magnetron sputtering, a magnetic field is applied perpendicular to the electric field (Figure 2.3). This

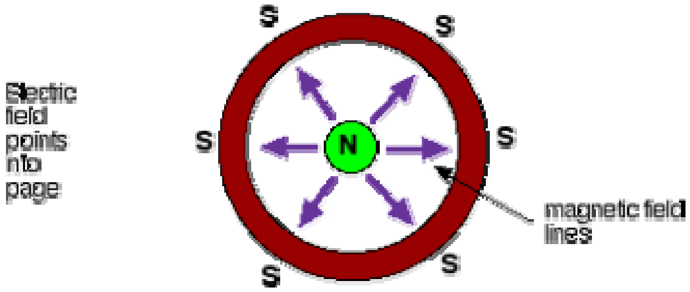

Figure 2.3 Magnetic fields on top of the target in a magnetron sputtering system [4].

magnetic field traps the electrons near the target and causes them to spiral around in the parallel plane right above the target. As a result, the electrons have a longer path length in the plasma, gain higher energy and have a higher probability to collide with argon atoms. Magnetron sputtering significantly increases the ionization efficiency which allows very low working pressures (down to 0.5 mTorr).

Figure 2.4 shows a top view of our magnetron sputtering system. Here, part (1) is the main chamber, which is basically a cylinder with height of 36 inches and diameter of 24 inches. Part (2) is two magnetron sputtering sources in RF modes. Part (3) is two other magnetron sputtering sources in DC modes. Part (4) is cryo-pump, which is used to pump the main chamber. Part (5) is two linear-rotary manipulators. One is to lower or lift the sample cradle for sample loading. The other is for a rotating mask plate. Part (6) is a load-lock through which the sample is initially loaded. It’s the pre-vacuum part which will open directly to the atmosphere. Part (7) is a magnetic transfer arm which is used to transfer the sample from the load-lock to the main chamber.

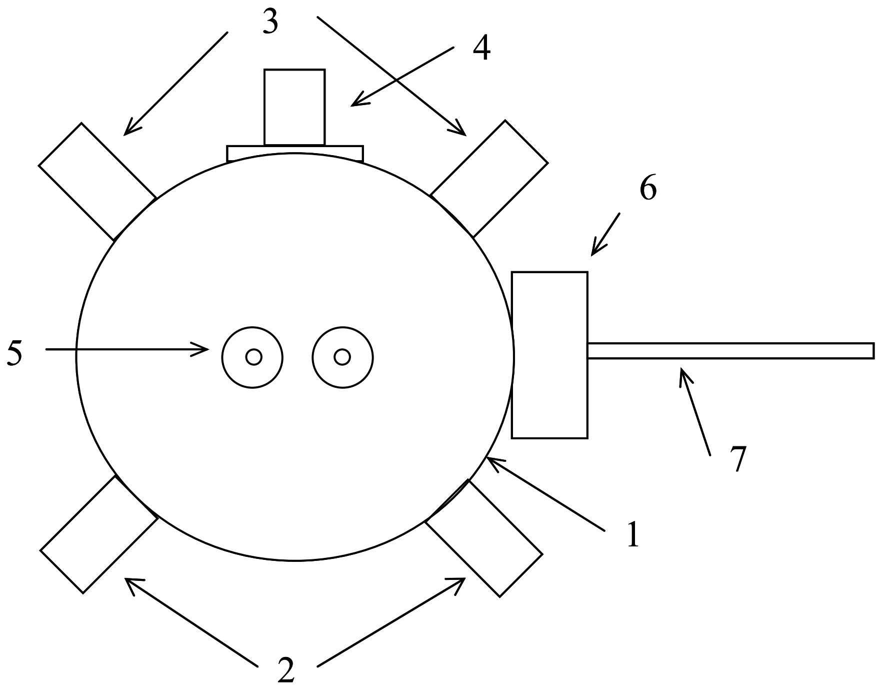

Figure 2.4 Top view of sputtering system in our lab for magnetic multilayer deposition.(1) Main chamber, (2) Sputtering source (RF), (3) Sputtering source (DC), (4) Cryo-pump,(5) Linear-rotary manipulators, (6) Sample load-lock, (7) Magnetic transfer arm.

The main process for vacuum preparation and thin film deposition is presented as follows:

1. Vacuum preparation

Start from atmosphere; open both the cryo-pump valve and the load-lock valve. Use a mechanical pump that is connected to the load-lock to pump the whole system down to about 6 mTorr. Then close the cryo-pump valve and turn on the cryo-pump to pre-vacuum the cryo-pump itself. After loading the sample to the cradle (see step 2), close the load-lock valve, open the cryo-pump valve. Then the cryo-pump can pump down the main chamber to a base pressure of about 10^{-5} mTorr.

2. *Sample Loading*

Vent the load-lock with N_2. Load the sample on a transfer fork in the load-lock. Then use a mechanical pump to pump down the load-lock to a few mTorr. Afterwards, open the load-lock valve and use a magnetic transfer arm to place the sample onto the cradle in the main chamber. Finally, close the load-lock valve to isolate the main chamber with the sample from outside.

3. *Film Deposition*

The actual deposition process is quite short, lasting only about 10 minutes. Operating with a computer program, turn on the source power first. After increasing the working pressure to about 5~6 mTorr and the power to 20W, the plasma should start up. Then, keep increasing the power to about 200W. Decrease the working pressure a little to 3~4 mTorr. Lower pressure usually gives higher deposition rate. The sputtering gas is pure argon (99.9998%). We usually set the argon gas flow rate at 40 sccm. With these parameters, the typical deposition rate is around 2 A/s depending on target materials.

In our prepared samples, the film thickness is only a few nanometers, so it’s very critical to control the thickness precisely. The key component for monitoring the film thickness is a Quartz Crystal Monitor (QCM). When a voltage is applied to this piezoelectric quartz crystal, the crystal is distorted and changes shape in proportion to the voltage. At a certain applied frequency, electro-mechanical resonance is encountered [5]. When extra mass is added onto the quartz crystal the resonance frequency decreases. This frequency shift can be directly related to the mass change. In 1972, Lu and Lewis developed an equation for this process by treating the resonance crystal and deposited film as a one dimensional continuous acoustic resonator [6].

$$T_f = \left(\frac{N_{at} d_q}{\pi d_f F_c Z} \right) \arctan\left(Z \tan\left(\frac{\pi (F_q - F_c)}{F_q} \right) \right) \tag{2.1}$$

where T_f is the film thickness, F_q is the resonance frequency for the bare quartz crystal, F_c is the resonance frequency of the crystal with film. $Z = (d_q u_q / d_f u_f)^{1/2}$ is the acoustic impedance ratio, d_q and d_f are the densities of the crystal and the film, u_q and u_f are the shear moduli of crystal and film. For a standard quartz crystal, $Z = 9.378 \times 10^5 (d_f u_f)^{-1/2}$. The monitor software solves the equation (2.1) and the film thickness can be measured with high accuracy. The resolution is very high and up to 0.123 angstrom.

When using the QCM, we should set three parameters for the deposited material: density, *d*, acoustic impedance ratio, *Z*, and tooling factor, *T*. Here *d* and *Z* can be found in a factory provided table for most materials. For some alloys with arbitrary components, they can also be calculated. For example, for the antiferromagnet $Ir_{25}Mn_{75}$, our calculated density is 11.35g/cm^3, acoustic impedance ratio is 0.83. The other parameter is tooling factor, $T = T_m / T_x$, where T_m is the actual film thickness on the substrate, T_x is the thickness reading from the QCM. The tooling factor can be defined by actually measuring the film thickness with an Atomic Force Microscope (AFM) and comparing the measured thickness with the QCM readings. The tooling factor can be different for different materials, sputtering sources, chamber geometry, and deposition conditions such as pressure and power.

2.2 Point Contact Setup

Point contacts are very critical for our spin-transfer-torque experiments. The quality of the point contact directly affects the experimental results. Here the quality includes two factors. First, the point contact size should be small enough to provide an extremely high current density. Second, the interface between the point contact and the sample should be as good as possible. Any interfacial damage and defects can cause experiments to fail.

There are a variety of techniques for fabricating point contacts, such as mechanical contacts, e-beam lithographical contact, electrodeposited nanowires, etc. In our lab we use two methods to make point contacts. One is a Focused Ion Beam (FIB) fabricated point contact; the other is a pressure-type mechanical point contact.

First let's look at the FIB fabricated point contact. A focused Ion Beam system uses a finely focused beam of gallium ions. At low beam current modes, the gallium ion beam hits the sample surface and sputters a small amount of material ions and secondary electrons. Sputtered ions and secondary electrons are then collected to form an image. At high beam current modes, a great deal of material can be removed by sputtering, allowing precision milling of the sample down to sub-micron scales. As shown in Figure 2.5, the first step of fabricating point contact is covering the sample by one layer of an insulator and then one layer of a conductor by an e-beam evaporation technique. The insulator is SiO_2, conductor is Cu and both layer thicknesses are usually 200nm. The second step is using the FIB to make a small hole in the insulating layer and expose the sample surface. The opening is typically larger in the Cu layer (500×500 nm) compared to the hole diameter in SiO_2 (200×200nm) to facilitate the following metallization process. The third step is using the FIB to fill the hole with a platinum Pt metal and make an electrical connection between Cu electrode and the sample. One should control the milling depth with a very high precision and just expose the sample surface without damaging it. This can be achieved by monitoring the current through the sample, which is expected to increase when the sample gets exposed.

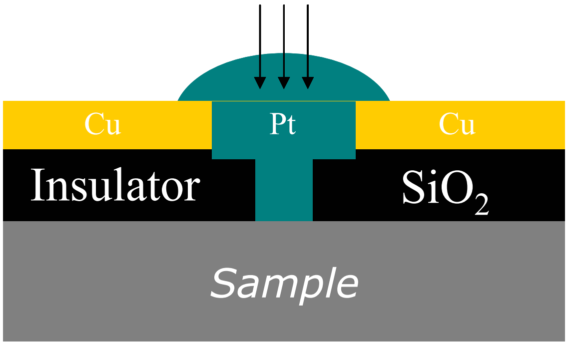

Figure 2.5 Procedure of fabricating point contact with FIB.

Overall, FIB fabricated point contacts are very robust. They are vibration-resistive and can be used at low temperatures. However, the contact size is limited by resolution of FIB and thickness of insulator. In our experiments it is usually bigger than 100nm. Finally the fabrication process takes relatively long time and the yield is low.

The other type of contacts we use in our experiments is mechanical point contact. Here we use a mechanical differential screw to push a sharpened metal tip toward the sample surface and make the point contact. Figure 2.6 shows a detailed view of the mechanical components of the point contact setup. (1) is the framework. It encloses a differential screw (2) and a movable cylinder (3). The differential screw is the most important component. It is responsible for moving the tip slowly and controllably toward the sample surface. The differential screw has two threaded parts. The upper part with thread step 0.75mm is linked with the solid framework (1). The lower part with thread step 0.7mm is linked with the movable cylinder (3). Here the movable cylinder is actually nested in the cylinder of the framework, and it’s free to move in the framework. When rotating the differential screw, the differential screw itself should move toward framework and movable cylinder at different speeds, respectively. Since the framework is the fixed part, the movable cylinder will then move toward the framework to compensate the thread step difference on the differential screw. The thread step difference is very small, only 50 μm, which means one complete rotation of the differential screw displaces the movable cylinder by only

25 μm at room temperature. For our setup, the total range of displacement is about 3mm. A rod (4) is used to rotate the differential screw. The rod is connected to the screw by a fork-blade coupling (5) keeping the vibrations of the rod away from the screw. Part (6) is a small spring which prevents the movable cylinder from turning and introduces an additional damping of the cylinder's vibrations and microdisplacements. The block, including the tip and sample, is tightly connected to the framework by four screws (14). Figure 2.6c shows an exploded view of the block. The spacer (9, 12) and sample table (7) provide a closed space and protect the components inside. The sample (8) is glued on a piece of a microscope slide which is stuck on the table (7) by

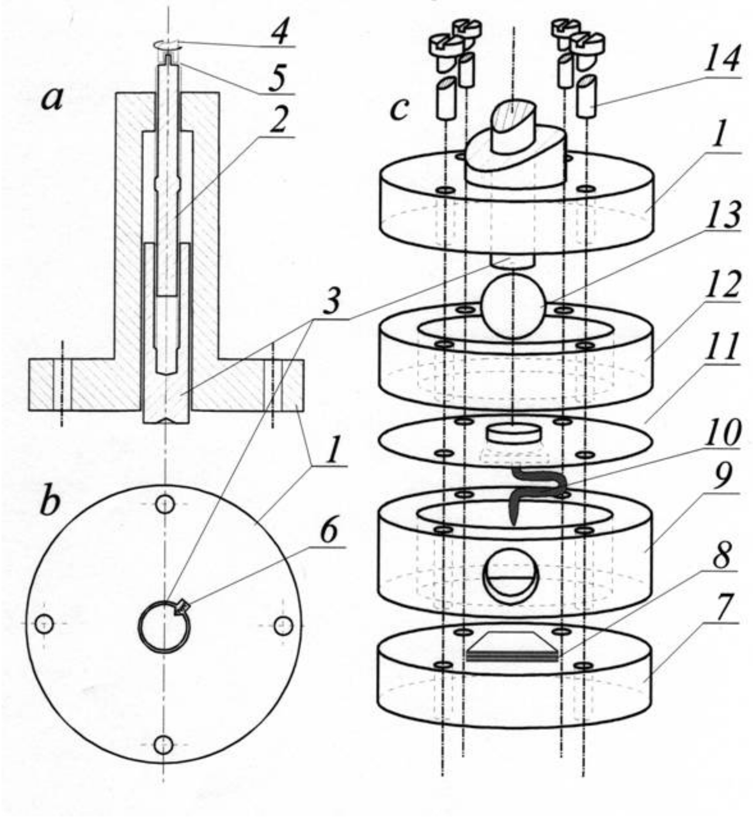

Figure 2.6 The mechanical components of the point contact setup. a) Side view of differential screw mechanism. b) Top view of differential screw and block. c) An exploded view of a block, including the tip (10) and a sample (8). See text for detail.

grease. The sharpened tip (10) is right above the sample. Here the tip is bent to form a spring, which minimizes the damage to the sample when the tip touches it. The tip is soldered on a leaf spring (11). Hence the movement of the cylinder (3) is transmitted through a metallic ball (13) to the leaf spring, and results in moving the tip up and down. The construction of the block allows us to minimize the horizontal displacements of the tip and make a stable point contact. However, our mechanical point contacts are still too fragile and require to be handled with caution. One of the main limitations for such a contact is that it's not compatible with measurements involving temperature variations. A mechanical point contact can't last over large temperature variations (~100 K) due to metal tip's thermal expansion. The mechanical point contact does have many advantages, however, over other techniques, which give it priority in our experiments. It's very easy to make and use. Compared with fabricating point contacts, the mechanical parts are more reliable and less expensive. Usually we can change the tip and make a new contact within one hour, which makes it possible to test many samples in a reasonable time. Also the contact size can be much smaller than a lithographically fabricated contact. We routinely produce contacts with sizes from 1-10 nm, which can not be produced with any other techniques. This feature will allow us to inject extremely high current densities into magnetic multilayers and study spin-transfer phenomena at yet unattained current levels. Additionally, we found that it's easy to control the contact size by Joule heating and perform in-situ size-dependent measurements as will be discussed in Chapter 3.

Below, we will describe the full procedure for making a high quality mechanical point contact. The first and most important step is making the tip. We start from a piece of copper wire, usually 1cm long, 200-250 μm in diameter. On one side, we prepare the wire by covering it with tin to increase the conducting area with the electrode. We use electropolishing to sharpen the other end of the copper wire. The electrolyte is a 45% KOH solution. The negative electrode is connected to stainless steel, which is immersed in the KOH solution. The positive electrode is connected to the copper wire. A DC voltage is applied to the two electrodes. When copper wire is inserted into the KOH solution, the reaction starts and Cu^+ leaves the wire into the solution. The reaction rate generally increases with voltage. So we use the maximum available voltage of our power supply ~18.6V. During the polishing, the current is usually 0.2-0.8A. This process is pretty quick, lasting only a few minutes. After polishing, the tip should be cleaned with DI water, acetone, and alcohol to remove the KOH solution. The polishing and cleaning process might be repeated several times until getting a high quality tip. The sharpened tip should have a very small curvature radius of <<1 μm. Figure 2.7 shows an example of a sharpened copper tip.

The next step is to assemble the tip, sample and other components together. The tip is bent like a spring (Figure 2.6 (10)) and soldered onto the leaf spring. The sample is placed on the table (7). Before tightening everything with screws, we should

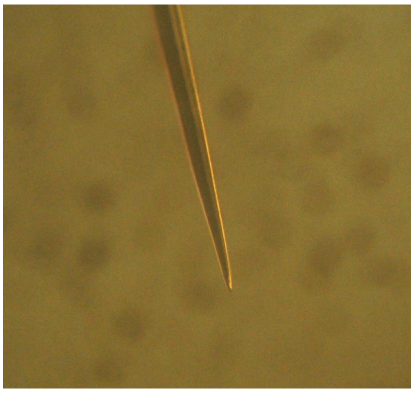

Figure 2.7 Microscopic image of a sharpened copper tip.

manually hold components (7), (9) and (10) together, and do a visual check of the tip-sample separation through the window in the spacer (9). The differential screw can displace the tip by ~3 mm, so we should make sure that the initial separation between the tip and sample is less than that. After assembling the block together, we do the pre-approach process. Here we use an optical microscope to monitor the tip through the window on spacer (9). At a certain angle, we can see the reflected image of tip from the sample surface; it's just opposite to the real tip. By carefully rotating the rod, we approach the tip toward the sample as much as possible before the two tips (one is the image, the other is real) touch each other. A typical tip to sample distance we can get is about 200 μm.

The last step is rotating the rod and finally pushing the tip to make the contact after connecting all the electrical measurement cables. The tip material we use is very soft copper, while the sample is usually mechanically hard thin metallic film on Si wafer. Hence when the tip hits the sample, the soft copper will form a circular contact without damaging the sample. A good contact can be stable for a week or longer.

2.3 Electrical Setup

In this section, we introduce the electrical system for the experiment. For exploring spin transfer phenomena, the easiest and most reliable way is measuring the sample resistance. The reason is that for all spin dynamics in thin films, the relative film magnetizations would vary and induce a resistance change due to the GMR effect. Our electrical system is mainly a bridge circuit with a lock-in amplifier (Figure 2.8). The bridge circuit is a type of electrical circuit where the current splits into two parallel paths. The well known bridge circuit is a Wheatstone bridge, which is used for measuring the resistance. In our electrical setup, we have actually six resistances: R_1~R_4, R_V and R_{PC}. Here R_V is the variable resistance; R_{PC} is the point contact resistance. The bridge circuit is driven by an AC voltage source. Additionally, the point contact is connected with a Keithley DC current source and voltage meter.

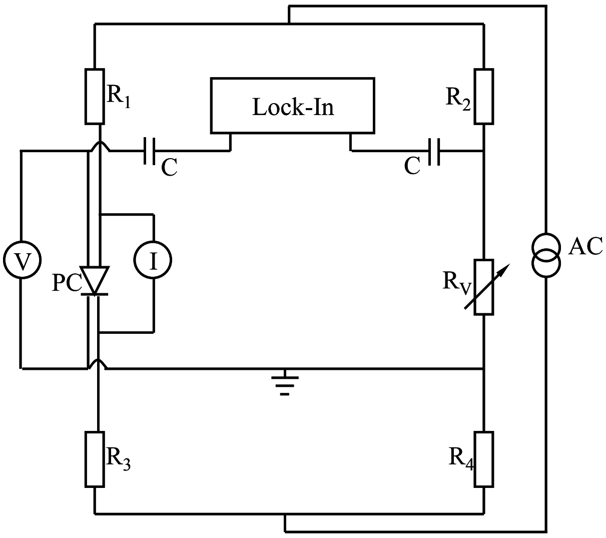

Figure 2.8 Electrical setup for measurement of the point contact (PC) resistance.

They can measure the point contact resistance precisely at a constant bias or sweep the current through the PC to drive spin dynamics. Here we use a four point measurement technique, where there are four leads out from the PC. Two are connected to the tip; the other two are connected to the sample. We take one tip lead and sample lead to drive the current and take the other pair of leads to measure voltage. The four point measurement is especially good for measuring small resistances, where the lead resistance is no longer negligible. Since the voltage meter uses separate leads from the current source, it only measures the voltage drop on the point contact. Hence the resulting resistance rules out the lead resistance.

The resistances R_1~R_4 are carefully chosen so that their real resistances differences are minimal. This is to make the bridge well balanced initially. These resistances can be switched between two values 1kOhm and 10 KOhm. When making the point contact, they are at 10 KOhm to lower the current in the paths and protect the point contact from electrical discharges. After the PC is well formed, they are switched to the 1Kohm level to increase the voltage drop on the PC, hence increasing the signal. The variable resistance has very high precision of 10 mΩ, so it can be as close to the point contact resistance as possible, to balance the bridge. The two capacitors are connected to block any DC current from the lock-in. The capacitor value is chosen to be about $600\,\mu F$, which is big enough to allow any AC current to pass by.

The lock-in amplifier is connected to the bridge circuit after a transformer pre-amplifier and a low noise pre-amplifier. The lock-in amplifier is used to detect and measure the very small AC signal. It uses a phase-sensitive detection (PSD) technique to convert the AC signal to a DC signal output which is proportional to the AC signal amplitude [7]. Here the conversion requires a reference AC signal with a frequency that is not close to any noise frequency, because ideally, only the signal at the reference frequency will result in the DC output. If the noise frequency is very close to the reference frequency, there may be some contribution to the DC output, lowering the signal-to-noise ratio. In our electrical system (Figure 2.8), the lock-in takes the AC voltage source, which drives the bridge, as the reference. We set the AC frequency at 444Hz. By this AC modulation technique, the lock-in can measure the derivative of the point contact resistance. Assuming the AC signal has frequency ω, the total voltage applied on the PC is a function of both DC and AC currents: $V(I + i\cos(\omega t))$. It can be presented as a Taylor series [8]:

$$V(I + i\cos(\omega t)) = V(I) + \frac{dV}{dI} i\cos(\omega t) + \frac{1}{2}\frac{d^2V}{dI^2} i^2 \cos^2(\omega t) + ... \qquad (2.2)$$

The lock-in can measure the first derivative dV/dI by locking the frequency at ω and the second derivative d^2V/dI^2 at 2ω and so on.

Below we show the procedure for establishing the point contact (PC), balancing the bridge circuit, and setting the lock-in parameters for further measurements. The first step is safely touching the tip to the sample and making a good contact. It's a very critical step for the rest of the measurements. The problem is that when the tip is very close to the sample surface, the voltage across this semi-insulating gap can be extremely big and electrical discharge between the tip and the sample would be very damaging to the sample right underneath the tip. To avoid this electrical damage, we optimize the process of establishing the PC as follows. The DC current source is initially disconnected from the PC to lower the background current. The AC voltage source is tuned to lowest value 4mV, which gives only a few micro-amperes of current in the bridge paths. The bridge resistance R_1~R_4 are all switched to 10K to further lower the bridge currents. Moreover, an additional resistor is connected in parallel to the PC. This protection resistance value is chosen to be 1 kOhm so that it will attract most of the current flow when the semi-insulating gap in PC gives several kilo-Ohms, and afterwards it will not lower the PC signal much since the final PC resistance is usually tens of ohms. Additionally, all parts should be grounded to eliminate any electrostatic discharge.

Next, we should switch R_1~R_4 to 1Kohm and balance the bridge circuit. The balancing procedure includes two parts. One is varying the variable resistance R_V to match the PC resistance, so that the lock-in X and Y channel have minimum output. The other is balancing the phase $\theta = \theta_{sig} - \theta_{ref}$ of the lock-in. The lock-in X channel indicates the 'in-phase' component which is proportional to $\cos\theta$, and Y channel indicates the 'quadrature' component which is proportional to $\sin\theta$ [7]. We tune the θ_{ref} to make most of the signal vector magnitude located in the X channel. On the lock-in, the time constant should be chosen properly. For a big time constant, the response to the real data is slow, so it might not catch the very fast changes in the real data. However, the advantage for a big time constant is that when there are noise pulses coming in, only small fluctuations will be on the real data or we say it is a good resistor of the external noise. For a small time constant, it responses is fast, but also can pick up all fast noise. Usually the time constant should be set $\tau \approx T_s / 3$ [9], where T_s is the sampling time, so that the noise is averaged out, but the signal features, such as steps and peaks, are preserved. Also the time constant should satisfy $\tau \geq \frac{1}{f_{ref}}$ in order to have a high signal-to-noise ratio, where f_{ref} is reference frequency. In our measurements, for example, the sampling time for current induced spin wave excitation is about 1000 ms. The inversed reference time is 1/444=2.5ms. So we choose the lock-in time constant at 300ms. With all of these optimizations, the signal-to-noise ratio can reach the optimal value of about 10^5 in our system, so that changes in the PC resistance of the order of $\Delta R / R = 10^{-3}$ could be measured with an accuracy of 1%.

2.4 References

[1] J. D. Plummer, M. D. Deal, and P. B. Griffin, *Silicon VLSI Technology: Fundamantals, Practics and Modeling*, Pearson Education, Inc., P511, P551 (2003)

[2] Online application notes from Alacritas Consultancy Ltd.

http://www.alacritas-consulting.com/sputter_deposition_for_thin_films.html

[3] K. Wasa, M. Kitabatake, H. Adachi, *Thin Film Materials Technology: Sputtering of compound materials*, William Andrew, Inc. P19 (2004)

[4] Online class notes:

http://www.uccs.edu/~tchriste/courses/PHYS549/549lectures/sputtertech.html

[5] *XTM/2 Deposition Monitor Operation Manual*, INFICON, **5-4**

[6] C. Lu, and O. Lewis, *J. Appl. Phys.* **43**, 4385 (1972)

[7] Stanford SR830 DSP Lock-In Amplifier User Manual

[8] Yu. G. Naidyuk, and I. K. Yanson, arXiv:physics/0312016, (2003)

[9] J. W. Huang, Ph.D Thesis, The University of Texas at Austin, (2007)

Chapter 3

Spin Transfer Phenomena in Ferromagnetic Multilayers

The magnetic state of a ferromagnet can be altered by an electrical current. For instance, the current was shown to induce spin waves, precession, and reversal of magnetization in magnetic nanostructures. Today a variety of experimental techniques provide a vast amount of data on such current-induced excitations. A typical experiment usually exploits dc resistance measurements to detect the excitations. In addition, high-frequency techniques can provide valuable information on frequencies of the current-induced spin waves. Probing wavelengths of the excitations, however, represents an experimental challenge. Point contacts were instrumental both for our original observation of current-induced excitations and in providing the first data on frequencies of the current-induced spin waves. In the present work we demonstrate that point-contact technique can also provide valuable information on the wavelengths of spin waves induced by the current. By varying the size of point contacts we have been able to control the size of the excitation volume and therefore the wavelength of current-induced spin waves. This leads to a technique with in situ sensitivity to wavelengths of current-induced excitations. The detailed size-dependent measurements of the current-induced excitations display an interesting relation between current and voltage thresholds for such excitations.

3.1 Introduction

Since in this chapter we will discuss the spin transfer phenomena in magnetic multilayers, it's necessary to introduce some properties of such multilayer. The usual type of magnetic multilayers is $(F/N)_n$ where F is ferromagnetic transition metal (Fe, Co, Ni and their alloys), N is non-magnetic metal (Cu, Ag, Cr, etc.), n is the number of F/N bilayers in the multilayer film. The first GMR effect was found in magnetic multilayers [1, 2]; while the trigger for this finding was the discovery by Grunberg's group [3] that in Fe/Cr/Fe trilayers the two Fe layers can be coupled antiferromagnetically across a thin Cr layer. Then Parkin et al. extended the study of exchange coupling in magnetic multilayers to other material combinations and a wide range of N-layer thicknesses [4, 5]. They have found an oscillatory variation of the magnetoresistance as a function of the N-layer thickness, which reflects the fact that the exchange coupling between F layers oscillates instead of decreasing monotonically as N thickness increases.

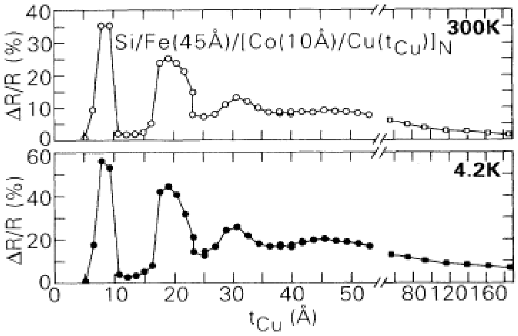

Figure 3.1 Magnetoresistance versus Cu spacer thickness for $[Co(10Å)/Cu(t_{cu})]_N$. where N=16 for t_{cu}<55Å (open circles for 300K and filled circles for 4.2K) and N=8 for t_{cu}>55Å (open squares for 300K and filled squares for 4.2K) [5].

Figure 3.1 shows such oscillations in Co/Cu multilayers. At Cu layer thickness less than 55Å, the MR rises when the F layers have antiferromagnetic coupling, whereas ferromagnetic coupling causes the F layer magnetizations to be parallel to each other, inhibiting any MR. The period of oscillation is about 10Å and increase slightly with Cu layer thickness. At Cu layer thickness more than 60Å, the interlayer exchange coupling decreases rapidly with increasing Cu thickness. So the MR shows a monotonic decrease. The underlying mechanism of these MR oscillations is RKKY (Ruderman-Kittel-Kasuya-Yosida) coupling between F layers. In 1954, Ruderman and Kittel [6] first suggested that magnetic moments can polarize electrons in a non-magnetic host metal. A few years later Kasuya [7] and Yosida [8] extended this concept to the localized rare earth materials. In a magnetic multilayer, the non-magnetic spacer is polarized by magnetic atoms situated at the F/N interfaces. This polarization oscillates and induces an oscillatory coupling in the direction perpendicular to the layer. In the simplest case of free electron approximation, the RKKY exchange coupling constant J is proportional to $\frac{\cos(2k_F R)}{R^2}$, where k_F is Fermi wave vector and R is the non-magnetic layer thickness. This simple form of J indicates that the coupling oscillates with a period of $\lambda_F / 2 \approx 1$ monolayer and decays as $1/R^2$. This oscillation period is much shorter than the experimental observation where the oscillation period is about 10Å. To be consistent with the experiment, the RKKY model was developed with the possible quantization of spacer thickness [9].

For our studies of spin transfer phenomena, the $[F/N]_n$ magnetic multilayer will be one of two multilayer structures; the other being an exchange biased spin valve structure which we will describe in Chapter 4. The first experimental observation of spin transfer effect was done by Tsoi et al. in $(Co/Cu)_n$ multilayers [10]. In this experiment a high-density electric current was injected into Co/Cu multilayer through a mechanical point contact between a sharpened Ag tip and the multilayer.

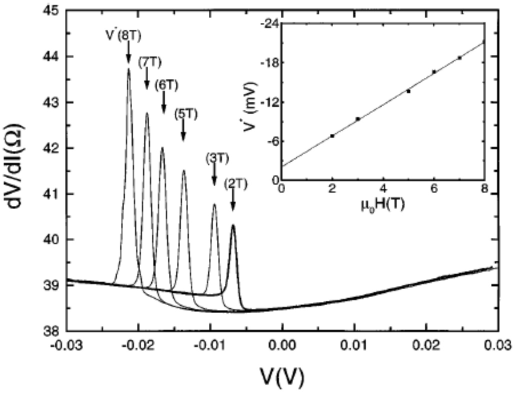

Figure 3.2 The point contact *dV/dI(V)* spectra for a series of magnetic fields (2, 3, 5, 6, 7, and 8T) revealing an upward step and a corresponding peak in *dV/dI* at a certain negative bias voltage $V^*(H)$. The inset shows that $V^*(H)$ increases linearly with the applied magnetic field H [10].

The current density was $\sim 10^9 A/cm^2$ which was high enough to induce the magnetization precession. Figure 3.2 shows curves of the differential point-contact resistance *dV/dI* versus the dc bias voltage taken at different values of magnetic field applied perpendicular to the plane of the multilayer at liquid helium temperature (4.2K). The peak indicates where spin-wave excitation starts. This excitation causes the F layer magnetizations to be tilted from parallel alignment. Hence the point contact resistance has a step increase which is shown as a peak in the differential resistance signal. The critical bias voltage, where this peak appears, increases linearly with the magnetic field from 2T to 8T. This linear dependence agrees with Slonczewski's spin torque model. His model leads to a prediction that the critical current depends on the magnetic field (greater than the multilayer saturation field) linearly as [11]:

$$I_c = \frac{et_1}{\hbar\varepsilon}\left[23.4A + 6.31a^2\alpha_G M_s B_{eff}\right] \tag{3.1}$$

where t_1 is the thickness of the excited layer. ε is the spin polarization efficiency parameter which reflects that the electrons in Co are not fully spin-polarized, A is the exchange stiffness for Co, a is the point contact radius, α_G is the Gilbert damping parameter, M_s is the Co saturation magnetization, and B_{eff} is the effective field including the applied field, demagnetization field, interlayer exchange field and anisotropy field.

A simple model to understand this spin wave excitation behavior is based upon the conservation of energy and angular momentum. Using the two-channel model [12], where the spin-up and spin-down electrons carry current independently in parallel, one can show that electrochemical potentials of two spin-states may be different near interfaces between F and N metals due to spin accumulation. For electrons flowing from N into F, the spin-down electron potential is higher than the spin-up potential at the F/N interface. So when spin-down electrons flip their spins, the released energy can be used for spin-wave excitation. At the same time a loss in F-layer's angular momentum for the majority direction (due to spin waves) is compensated by an increase in polarization of conduction electrons.

A mechanical point contact is a very efficient probe of electrical transport in extremely small sample volumes because of its small size (<10nm). This qualifies point contact as the smallest probe of spin transfer phenomena today. This by itself is an excellent motivation for exploring point contact excitations in magnetic multilayers. In addition, we want to extend the capabilities of our point-contact technique to include the sensitivity to wavelengths of the current-induced spin waves. In early measurements of high frequency (5-60GHz) current-induced magnetization precession [13-15], the dependence on the lateral device area or point contact area has not been examined. However understanding the size dependence is important for determining the details of precession dynamics since the wavelength of the current-induced spin waves is predicted to depend on the contact size [11]. So a point contact with a controllable size is highly desirable for detailed size-dependent measurements of current-induced excitations.

In this chapter we will show first a point-contact experiment exploring spin transfer effect in magnetic multilayers at room temperature and then an experiment in which we have probed the wavelength of current-induced excitations with a size-variable point contact.

3.2 Experiment

Our samples were $(Co/Cu)_n$ multilayer films prepared by sputter deposition.

The bilayer number *n* ranges from 20-50 and layer thickness t_{Co}=1.5nm, t_{Cu}=2.0-2.2nm. The Cu tip was made using the procedure described in Chapter 2.2. The measuring system is shown in Chapter 2.3. All the measurements are done at room temperature. With the magnetic field applied perpendicular to the film plane and dc bias applied to the contact (Figure 3.3a) two main measurements can be preformed: current-voltage characteristics (I-V) at certain applied magnetic field B and magnetoresistance (MR) at certain dc bias current. In IV measurement, the point contact resistance R and the differential resistance dV/dI are measured when sweeping the bias current at fixed magnetic field. In MR measurement, the static contact resistance R=V/I is measured when sweeping the applied magnetic field at fixed dc bias current. These two types of measurements were performed on point contacts (see Figure 3.3b) of different size. The point-contact size could be continuously varied from a few nanometers to a few tens of nanometers as described next.

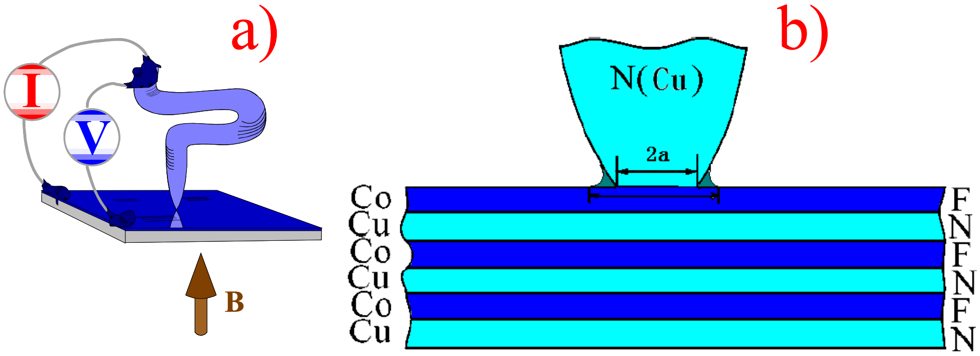

Figure 3.3 Schematic diagram of point contact system with size dependent measurement capabilities. a) The dc bias current and applied magnetic field is perpendicular with the sample surface. b) After establishing the contact between the tip (Cu) and the sample surface, the contact size can be varied by further pressing the tip to the multilayer film. Here *a* is the contact radius.

After establishing a small (*a* ~ few nanometers) point contact between the Cu tip and the multilayer film, the contact size can be increased by further pressing the tip to the multilayer film. The extent of damage to the film is determined by relative mechanical strength of the tip and the film. We choose soft material (Cu) for the tip to minimize the damage to the sample and constrain most of deformations within the tip. Experimentally the pressure from leaf spring and the spring like bent tip (Figure 2.6) is hard to control. One of the main disadvantages of mechanical point contact is the instability. Usually it takes several hours for established point contact to be stable enough for measurements at room temperature. So it is not wise to mechanically add more pressure on this very sensitive setup after the contact was initially established and stabilized. A practical method to vary the contact size consists of further softening the Cu tip. We applied high enough dc current through the tip to heat it up. As a result, the Cu tip softens more, deforms, and produces a larger contact to the more mechanically rigid film. This is an irreversible process where we can only increase the contact size. So when establishing the point contact, we try to establish a contact with a relatively high initial resistance (small contact size). Then by heating the point contact we lower the contact's resistance in small steps. For each new point-contact resistance value we measure IV and MR characteristics.

3.3 Spin-Transfer-Torque Effect in Magnetic Multilayers at Room Temperature

Our magnetic multilayers, with Cu spacer ~2nm thick, are located near the second antiferromagnetic coupling peak in Co/Cu systems (see Fig. 3.1). The film's easy magnetization axis is determined by a competition between the magneto-crystalline anisotropy and the shape anisotropy [18]. With 1.5nm Co layer thickness, the shape anisotropy dominates. So at zero applied field magnetizations of our Co layers have antiferromagnetic in-plane alignment. With the applied magnetic field, we can saturate all the film magnetizations to be parallel. To saturate the film in the perpendicular-to-plane direction one needs to apply magnetic field of about 1.5T. Figure 3.4 shows the IV measurement of current-induced excitations in perpendicular magnetic field. To our knowledge, this is the first point contact excitation of spin waves at room temperature. Here the point contact resistance is ~11ohm; the resistance R and differential resistance dV/dI are measured as a function of the bias current. The spin-transfer-torque excitation can be seen for a certain negative bias current (~-2.1mA), but not for positive ones. Since the current spreads out rapidly into the multilayer, only a few layers under the point contact are considered to have high enough perpendicular current density for the excitations. The precession of magnetic moments in F-layers leads to a non-zero angle between excited layer magnetizations and fixed layer magnetizations; and due to GMR effect, we observe a step increase in the contact resistance R. This sharp resistance change can also be monitored by a lock-in technique in differential resistance of the contact. The dashed line in Fig. 3.4

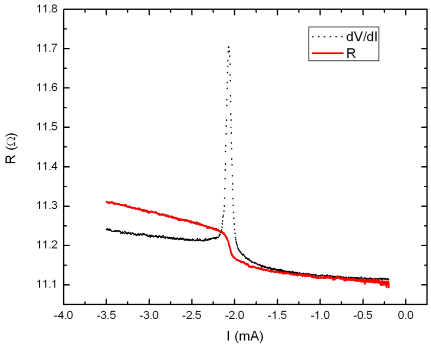

Figure 3.4 Point contact I-V characteristic curves. Red curve is the contact resistance R versus dc bias current. The negative current is defined as electrons flow from tip rapidly into the multilayer films. At critical current (~-2.1mA) the steady precession of magnetization is excited and resistance R has a step increase. The corresponding dV/dI signal has a peak (dashed line) at the critical current.

is the corresponding dV/dI signal versus bias current. At the critical current it shows a nice peak which provides us a more accurate definition of the critical current value. In the following, we investigate how this critical current evolves as a function of applied fields and contact size.

For field dependent measurements, we sweep the field from 3T to 9T with 0.5T step. At each applied field, we measure the resistance R and the differential resistance

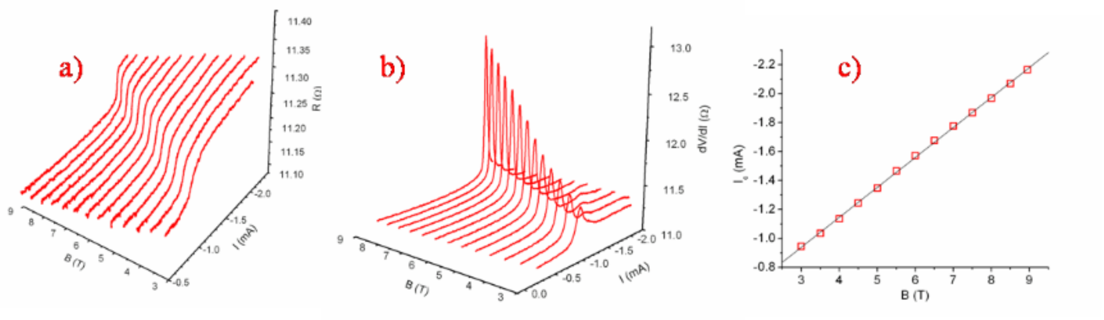

Figure 3.5 Field dependent measurements of point contact I-V characteristics for magnetic multilayers. a) Contact resistance R versus I curves at applied fields from 3T to 9T. b) Differential resistance dV/dI versus I curves at applied fields from 3T to 9T.

c) Critical current versus applied fields. Black line is the linear fit for guidance.

dV/dI signals as a function of bias current I. Figure 3.5a shows the resistance R versus I curves at different applied field. Figure 3.5b shows dV/dI signal versus I curves. The critical current, found from the dV/dI peak locations, increases linearly with the applied field (Figure 3.5c) in good agreement with Slonczewski's model (Equation 3.1). We find that the step increase in resistance is sharper at higher magnetic field where the corresponding peak has a higher magnitude and narrower width. The possible reason is that with higher critical current, the current induced spin torque is more efficient in exciting magnetic moments from their initial states to precessional states.

The above measurements are performed in a high magnetic field which is higher than the saturation field. At low magnetic field, the behavior of F-layer magnetic moments is complicated, including both magnetization switching and in-plane precession. The systematic picture for low field spin transfer phenomena in magnetic multilayers is shown in Figure 3.6a. This is a 2D color plot where the dV/dI(I) spectra are color coded and plotted as a function of applied magnetic field. Red color indicates higher dV/dI signal and blue indicates lower. The current (the x axis) is swept from +4.0mA to -4.0mA and back to +4.0mA. The magnetic field (the y axis) is stepped up from -0.5T to +0.5T. The contact resistance is higher at high bias current magnitude (parabolic background) due to Joule heating of the contact, which does not exceed a few degrees at the highest applied currents. There are two typical features in this plot. At field around 0.2~0.4T, some magnetizations are tilted up from the in-plane direction by the applied field. Hence the current induced spin torque excites magnetization precession with both in-plane and out-of-plane components. In

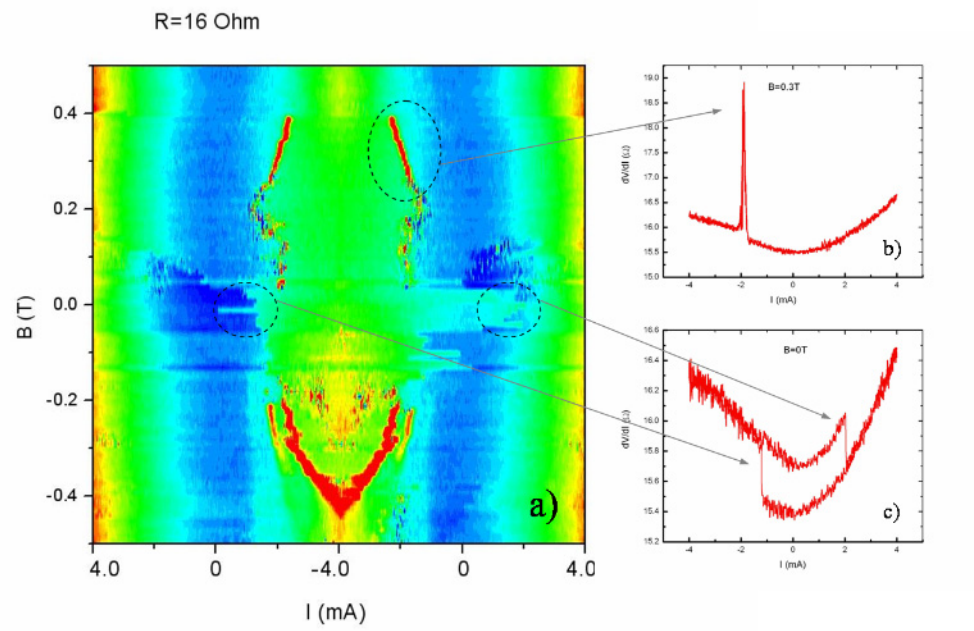

Figure 3.6 Low field spin transfer phenomena in magnetic multilayers. a) 2D color plot for dV/dI(I) spectra as a function of magnetic field. Red and blue indicates higher and lower dV/dI signal. b) dV/dI spectra at B=0.3T. The peak appears when the precession is excited. c) dV/dI spectra at zero magnetic fields. The magnetization switching happens at critical current on both directions.

2D plot the corresponding dV/dI peaks are shown as red spots. If we take one sweep out and re-plot as I-V curve for B=0.3T (Figure 3.6b), the curve shows a reversible peak structure which is similar to the high field curve shown in Figure 3.4. At fields around zero, the spin transfer torque is big enough to switch magnetizations of F-layers completely. It’s shown as an abrupt color change in Figure 3.6a. Figure 3.6c is the I-V curve taken at B=0T, which shows the switching behavior with hysteresis. The critical current at negative side switches the layer magnetizations from parallel to antiparallel, and contact resistance jumps up. On the back way, the positive critical current switches the magnetizations back to parallel state, and the resistance jumps down.

3.4 Probing Wavelengths of Current Induced Excitations in Point Contact Experiments

Till now all the point-contact measurements of magnetization dynamics were performed at a certain fixed contact resistance (size). In the following we perform all these measurements on contacts with a continuously and controllably varied size. The will allow us to investigate the size-dependence of the current-driven magnetization dynamics.

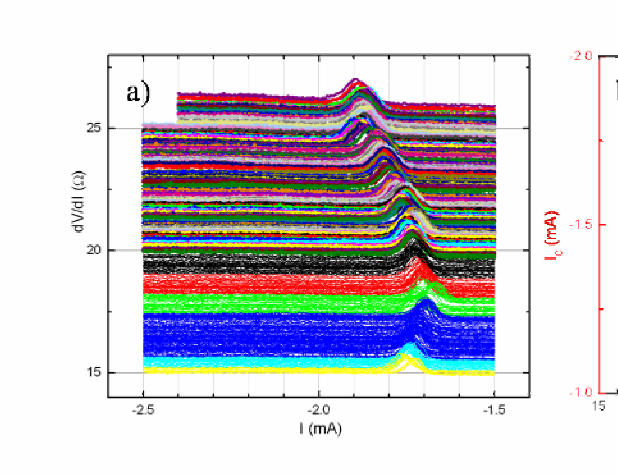

Figure 3.7 Resistance dependent measurements of current induced spin wave excitations in magnetic multilayers. a) Point contact dV/dI(I) spectra for contact resistance varies from 26Ω to 15Ω. b) Critical current I_c (red circles; left scale) and corresponding voltage V_c (black squares; right scale) as a function of the contact resistance R (equivalent to contact size) for fixed B=5T.

Figure 3.7a shows the dV/dI(I) spectra for a contact whose resistance is lowered from 26Ω to 15Ω at a fixed magnetic field B=5T. The peaks indicate the onset of spin-transfer-torque excitations and provide the values of critical currents and corresponding voltages. Figure 3.7b shows the variation of the critical current I_c and the corresponding voltage V_c as a function of the contact resistance R (equivalent to contact size) for B=5T. The voltage V_c is a measure of energy for nonequilibrium electrons in the contact region, which may be energetic enough to excite spin waves alone. Assuming the combination of ballistic and diffusive scattering, the contact size can be estimated from the contact resistance using Equation 1.12. In Figure 3.7b, this interpretation would give the contact size ranging from 5nm (R=26Ω) to 8nm (15Ω). Note that in this region, I_c varies by less than 11% while V_c varies by as much as 45%. Assuming that at constant B we are exciting spin waves of a constant energy, this observation unambiguously identifies the current (not voltage) as the driving force for spin wave excitations. To our knowledge this is the first direct proof that "current-driven excitations" are actually current- and not voltage- driven. For large contact sizes (low Rs), I_c increases with decreasing R due to a rapid decrease in current density. For small contacts (high Rs), increase in I_c with increasing R indicates that the spin-wave energy increases due to a shorter wavelength excited in smaller contacts [11].

With our technique to vary the point contact size, the wavelength of excited spin waves can be recovered from the slope of $I_c(B)$ (Figure 3.5c). By measuring the dV/dI(I) spectra as a function of applied field for each contact resistance (size), we were able to get the Ic(B) curve for a point contact whose resistance ranges from 10.8Ω down to 2.4Ω (Figure 3.8). By linearly fitting the I_c(B) dependence at each resistance value, we could obtain the slope and intercept for each linear fit. We also

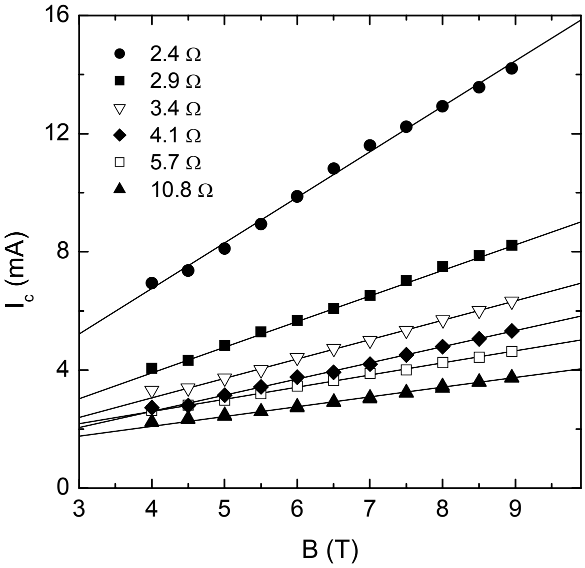

Figure 3.8 I_c versus B for the point contact resistance decreases from 10.8Ω to 2.4Ω. Solid lines are the linear fit for I_c(B) relation at each resistance.

estimated the contact radius from contact resistance using Sharvin-Maxwell method (Equation 1.12) and assuming that at room temperature $\Gamma(l << a) = 1$. The results for contact radius *a*, slope α, and intercept β for each resistance R are listed in Table 3.1. We use these experimental data to get the wavelengths of excited spin waves and compare the results with estimated contact radiuses to verify Slonczewski's prediction that the wavelength should comparable to the contact size. There are several models providing the $I_c = \alpha' B_{app} + \beta'$ relation. Here α', β' are theoretical calculated slope and intercept. They could be the functions of wavelength λ where we can figure out the wavelength by substituting the experimental slope or intercept value for each resistance.

R (Ω)	a (nm)	$\alpha\left(\times 10^{-4} A/T\right)$	$\beta\left(\times 10^{-4} A\right)$
10.8	8.03	3.30	7.78
8.7	9.2	4.43	8.89
5.7	11.96	4.10	9.57
4.1	15.12	5.46	4.19
3.4	17.22	6.57	4.29
2.9	19.28	8.68	4.85
2.7	20.3	17.8	3.88
2.36	22.39	15.4	6.0

Table 3.1 Contact radiuses, Ic(B) relation linear fit slopes and intercepts for each resistance.

The first model we use is Slonczewski's spin torque model [11]. He calculated the spin torque on the multilayer magnets and used it in the LLG equation for spin transfer torque term to derive I_c as a function of field and contact radius. Here we rewrite equation 3.1 to clearly identify α', β' terms:

$$I_c = \underline{\frac{et_1}{\hbar\varepsilon}6.31a^2\alpha_G M_s} B_{app} + \underline{\frac{et_1}{\hbar\varepsilon}23.4A - \frac{et_1}{\hbar\varepsilon}6.31a^2\alpha_G M_s \mu_0 M_s} \qquad (3.2)$$

where we assume $B_{eff} = B_{app} - \mu_0 M_s$ with exchange field, anisotropy field both zero.

Using SI units, t_1=1.5×10^{-9}(m) for Co layer thickness, $\varepsilon = 0.5$ which reflects the electrons are not fully spin polarized in Co, damping parameter $\alpha_G = 0.05$, exchange stiffness A=1×10^{-11}*J/m* for Co, and the saturation magnetization for Co is M_s=1.45×10^{6} *A/m*. Then we can calculate the α', β' with all this parameters:

$$\begin{aligned}\alpha' &= \frac{1.6\times10^{-19}(C)\times1.5\times10^{-9}(m)}{1.05\times10^{-34}(J\cdot s)\times0.5}\times6.31\times10^{-18}a^2\times0.05\times1.45\times10^{6}(A/m)\\ &= 2.09\times10^{-6}a^2(nm)^2\end{aligned} \tag{3.3}$$

$$\begin{aligned}\beta' &= \frac{1.6\times10^{-19}(C)\times1.5\times10^{-9}(m)}{1.05\times10^{-34}(J\cdot s)\times0.5}\times23.4\times1.0\times10^{-11}(J/m)\\ &-\frac{1.6\times10^{-19}(C)\times1.5\times10^{-9}(m)}{1.05\times10^{-34}(J\cdot s)\times0.5}\times6.31\times10^{-18}a^2\times0.05\times(1.45\times10^{6}(A/m))^2\times12.566\times10^{-7}(N\cdot A^{-2})\\ &=1.07\times10^{-3}-3.8\times10^{-6}a^2(nm)^2\end{aligned} \tag{3.4}$$

Now we can have Ic(B) relation with α', β' as a function of contact radius *a*:

$$I_c(A) = \underline{2.09\times10^{-6}a^2(nm)^2}\,B_{app}(T) + \underline{1.07\times10^{-3}-3.8\times10^{-6}a^2(nm)^2} \tag{3.5}$$

where the contact radius *a* is assumed to determine the excited wavelength. Hence in our calculation we consider radius *a* equivalent to the wavelength λ. Since both α', β' are the function of wavelength, we can use either slope or intercept to get the wavelength respectively.

From slope: $\lambda = a = \sqrt{\dfrac{\alpha}{2.09\times10^{-6}}}(nm)$, where α is the slope of linear fit for experimental data (Table 3.1).

From intercept: $\lambda = a = \sqrt{\dfrac{1.07\times10^{-3}-\beta}{3.8\times10^{-6}}}(nm)$, where β is the intercept of linear fit for experimental data (Table 3.1).

Another model we use for wavelength calculation assumes the following dispersion of spin waves in our films:

$$\hbar\omega = g\mu_B(B_{app} - \mu_0 M_s) + D\left(\frac{2\pi}{\lambda}\right)^2 \qquad (3.6)$$

where $\hbar\omega$ is the spin wave energy, Lande factor g=2.170 for Co, $\mu_B = 0.5788\times10^{-4} eV/T$ is Bohr magneton. Stiffness parameter D=510 meVÅ^2. For energy conservation, the energy required to excite a spin wave is actually the energy splitting of spin-up and spin-down electrochemical potentials at the F/N interface. We calculate this splitting $\Delta\mu$ using two different expressions as discussed next.

In the initial observation of current-driven excitations [10], the electrochemical potential difference $\Delta\mu$ was deduced from the solution of the diffusion equation given by van Son et al. [19]:

$$\Delta\mu = ej\frac{2(2\alpha_F - 1)(\sigma_N^{-1}\Lambda_N)(\sigma_F^{-1}\Lambda_F)}{(\sigma_F^{-1}\Lambda_F) + 4\alpha_F(1-\alpha_F)(\sigma_N^{-1}\Lambda_N)} \qquad (3.7)$$

where j is the current density, σ_F and σ_N are F and N conductivities, Λ_F and Λ_N are spin diffusion lengths in F and N, α_F is the spin asymmetry coefficient in F. Choosing the room temperature parameter for Co/Cu multilayer: $\sigma^{-1}{}_F = 238 n\Omega m$, $\sigma_N{}^{-1} = 29 n\Omega m$, $\Lambda_F \approx 15 nm$, $\Lambda_N \approx 350 nm$, and $\alpha_F = 0.75$, we get $\Delta\mu = j\times3.24\times10^{-15}(eV)$. The emission of spin wave is possible only when this potential difference $\Delta\mu$ is bigger than $\hbar\omega$. Assuming that at threshold $\Delta\mu = \hbar\omega$, we find the following relationship between the critical current and applied field:

$$\Delta\mu = \frac{I_c}{\pi a^2}\times 3.24\times 10^{-15}(eV) = \hbar\omega = g\mu_B(B_{app}-\mu_0 M_s) + D\left(\frac{2\pi}{\lambda}\right)^2 \qquad (3.8)$$

We rewrite equation 3.8 to have form $I_c = \alpha' B_{app} + \beta'$:

$$I_c = \frac{g\mu_B \pi a^2}{3.24\times 10^{-15}} B_{app} + \frac{4\pi^3 D a^2}{3.24\times 10^{-15}\lambda^2} - \frac{g\mu_B\mu_0 M_s \pi a^2}{3.24\times 10^{-15}} \qquad (3.9)$$

With the parameters given above, the calculated results for α', β' are:

$$\alpha' = \frac{2.170\times 0.5788\times 10^{-4}(eV/T)\times 3.14\times 10^{-18} a^2 (nm)^2}{3.24\times 10^{-15}} = 1.22\times 10^{-7} a^2 (nm)^2 \qquad (3.10)$$

$$\begin{aligned}\beta' &= \frac{4\pi^3\times 510\times 10^{-23}(eV\cdot m^2)\times a^2(nm)^2}{3.24\times 10^{-15}\times \lambda^2 (nm)^2}\\ &- \frac{2.170\times 0.5788\times 10^{-4}(eV/T)\times 12.566\times 10^{-7}(N\cdot A^{-2})\times 1.45\times 10^{6}(A/m)\times 3.14\times 10^{-18} a^2 (nm)^2}{3.24\times 10^{-15}} \qquad (3.11)\\ &= \frac{1.95\times 10^{-4} a^2 (nm)^2}{\lambda^2 (nm)^2} - 2.22\times 10^{-7} a^2 (nm)^2\end{aligned}$$

Here only β' is the function of wavelength, which can be used to calculate λ:

$\lambda = \sqrt{\dfrac{1.95\times 10^{-4}\times a^2}{\beta + 2.22\times 10^{-7}\times a^2}}(nm)$, where a is the contact radius from Equation 1.12 and β is the intercept of linear fit for experimental data (Table 3.1).

Another method to calculate $\Delta\mu$ can be adopted from Berger's work [20], where he assumed the energy difference $\Delta\mu$ between spin-up and spin-down currents is from local Fermi level difference due to non-equal Fermi surface shift in k space for two current channels. The resulting expression for $\Delta\mu$ is:

$$\Delta\mu = 2\left(\frac{\alpha_1 - 1}{\alpha_1 + 1}\right) j \frac{\hbar k_N}{e n_N} \qquad (3.12)$$

where $\alpha_1 = \sigma^{\uparrow}/\sigma^{\downarrow} = 3$ is the asymmetry parameter, here $\sigma^{\uparrow}, \sigma^{\downarrow}$ are the spin-up and spin-down conductivities in F; *j* is current density, $k_N = 1.36\times10^{10} m^{-1}$ is wave vector in Cu, and $n_N = 8.5\times10^{28} m^{-3}$ is electron density in Cu. With all these parameters, we get $\Delta\mu = j\times1.32\times10^{-15}(eV)$. Following a similar procedure as for Equation 3.8, we figure out the Ic(B) relation:

$$I_c = \underline{\frac{g\mu_B\pi a^2}{1.32\times10^{-15}}}B_{app} + \underline{\frac{4\pi^3 Da^2}{1.32\times10^{-15}\lambda^2} - \frac{g\mu_B\mu_0 M_s\pi a^2}{1.32\times10^{-15}}} \qquad (3.13)$$

Again only β' is the function of wavelength:

$$\beta' = \frac{9.57\times10^{-4}a^2(nm)^2}{\lambda^2(nm)^2} - 10.9\times10^{-7}a^2(nm)^2 \qquad (3.14)$$

So λ can be calculated: $\lambda = \sqrt{\frac{9.57\times10^{-4}\times a^2}{\beta+10.9\times10^{-7}\times a^2}}(nm)$, where *a* is the radius from Equation 1.12, β is the intercept of linear fit from experiment (Table 3.1).

After calculating the wavelength for all the measured resistances (from 10.8Ω to 2.4Ω) with four different models, we compare the results with the contact radiuses from Sharvin-Maxwell (S-M) equation in Figure 3.9. The solid line shows how the contact radius *a* depends on resistance R according to S-M relation. The filled symbols are the wavelength of current driven spin wave calculated from Slonczewski's spin torque model. The filled squares are the wavelengths we obtain from slope of the I_c(B) linear fits. They are all bigger than the contact radius. The filled triangles are the wavelengths we got from intercept of the I_c(B) linear relations. Most of them are smaller than the contact radius. The possible reason for that is the following: when calculating the effective field $B_{eff} = B_{app} - \mu_0 M_s$, we assumed the saturation magnetization M_s is fully out-of-plane. However, in reality, the magnetization is precessing and tilted away from the out-of-plane or perpendicular direction. So the *Ms* should be only the perpendicular component of magnetization and is smaller than saturation magnetization. This means our calculated wavelengths from intercept are smaller than they should be which are closer to the contact radius.

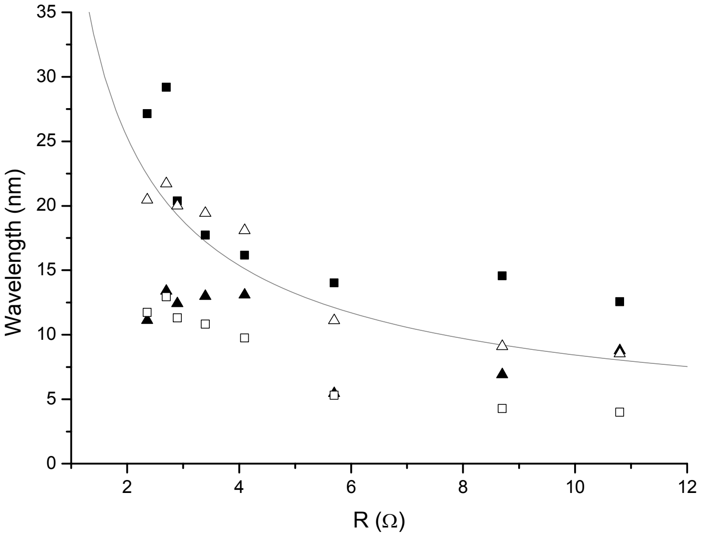

Figure 3.9 Wavelength of current driven spin wave versus contact resistance R. Filled square is the wavelength calculated from Slonczewski's spin torque model using slope α. Filled triangle is also from spin torque model but using intercept β. Open square is calculated from spin wave energy conservation with Δμ provided by van Son. Open triangle is the result from Berger's model for Δμ. Solid line shows how the contact radius *a* depends on R with Sharvin-Maxwell relation.

The open symbols are the wavelengths calculated from $\Delta\mu = \hbar\omega$ condition. The open squares are the wavelengths obtained for $\Delta\mu$ from van Son's model. They are all smaller than the corresponding contact radiuses. Since here we assume the 100% efficiency of converting $\Delta\mu$ into spin wave energy, it is natural to assume that such a high efficiency can not be realized in our room temperature experiment and the actual wavelength should be somewhat longer for lower efficiency and, therefore, closer to the S-M curve. The open triangles indicate the wavelength obtained with $\Delta\mu$ from Berger's model. They give the closest wavelengths to the S-M curve of all four types of calculations.

3.5 Microwave Generation and Detection in Magnetic Multilayers

3.5.1 Introduction

The magnetic state of a magnet can affect the electron transport properties and give the well-known phenomenon of Giant Magnetoresistance (GMR). On the other hand, the electrical current can perturb the magnetic state of a magnetic multilayer via spin-transfer-torque; for example, the high enough current density can excite precession of magnetization in magnetic layers. The precession frequency depends on applied current and magnetic field. By varying applied current, the frequency can be tuned over a range of several GHz; by varying applied field, the frequency can also vary considerably and, depending on the multilayer system, may exceed 100 GHz at high field. In our experiments, high current densities were achieved by injecting current from a nanocontact into the multilayer. As mentioned in previous section, the region of the magnetic precession (excitation region) has dimensions comparable to the contact size. Such a nanoscale oscillator powered and tuned by spin-transfer-torque has some exciting properties for potential applications. It can be tuned in a wide range of frequencies, nanometer size easily integrated with other devices, and a narrow line-width in high-frequency output, that is, a high-frequency stability, as characterized by a quality factor *f/FWHM*, where *f* is the oscillator frequency and FWHM is the full-width at half-maximum of the spectral peak [21]. The quality factors exceeding 10000 have been previously reported [22]. The spin-transfer-torque oscillator can be used in portable electronics as timing reference, in heterodyne detector as a local oscillator, and in wireless communication system for fast electronic data transfer.

To study the high frequency precession dynamics, Tsoi et al. [13] have probed directly the behavior of current-induced spin-wave excitations by externally irradiating a point contact with microwaves. In this experiment, point-contact [10] with magnetic multilayer was placed inside a microwave cavity of an electron spin resonance (ESR) spectrometer [23]. The main experimental result is shown in Figure 3.10. High current density induces a high-frequency precession of magnetization in the magnetic multilayers at frequency ω_1. When the external radio-frequency (RF) radiation frequency ω_2 equals ω_1, the precession is amplified in a resonant manner. This process leads to an additional dc voltage across the contact that allows the frequency of precession to be mapped for different applied currents and fields (Figure 3.10b). The experiment also showed that the location of this additional radiation-induced structure varies with the frequency of the applied radiation. For

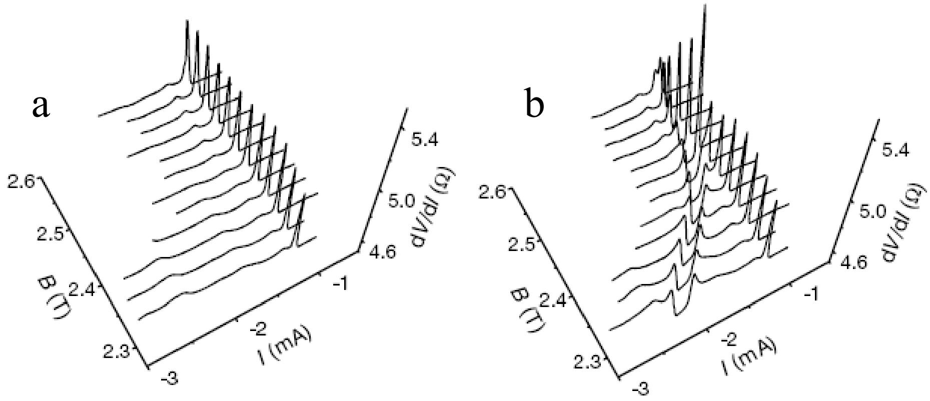

Figure 3.10 The point contact *dV/dI(I)* spectra for a series of magnetic fields. (a) Without external irradiation, the spectra reveal just the usual peak structure for a certain negative bias current I^*=-1.2mA which was attributed to the onset of the current-driven spin wave excitations. (b) Irradiation of the contact with microwaves at ω/2π=50.6GHz generates an additional structure in *dV/dI.* The strongest influence of the microwaves is found around a certain value B^*=2.6T of the applied field. Starting down from high fields, the additional structure is absent above B^*, appears around I^* when the field approaches B^*, and then moves to higher values of the bias current *I* as the field is reduced below B^* [13].

lower radiation frequency, the threshold field $B^*(\omega)$ is also lower which agree well with the linear relationship between the current driven spin wave frequency and applied field.

In the experiment described in this chapter, we designed a new experimental scheme where the high-frequency RF current from the microwave generator is directly injected into the magnetic multilayer through the same point contact where dc current drives high-frequency precession. Our goal is to explore the resonance between current-driven spin waves and external microwaves in this simpler setup, and recover information about frequency of the spin waves. Combination of this technique with in situ contact-size variation would leads to a powerful technique for studying current-induced excitations with both frequency and wave number sensitivity.

3.5.2 Experiment

The samples are sputtered $(Co/Cu)_N$ multilayers. The point contact system is standard (described in previous sections). The external microwave signal is injected into the sample using the set-up schematically shown in Figure 3.11. The high-frequency signal is transferred by a semi-rigid coaxial cable from microwave generator to the point contact. The positive center pin of the coaxial cable is connected directly to the sample. The negative shield of the coaxial cable is connected to the Cu tip through a ~50Ω resistance for impedance matching. In this system, the high-frequency RF signal from generator will flow directly across the point contact and thus through the excitation region underneath the contact. The microwave generator provides a maximum frequency of 67 GHz and the output power can be set up to +20 dBm which corresponds to 100 mW. Not that the actual power delivered to the contact can be significantly lower due to losses in cables, etc., on the way to the

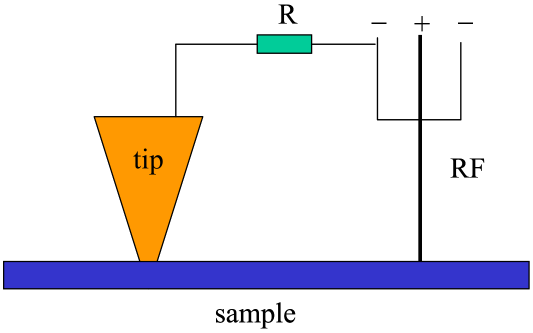

Figure 3.11 Schematic diagram of the high-frequency radiation system on the standard point contact.

contact.

We measured the *dV/dI(I)* spectra for a series of applied magnetic fields with the external microwaves tuned on. The microwave frequency and power were tuned to search for a resonance between the current-excited spin wave and external microwaves.

3.5.3 Results and Discussions

With dc current and field both applied perpendicular to the layers of our sample we excited spin-waves in the multilayer. Figure 3.12a shows the *dV/dI(I)* spectra for a series of magnetic fields from 1.8T to 2.2T without any microwaves applied to the contact (-20 dBm). At about 4mA, the excitations show up as peaks in point-contact *dV/dI* signal. Here double peak indicates that more than one layer may be excited in the multilayer. Figure 3.12b shows the *dV/dI(I)* spectra for the same point contact in the same field and current range but this time with microwaves turned on (+17 dBm). We found that the resonance occurs at frequency of ~ 39GHz. The *dV/dI(I)* spectra with and without external microwave are compared side by side in Figure 3.12. When the external microwave output power is about zero (-20dBm), the *dV/dI(I)* spectra show the usual peak structure for the current induced spin wave excitation. However when the external microwave output power is +17dBm, the extra structure appears in dV/dI spectra. Similar to what has been observed in Ref. [13], this additional structure appears around the critical current at field $B^{*}\approx 2.2$T and shifts to higher currents for higher applied fields. This additional structure can be explained as an extra dc voltage from the resonance between the excited spin waves and external microwaves.

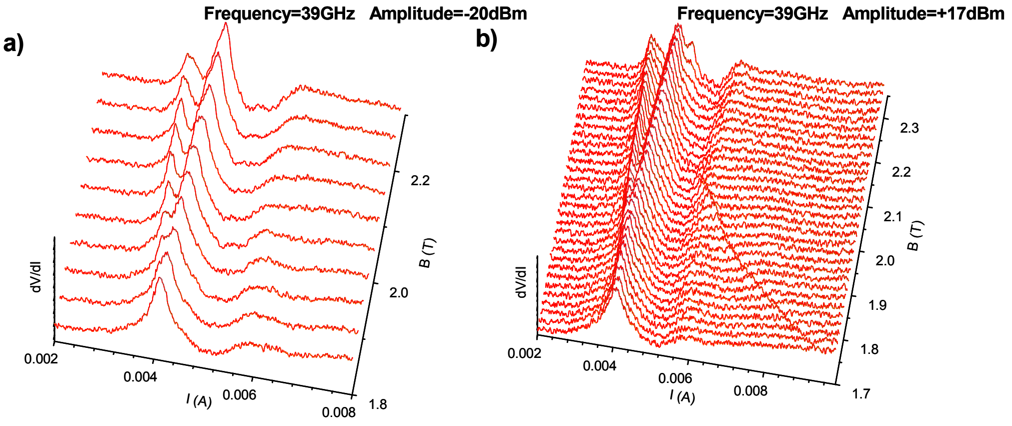

Figure 3.12 The point contact dV/dI(I) spectra for a series of magnetic fields. a) With external microwave have almost zero output power (-20dBm), the spectra show the usual peak structure at positive bias current I≈4mA where the current excited the spin wave. b) With the external microwave at frequency f=39GHz and output power A=+17dBm, the additional structures are generated in *dV/dI*.

In our experiment we didn't find any additional structure in dV/dI spectra when the microwave frequency was tuned away from 39 GHz. This may be related to strong frequency-dependent losses of microwave power in our system. In our system, the high-frequency cable is about 70 inches long from the generator to the sample. This means that more than 90% of the output power will be lost in signal transfer. Furthermore, as shown in Figure 3.11, at the very end of the cable, we expose the center pin from the cable shield protection. This certainly decreases the power of microwave signal injected into the sample. This hypothesis of strong power losses also correlates with an extremely weak microwave-induced signal observed at 39 GHz (see Figure 3.12b). Overall, further research with possibly better designed high-frequency microwave injecting system is required.

3.6 Summary

We use point contact technique to explore the spin-transfer-torque effect in Co/Cu magnetic multilayer films. With current and field both applied perpendicular to the film layers, we observe the current induced spin-wave excitations in magnetic layers at both high and low fields and magnetization switching at around zero fields at room temperature. Our novel technique to control the point-contact size extends significantly the capabilities of such contacts for studying the spin-transfer phenomena. Continuous in situ variation of the contact size and, therefore, of the spin transfer excitation volume enables detailed contact-size dependent measurements of current-driven excitations and provide valuable information on the critical current/voltage relation. Most importantly, this is the first technique with in situ sensitivity to the wavelengths of current induced spin waves. We are able to recover the wavelengths of spin waves from the $I_c(B)$ linear relation. The recovery of wavelength is implemented with theoretical formula of $I_c(B)$ from Slonczewski's spin torque model, and spin wave energy conservation model using van Son's energy difference $\Delta\mu$ from diffusion equation and Berger's $\Delta\mu$ from Fermi surface shift. All resulting wavelengths recovered via combining experimental data with these models are in good agreement with the prediction that wavelength of spin wave is comparable to the contact size. The high-frequency measurements show that in our newly designed system with microwave generator, external microwaves can interact resonantly with dc-driven spin waves. However dramatic loss of external microwave signal limits its application for studying high-frequency behaviors.

3.7 References

[1] M. N. Baibich, J. M. Broto, A. Fert, F. N. V. Dau, F. Petroff, P. Eitenne, G. Creuzet, A. Friederich, J. Chazelas, *Phys. Rev. Lett.* **61**, 2472 (1988)

[2] G. Binasch, P. Grunberg, F. Saurenbach, W. Zinn, *Phys. Rev. B* **39**, 4828 (1989)

[3] P. Grunberg, R. Schreiber, Y. Pang, M. B. Brodsky, and H. Soweis, *Phys. Rev. Lett.* **57**, 2442 (1986)

[4] S. S. P. Parkin, N. More, and K. P. Roche, *Phys. Rev. Lett.* **64**, 2304 (1990)

[5] S. S. P. Parkin, R. Bhadra, and K. P. Roche, *Rhys. Rev. Lett.* **66**, 2152 (1991)

[6] M. A. Ruderman, C. Kittel, *Phys. Rev.* **96**, 99 (1954)

[7] T. Kasuya, *Prog. Theor. Phys.* (Kyoto) **16**, 45 (1956)

[8] K. Yosida, *Phys. Rev.* **106**, 893 (1957)

[9] R. Coehoorn, *Phys. Rev. B* **44**, 9331 (1991)

[10] M. Tsoi, A. G. M. Jansen, J. Bass, W. –C. Chiang, M. Seck, V. Tsoi, and P. Wyder, *Phys. Rev. Lett.* **80**, 4281 (1998)

[11] J. C. Slonczewski, *J. Magn. Magn. Mater.* **195**, L261 (1999)

[12] A. Fert, and I. A. Campbell, *J. Phys. (Paris), Colloq.* **32**, C1-46 (1971)

[13] M. Tsoi, A. G. M. Jansen, J. Bass, W. C. Chiang. V. Tsoi, and P. Wyder, *Nature* (London) **406**, 46 (2000)

[14] S. L. Kiselev. J. C. Sankey, I. N. Krivorotov, N. C. Emley, R. J. Schoelkopf, and R. A. Buhrman, *Nature* (London) **425**, 380 (2003)

[15] W. H. Rippard, M. R. Pufall, S. Kaka, S. E. Russek, and T. J. Silva, *Phys. Rev.*

Lett. **92**, 027201 (2004)

[16] F. B. Mancoff, N. D. Rizzo, B. N. Engel, and S. Tehrani, *Appl. Phys. Lett.* **88**, 112507 (2006)

[17] Y. Acremann, J. P. Strachan, V. Chembrolu, S. D. Andrews, T. Tyliszczak, J. A. Katine, M. J. Carey, B. M. Clemens, H. C. Siegmann, and J. Stohr, *Phys. Rev. Lett.* **96**, 217202 (2006)

[18] J. Stöhr, H. C. Siegmann, *"Magnetism: from fundamentals to nanoscale dynamics"* (Springer Series in Solid-State Sciences, P506 Springer, 2006)

[19] P. C. van Son, H. van Kempen, and P. Wyder, *Phys. Rev. Lett.* **58**, 2271 (1987)

[20] L. Berger, *Phys. Rev. B* **54**, 9353 (1996)

Chapter 4
Spin-Transfer-Torque Effect in Antiferromagnets

In this chapter we discuss the spin-transfer-torque effect in the magnetic systems where conventional ferromagnets are replaced by antiferromagnets. We show that exchange bias at an antiferromagnet/ferromagnet interface can be varied by an applied current, which is the first experimental evidence for spin transfer torque in antiferromagnets. Later we extend the exploration of spin-transfer-torque (STT) in spin valves with different ferromagnetic/antiferromagnetic materials combination and discuss the comprehensive STT effects in both ferromagnets and antiferromagnets. Last we present our search for the antiferromagnetic giant magnetoresistance (AGMR) in antiferromagnetic sandwiches where two antiferromagnetic layers are separated by a non-magnetic spacer.

4.1 Introduction

The current induced spin transfer torques in ferromagnets have been predicted more than 10 years ago [1, 2] and have since been extensively studied both experimentally and theoretically [3]. Recently, MacDonald and co-workers [4-6] predicted that spin transfer torque could occur in systems where the ferromagnets are replaced by antiferromagnets. First, they predicted that the resistance of an antiferromagnetic (AFM) trilayer of the form AFM/N/AFM, where N is non-magnetic metal spacer, could change when the relative orientation of the magnetic moments in the two AFM layers next to the N spacer changes—antiferromagnetic GMR=AGMR, and that the resistance changes could be comparable in size to those for GMR. Second they predicted that injection of a large enough current density j, perpendicularly into an AFM/N/AFM trilayer (current-perpendicular-to-plane geometry = CPP), could change the magnetic order of the trilayer. Their estimate of the necessary $j \sim 10^5$ A/cm^2 was hundred times less than the typical $j \geq 10^7$ A/cm^2 needed to reverse the magnetic order in F/N/F multilayers. Part of the reason for this smaller j is their conclusion that the STT with AFMs acts on a large portion of the AFM-metal, whereas it acts on an F-metal only near the N/F interface. Lastly, they predicted that a large enough CPP j injected into an F/AFM interface could affect the exchange bias at the interface. Such a phenomenon could allow current to control the exchange bias in magnetic devices. Replacing F-metals in spintronic devices with AFM-metals would also eliminate unwanted effects of shape anisotropy on the magnetic stability of small elements, thus potentially offering better control of the magnetic state in nanoscale systems. Xu et al. [7] recently calculated the AGMR for a simple AFM/N/AFM/N = FeMn/Cu/FeMn/Cu multilayer, and found results similar to those predicted by MacDonald and co-workers, and Gomonay and Loktev [8] provided additional theoretical evidence that polarized current can destabilize the equilibrium state of an AFM. Currently all the published experimental searches of spin transfer torque in antiferromagnets [9-12] were done in exchange-biased spin valves (EBSVs). The spin valve structure was first introduced by Dieny in 1991 for studying GMR effect [13]. Unlike magnetic multilayer where interlayer exchange is used to obtain antiparallel configuration which is necessary for observing GMR effect, the spin valve shows GMR effect by constructing two ferromagnetic layers with different switching fields. The simplest spin valve is sandwich system containing two ferromagnetic (F) layers separated by a non-magnetic metal (N) layer. One antiferromagnetic layer lies outside the ferromagnetic trilayer and pins the adjacent F layer to give it a larger switching field compared to that of the other (free) F layer (see Figure 4.1). This exchange coupling between AFM and F layer is called *exchange bias*. This phenomenon was first discovered by Meiklejohn and Bean in 1956 in the study of oxidized antiferromagnet CoO particles [14]. The exchange bias phenomenon is due to the magnetic structure near the F/AFM interface. The basic understanding of exchange bias is shown in Figure 4.2 with the schematic diagram of exchange bias at the F/AFM interface and M-B loop for the F layer under the effect of exchange bias. The exchange bias is also called *unidirectional exchange anisotropy*. It presents a preferred direction of the F

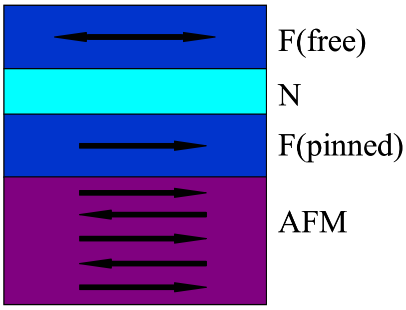

Figure 4.1 Schematic cross-section of a simple exchange-biased spin valve structure.

layer magnetization. Assuming initially F and AFM spins are aligned along the same axis, there are uncompensated spins in AFM

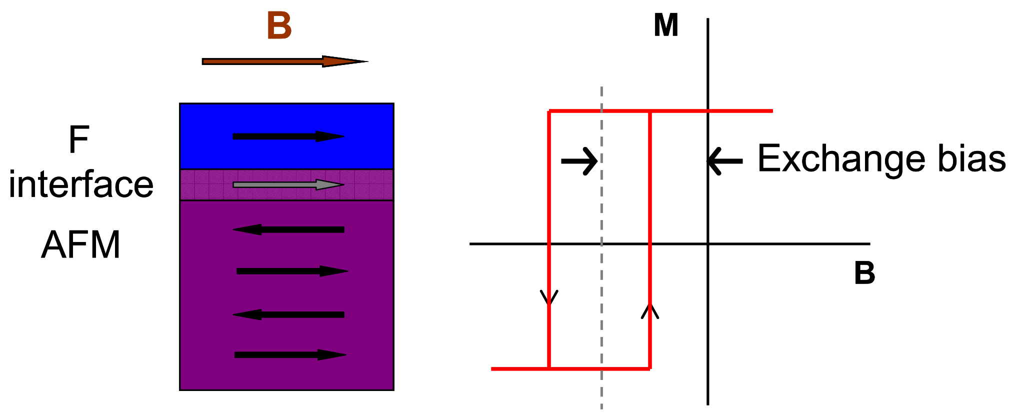

Figure 4.2 Schematic diagram of exchange bias at an interface between a ferromagnet (F) and an antiferromagnet (AFM). It originates from exchange coupling of the moments in the FM to uncompensated pinned moments in the AFM interface. As a result of this coupling the F layer magnetization M-B loop is shifted along the field axis. Here M is the F layer magnetization, B is the external magnetic field.

near the interface. Some of these uncompensated spins are pinned by the bulk AFM and cannot be reversed by typical external magnetic field. These pinned interfacial spins are coupled to the F layer magnetization and set an energy barrier for the F layer magnetization reversal. The exchange bias is shown as an exchange bias field in M-B measurement for the coupled F layer (Figure 4.2). Here the external field B is applied in the plane along F layer easy axis. If there is no exchange coupling from AFM, the F layer M-B loop should be symmetric about zero external magnetic field B because of uniaxial anisotropy. In the presence of exchange bias, this symmetric loop is horizontally shifted by an exchange bias field H_E. The exchange bias can be introduced by the following methods. One is growing the F layer on AFM in the presence of a constant setting field. The other is cooling the already formed F/AFM samples down through Néel temperature of AFM with static setting field. The exchange bias field H_E can be either same as or opposite to the setting field direction. In our research, the H_E is opposite to the setting field and called negative exchange bias.

The exchange biased spin valve (EBSV) shows GMR effect based on the resistance change from variable alignments between free layer and pinned layer. The angular variation of the resistance due to the GMR effect is to a good approximation given by [16]:

$$R(\theta) = R(\theta = 0) + \frac{\Delta R_{GMR}}{2}(1 - \cos\theta) \qquad (4.1)$$

where θ is the angle between the magnetizations of free and pinned layers, and ΔR_{GMR} is the intrinsic GMR ratio defined as resistance difference between parallel and antiparallel alignment of free and pinned layers.

The magnetoresistance curves for three different classes of EBSVs are shown in Figure 4.3. We define the exchange bias field as $H_E = -(H^L + H^R)/2$ and the coercive field as $H_C = -(H^L - H^R)/2$, where H^L is the leftmost field at which the pinned layer flips, and H^R is the rightmost field. With the standard definitions of field directions, H^L is more negative than H^R, so both H_E and H_C are positive. Here we take the non-magnetic spacer to be thick enough so that there is no magnetic coupling between free layer and pinned layer and the free layer reverses symmetrically about zero external field H=0. We start with large +H along the pinning direction, causing

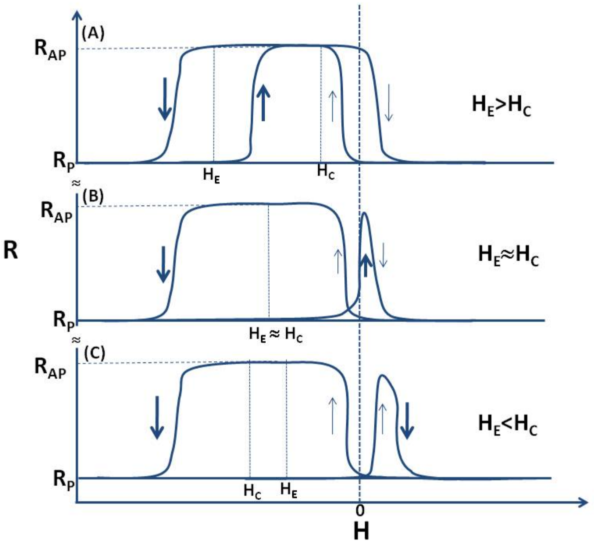

Figure 4.3 Schematic hysteresis curves for exchange-biased spin-valves with: (A) $H_E > H_C$; (B) $H_E \approx H_C$, and (C) $H_E < H_C$. Thick arrows indicate when the pinned layer reverses; thin arrows indicate when the free layer reverses. The arrows point in the direction of resistance change. The free layer reverses symmetrically about H = 0 [15].

the moments of both the free and pinned layers to point along +H (parallel = P) orientation. From standard GMR theory with identical F-metals, R_P is the minimum resistance. Reducing the magnitude of H, the free layer reverses at a small negative H, giving maximum resistance, R_{AP}. A larger negative H^L is needed to break the EB pinning of the pinned layer, at which its moment rotates to along –H, returning the sample to R_P. After R_P is achieved, the direction of change of H is reversed and the field is swept back toward +H. In case A, $H_E > H_C$, the pinned layer switches back to its preferred pinned direction (at H^R) before reaching H = 0, giving R_{AP}. The sample returns to R_P after passing through H = 0, when the free layer reverses. In case B, $H_E \approx H_C$, the reversal of the pinned layer doesn't occur until $H^R \approx 0$, and R may never reach R_{AP} before falling back to R_P when the free layer flips. In case C, $|H_E| < |H_C|$, the pinned layer doesn't unpin until H^R is beyond where the free layer flips.

EBSV with case A is studied in Ref. [9] where the high density dc CPP current was injected into EBSV through a point contact. The main result was that the current can increase or decrease the exchange bias depending on the current polarity. This finding provided ane indirect evidence that current induces torques on AFM. Reference [10] studied the effect of a dc CPP current at 4.2K on sputtered and ion milled nanopillar EBSVs with case C. They applied positive or negative pulse current I_0 at fields H_0=±3KOe and found the effect of I_0 upon exchange bias field H_E was asymmetric in H_0. This observed asymmetry was attributed to the STT acting on the interfacial AFM moments, to asymmetrically enhance or suppress H_E. The EBSV structure with layer switching fields similar to case B was used in Ref. [11]. They sent a dc current-in-plane (CIP) current into EBSV film with a metallic AFM and could completely reverse the exchange bias with a large enough current. This effect could be explained by combining the effects from STT on AFM, Joule heating, and a large current-induced Oersted field.

4.2 Changing Exchange Bias in Spin Valves with Electrical Current

We show that a high-density electric current, injected from a point contact into an exchange-biased spin valve, systematically changes the exchange bias. The bias can either increase or decrease depending upon the current direction. This observation is not readily explained by the well-known spin-transfer torque effect in ferromagnetic metal circuits, and could be an evidence for the recently predicted current-induced torques in antiferromagnetic metals.

4.2.1 Introduction

An electrical current can transfer spin angular momentum to a ferromagnet. This novel physical phenomenon, called spin-transfer or spin-torque, offers unprecedented spatial and temporal control over the magnetic state of a ferromagnet and has tremendous potential in a broad range of technologies, including magnetic memory and recording. It was recently predicted [4] that current induced torques are a general property of magnetic metals not limited to ferromagnets (F) and in particular that spin-torques act on the order parameter of antiferromagnetic (AF) circuit elements. Unlike spin-torques in a F-metal, which follow from conservation of total spin and act only near interfaces, current-induced torques in AF-metals are not related to total spin conservation and have a bulk contribution. In an antiferromagnet the magnetic order is staggered, which requires the staggered torques to drive the order parameter dynamics. As calculated in Ref. [4] for the structure of AFM/N/AFM, where two antiferromagnets are noncollinear, the out-of-plane spin density is produced in top AFM and drives staggered torque into bottom AFM to excite spatially coherent precession of the antiferromagnetic order parameter. Because the perpendicular spin density is periodic with the antiferromagnet lattice, it will not decay away from the interface and therefore lead to spin transfer torques that act all the way through the whole body of antiferromagnet. The simulated spin density (spin transfer torque) in a standard spin valve structure (AFM/F2/N/F1) is shown in

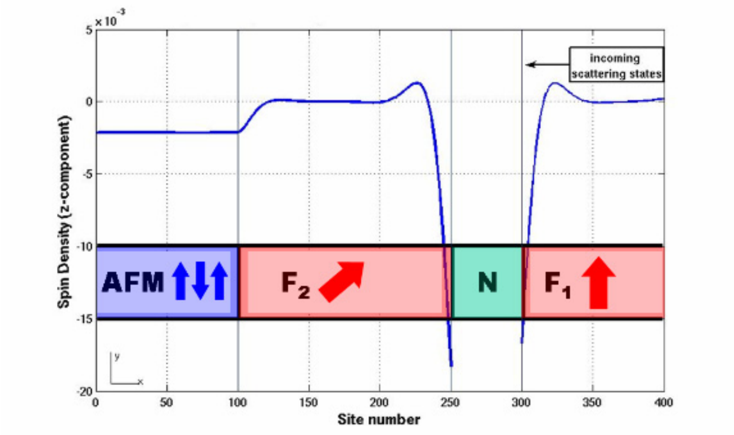

Figure 4.4 Variation of out-of-plane spin density cross the standard EBSV structure. The spin transfer is localized at F interfaces and is constant throughout the entire AFM volume [17].

Figure 4.4. As expected, the spin transfer in Fs is big but limited to the F/N interfacial regions, while the spin transfer in AFM is constant throughout the entire volume of AFM. The calculated total torque on F1, F2, and AFM is -0.087, -0.1277, and -0.2135, respectively (in arbitrary units). We can see that the torque on AFM can be bigger than that acting on Fs. Together with the absence of shape anisotropy in AFM, the predicted critical current for driving AFM order parameter dynamics is about 10^5 A/cm^2 [5], which is significantly smaller than the typical threshold current (10^7 A/cm^2) for a ferromagnet.

From experimental point of view, all the theoretical calculations are for perfect AFM layers and ballistic transport. The spin transfer torque in AFM is consequence of quantum interface. However the disorder of layers might produce diffusive scattering and weaken such STT in AFM. Hence it's not optimistic to observe STT in pure AFM spin valve structures. Instead, the exchange biased spin valve containing coupled AFM/F layers is good for exploring antiferromagnetic STT because the spin polarization in F layer is high and the possible current induced antiferromagnetic moments' rearrangements could be presented as the change of exchange bias. This is the motivation for us to search for the antiferromagnetic STT in EBSVs.

4.2.2 Experiment

We use a standard mechanical point contact system as described in Chapter 2.2 to generate high-density currents. Our samples are EBSVs prepared by sputtering. The EBSV contains two ferromagnetic layers separated by a non-magnetic spacer. One of the ferromagnetic layers is pinned by an antiferromagnetic layer. The material for ferromagnetic layer is $Co_{91}Fe_9$, for antiferromagnetic layer is $Fe_{50}Mn_{50}$, for non-magnetic spacer is Cu. On top of the EBSV there is a 5nm thick Au protective cap to avoid oxidation. Underneath the EBSV there is a 50nm thick Cu underlayer which works as a sink to secure a closely perpendicular-to-plane flow of the current (CPP) from the point contact, across the EBSV, and into the Cu buffer. Three standard EBSVs: (I) FeMn(8 nm)/CoFe(3 nm)/Cu(10 nm)/CoFe(10 nm), (II) FeMn(3 nm)/CoFe(3 nm)/Cu(10 nm)/CoFe(10 nm), (III) FeMn(8 nm)/CoFe(3 nm)/Cu(10 nm)/CoFe(3 nm) and two inverted EBSV structures: (IV) CoFe(10 nm)/Cu(10 nm)/CoFe(3 nm)/FeMn(8 nm), (V) CoFe(3 nm)/Cu(10 nm)/CoFe(3 nm)/ FeMn(8 nm) were studied. EBSVs (I), (II), and (IV) are asymmetric, and EBSVs (III) and (V) are symmetric. The samples were cooled through the Néel temperature of FeMn ($T_N \approx$ 400 K) in the presence of a static magnetic field (~18mT) and zero applied current to pin the magnetization direction of the neighboring CoFe. A total of 24 point contacts with resistances from 0.7-5 Ω showed the characteristic behaviors that we describe with the help of representative data from a 0.92 Ω contact to sample (I), a 2.72 Ω contact to sample (III), and a 1.59 Ω contact to sample (IV). At room temperature and with in-plane magnetic field B applied along the exchange bias direction, we measured the magnetoresistance (MR) of the point contacts at different bias current. Also with the capability of in situ contact size dependent measurement, we measured the magnetoresistances with point contact resistance reduced from 4.1Ω to 1.9Ω for sample (I).

4.2.3 Results and Discussions

The magnetoresistance for standard EBSV (I) is shown in Figure 4.5. This measurement was done at low bias current to show how the point-contact resistance changes as a function of magnetic field in the absence of any spin-transfer effects. At high positive field, the field direction is along the exchange bias and the field magnitude is high enough to saturate the free and pinned F layers in the same

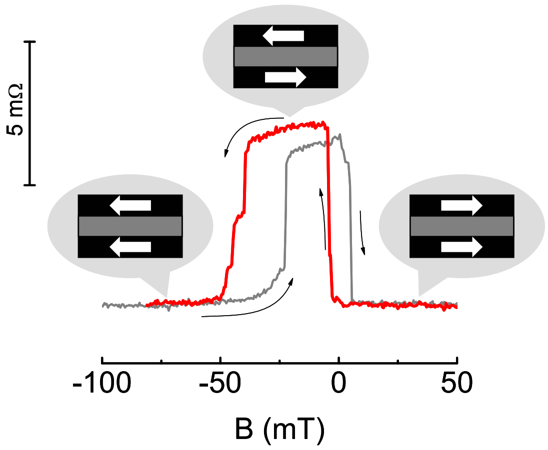

Figure 4.5 Magnetoresistance curve for standard sample (I). Red curve is for magnetic field sweeping from high to low; gray curve is for opposite way. Arrows indicate the directions of point contact resistance change. Inserts show the alignment of two F layer magnetizations in EBSV.

direction. Hence the resistance is at lowest value due to GMR effect. At low negative field, the field direction is opposite to the exchange bias but the field magnitude is not high enough to overcome the exchange coupling plus F layer anisotropy. As a result only free layer is reversed by magnetic field. This give antiparallel alignment for two F layers and resistance is at highest resistance state. At high negative field, the field is strong enough to align both F layers opposite to exchange bias and gives the lowest resistance again. The reversed sweeps from high negative to high positive fields show similar behavior. The reversal of both free and pinned CoFe layers and the corresponding variations in R proceed via a discrete series of irreversible steps. The latter correspond to reversals of individual ferromagnetic domains in CoFe probed by the point contact. Note that domains closest to the contact contribute most to its resistance. As expected, the switching fields for free layer are symmetric about zero fields, while the switching fields for pinned layer are symmetric about 30mT due to exchange bias.

Figure 4.6 shows typical variations in the contact resistance *R=V/I* as a function of the applied field B (solid traces) for a series of bias currents I. Black (grey) traces show sweeps from high positive (negative) field to high negative (positive) fields. Here negative current corresponds to the flow of electrons from the tip into the spin valve. The reversal of the free layer seems to be little affected by the applied current. In contrast, the current clearly changes the exchange bias field at which the pinned layer is reversed. The changes in the exchange bias are reversible when current is stepped up or down and exhibit no significant 'training' effects.

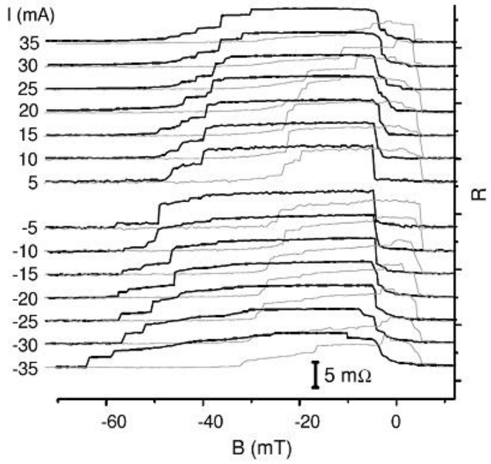

Figure 4.6 Point-contact magnetoresistance at different bias currents. Solid traces show point-contact resistance *R=V/I* as a function of the applied magnetic field *B* for a series of bias currents *I*. The current was varied from 35 mA to -35 mA as indicated on the left. The reversed current sequence showed similar behavior. Black (grey) traces are for *B*-sweeps down (up). The MR sweeps at different currents are shifted along vertical axis for clarity. Note that the resistance changes associated with reversal of the pinned layer usually extend over a wider range of *B* (broader transition) than those for the free layer, especially for larger (magnitude) *I*. The point-contact resistance at high fields is 0.92Ω [9].

The 2D gray-scale plot representation [see Figure 4.7a; lighter color indicates higher resistance] of the data in Figure 4.6 suggests that on average the exchange bias

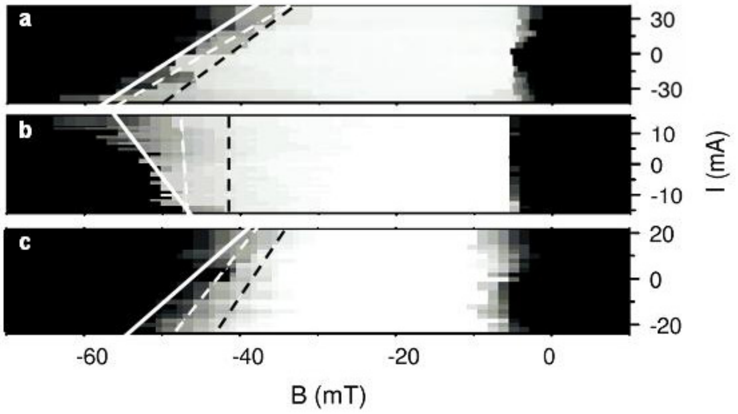

Figure 4.7 Variation of exchange bias in standard, inverted, and symmetric spin-valve structures. 2D gray-scale plots show the point contact magnetoresistance (down sweeps) as a function of the bias current in (a) standard, (b) inverted, and (c) symmetric spin-valve structures. Lighter color indicates higher resistance with black/white corresponding to (a) 0.919Ω/0.926Ω, (b) 1.590Ω/1.596Ω, (c) 2.720 Ω/2.733Ω. In (b) and (c) the current was stepped up from high negative values while in (a) it was stepped down from high positive ones. See text for details [9].

increases with (current goes from positive to negative) applied negative current and decreases with positive one. The white solid, white dashed, and black dashed lines in Figure 4.7 are the least-squares linear fits to the *R(B)* data points at the 30%, 50%, and 70% levels, respectively, assuming 0% for the minimum resistance value (parallel state) and 100% for the maximum resistance value (antiparallel state). The resulting slope of 3.9 ± 0.3 A/T in Figure 4.7a emphasizes the overall trend, and also highlights stochastic variations that occur on top of this trend. Although the resistance curve near switching varies from run-to-run at a given current, the trend indicated by the white fits is always present. For comparison, Figures 4.7b and 4.7c show exchange bias variations in an inverted structure CoFe (10nm)/ Cu (10nm)/CoFe (3nm)/FeMn (8nm) in which the pinning antiferromagnet lies on top of the spin-valve stack and in a symmetric structure FeMn (8nm)/CoFe (3nm)/Cu (10nm)/ CoFe (3nm) in which the pinned and free ferromagnets have the same thickness. While the symmetric spin valve exhibit qualitatively similar variations in the exchange bias as a function of the applied current, the response of the inverted spin valve (Figure 4.7b) is different. Here positive current crosses the FeMn/CoFe interface in the opposite sense (from FeMn into CoFe) compared to the case of Figure 4.7a. Interestingly, the effect of current on the exchange bias is also reversed (slope = −3.3 ± 0.4 A/T in Figure 4.7b) – the positive current increases the exchange bias while negative current decreases it. Note that the observed asymmetry of the current-induced variations in exchange bias can not be explained by heating effects, which are symmetric in current.

The conventional spin transfer torque explanation of our data can be attempted by viewing the system as being composed of three ferromagnets: the free ferromagnet, the pinned ferromagnet, and the surface layer of the antiferromagnet which includes uncompensated pinned moments [18, 19]. In this picture, spin torques act on the pinned F layer due to transport electron transmission through or reflection off both the free F layer and the AFM layer. The spin torque acting on the pinned F layer due to the free one, is necessarily accompanied by a “reaction” torque acting on the free F layer due to the pinned one [2]. Indeed, these torques are expected to have the same magnitude when the free and pinned F layers have the same thickness. However, as illustrated by the sample (III) data in Figure 4.7c, the behavior observed in symmetric structures is similar to that of asymmetric ones; the switching field of the free F layer is essentially unaffected by current in all EBSV structures over the current range studied here. We argue below that the qualitative difference in the influence of current on the two CoFe layers is due to a large difference in the current induced torques they experience, a difference that is not allowed by the spin transfer torque applied solely to the F layers. Some simple mechanisms that could produce a difference can be discounted on experimental grounds. In particular, the difference in damping, which competes with torques in current induced switching phenomena, would produce an effect opposite to the one we observe because the pinned layer is more strongly damped [20] than the free one. Spin transfer torques between the pinned layer and uncompensated pinned spins in the antiferromagnet cannot by significant because of the orders of magnitude difference in total spin between these ferromagnetic subsystems. Finally if we focus on the usual spin transfer effect on the pinned F layer due to the free F, the current-induced change in its switching field is expected to be opposite to what we observed as illustrated in Figure 4.8. Here we consider the simple structure with only pinned layer F1, free layer F2 and Cu spacer. For our negative current, the electrons flow from free layer F2 to pinned layer F1 (Figure 4.8a). The electrons are polarized in F2, which means the transmitted electrons have majority spin direction along F2 moment direction. When these polarized electrons get to F1, they exert a torque on F1 layer moments. This torque (shown as orange arrow on F1 moment in Figure 4.8a) tends to rotate F1 toward the F2 direction. Also some of electrons are reflected back from F1 with opposite to F1 moments. These reflected electrons go back to F2 and apply torque on F2 such so to

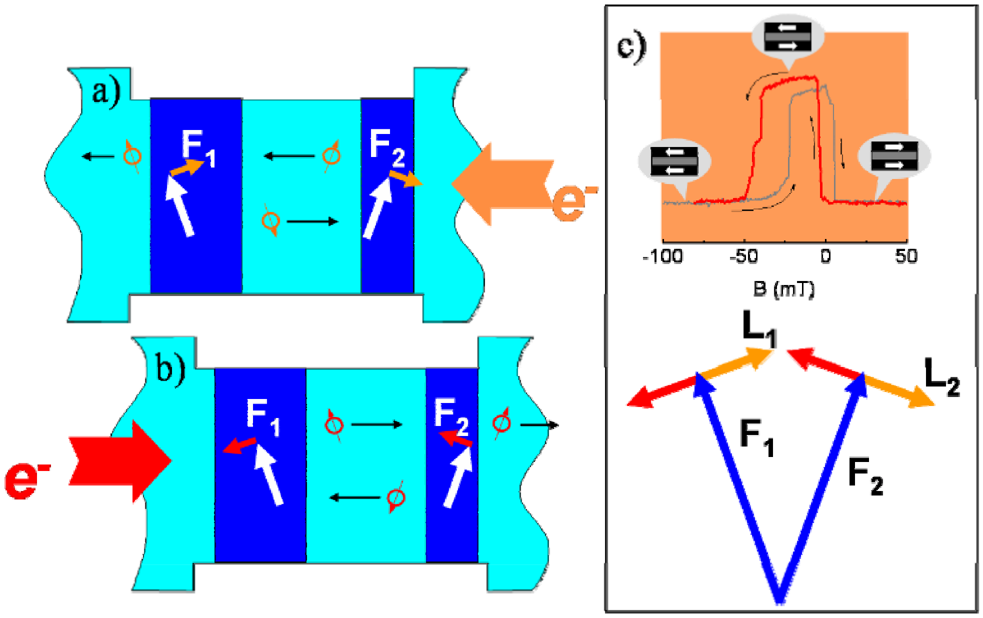

Figure 4.8 Schematic diagram of usual spin transfer torque on the F layers in simple F1/N/F2 structure. Assume F1 is the pinned layer in EBSV and F2 is the free layer. a) Negative current induced STT. b) Positive current induced STT. c) Direction of torques from positive (red) and negative (orange) current on F1, F2 layers.

Rotate it away from F1 direction. Figure 4.8b show the similar process for our positive current where the electrons flow from pinned layer F1 to free layer F2. Similarly the reflected electrons apply torque on F1 to favor the antiparallel alignment with F2. The summarized usual spin transfer torques on F1 and F2 are shown in Figure 4.8c. We are more interested in pinned layer F1 and use the field sweeping down curve (red curve in MR measurement) to illustrate the STT effect on switching field. Here a positive current (red) generates torque on F1 to favor the antiparallel configuration. Since the two F layers alignment changes from antiparallel to parallel at switching field, the STT actually prevents this from happening and results in a larger field required for switching. For negative current (orange), the STT on pinned layer F1 favors parallel state. It helps the switching of F1 and lowers the switching field. Thus, the usual 'ferromagnetic' spin transfer torque on pinned layer gives the opposite effect to the observed effect where positive current decreases the pinned layer switching field and negative current increases it. The above arguments rule out the conventional spin transfer effect between the two CoFe layers as the explanation of our observations.

A natural explanation of our data is provided by the ideas put forward in Ref. [4] in which current-induced torques are calculated microscopically by evaluating spin densities in the non-equilibrium current-carrying state. In this time-dependent mean-field (e.g. time-dependent spin-density-functional) based picture, spin-torques are due to the contribution of transport electrons near the Fermi energy to the spin-dependent exchange-correlation potential, which is [4] in turn proportional to the corresponding spin-density contribution. Current-induced changes in the exchange-correlation effective magnetic field are experienced by all magnetic atoms and are generically non-zero in any circuit with non-collinear moments whether arranged ferromagnetically, antiferromagnetically, or in some more complex spatial arrangement. Conservation of total spin, which is relevant for order parameter dynamics in a ferromagnet but not in an antiferromagnet, is not a necessary condition for current-induced spin-torques. It does however simplify its description in a system composed of coherent ferromagnetic elements to the commonly used action-reaction picture, with separate current-carrying quasiparticle and collective magnetization degrees-of-freedom.

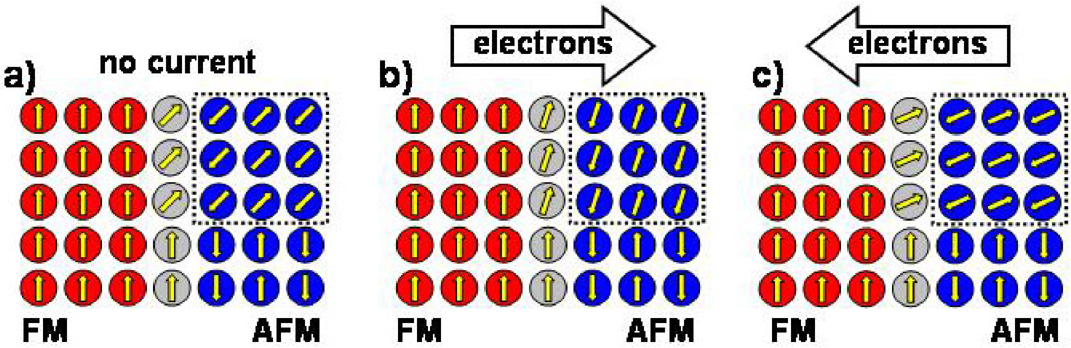

Figure 4.9 Schematic illustration of the influence of transport currents on exchange bias. (a) The surface layer of an antiferromagnet contains uncompensated magnetic moments (grey). A fraction of the uncompensated moments are pinned. They do not reverse when the adjacent ferromagnet reverses and are responsible for the existence of exchange bias. Dotted line indicates an antiferromagnetic domain. (b-c) Exchange bias will increase (decrease) if the configuration of pinned moments is altered to increase (decrease) the total component along the exchange bias direction. The pinned moments are exchange coupled to the bulk antiferromagnet and will be reoriented by torques that act in the bulk of the antiferromagnet [9].

From Ref. [4] it follows on quite general grounds that the moment arrangement near the ferromagnet, antiferromagnet interface is altered by a transport current. Since the moment arrangement near this interface is complex and still not fully characterized even in the absence of a current, we are able at present to provide only the qualitative explanation for the dependence of exchange bias on transport current summarized schematically in Figure 4.9. Near the exchange bias field, the meta-stability of the ferromagnet's opposite to field orientation is due almost entirely to exchange interactions with uncompensated moments in the surface layer of the antiferromagnet. Some of these spins are pinned, thereby inducing an energy barrier for ferromagnetic layer spin reversal [18, 19]. Electrons flowing from the ferromagnet into the antiferromagnet [4] induce torques on moments in the antiferromagnetic matrix, which alter its magnetic configuration. These torques tend to favor parallel alignment of moments at the ferromagnet/antiferromagnet interface [4] and will therefore tend to increase the exchange bias field. Electrons flowing in the opposite direction will tend to have the opposite effect.

Our simple picture does not attempt to account in detail for the domain structure and disorder in both materials near the FeMn/CoFe interface that is presumably responsible for stochastic run-to-run variations, but we believe that it gives the correct qualitative explanation for the overarching trend identified in our data. The experiment admittedly does not directly imply that the effect we have discovered is due to torques acting on the bulk FeMn antiferromagnet because it does not distinguish torques applied directly to the uncompensated pinned moments from torques applied to buried moments which are exchange coupled to the surface. It nevertheless conclusively demonstrates that the scope of fundamentally interesting and potentially useful current-induced torque phenomena in non-collinear magnetic systems is even broader than the rich variety of ferromagnetic nanomagnet effects explored to date.

Because there is no spacer separating the ferromagnetic and antiferromagnetic layers in the current experiment, strong interactions across the interface imply that changes in the magnetic microstructure of the antiferromagnet will not normally be permanent, but will relax once the current is turned off. Our results suggest though, that it is possible in principle to drive irreversible changes in the antiferromagnet's microstructure with a transport current, and thereby achieve post-growth changes in exchange-bias characteristics. The latter supports the feasibility of a programmable magnetic memory element.

Additional size dependent measurements for standard EBSV (I) is performed with the point contact resistance reduced from 4.1Ω to 1.9Ω. At each resistance, the contact MR curves are measured at different bias currents and plotted in 2D gray-scale similar with Figure 4.7a. The least-squares linear fits to the *R(B)* data points at 50% levels give the slopes for each resistance as shown in Figure 4.10. With

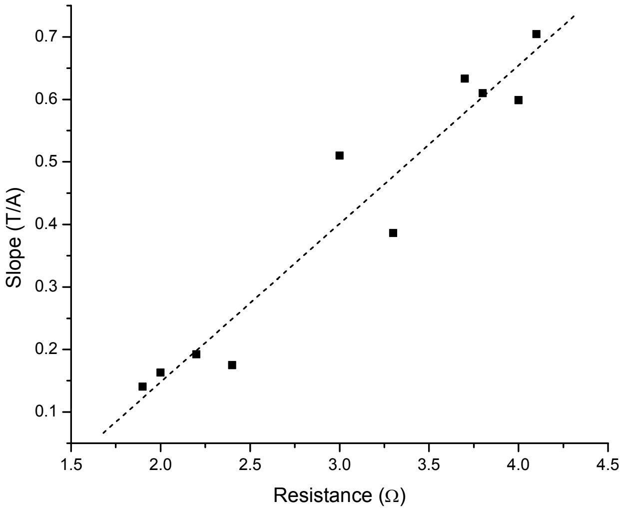

Figure 4.10 Slope of least-squares linear fits to the R(B) data points at 50% levels versus point contact resistance. Dashed line is guide for the eyes.

the guide from dashed line, we see the slope increase with the contact resistance. This can be understood as that at higher resistance with smaller contact size, the current density is higher and more efficient to tune the exchange bias. However the absence of a simple conservation law constraint makes it difficult for us to have quantitative understanding of this contact-size dependent current effect on exchange bias.

4.2.4 Summary

Our study in the CPP geometry on EBSVs provided the first evidence that current could affect AFM magnetic order near the F/AFM interface, including the exchange bias field H_E. We found that one polarity of I increased H_E, while the other polarity decreased it. To understand our observation, we proposed a model based upon static STT effects of the current on the bulk of the AFM. Currently all the theoretical calculations are for perfect, single crystal samples, with the predictions requiring ballistic transport and quantum interference. In contrast, our real sputtered samples are ‘dirty’ and transport is at least substantially diffusive. Thus our understanding of effects of large current upon exchange bias is still qualitatively and the studies of STT in antiferromagnets are very incomplete.

4.3 Spin Transfer Interactions in Exchange Biased Spin Valves

4.3.1 Introduction

In previous section, we showed that the strength of the exchange bias at an AMF/F = FeMn/CoFe interface (FeMn = $Fe_{1-x}Mn_x$ with x ~ 0.5 and CoFe = $Co_{1-x}Fe_x$

with x ~ 0.09) could be increased or decreased (up to 30%) by an electric current flowing approximately perpendicular to the interface. As exchange bias is known to be associated with interfacial AFM magnetic moments [18, 19], our observation can be taken as the first evidence of effects of the current on the AFM predicted in Ref. [4]. However, the data do not distinguish effects of the current on bulk or interfacial AFM moments. In hopes of clarifying the situation, we have extended that study to a new AFM = IrMn = Ir_xMn_{1-x} with x = 0.2 and to a new F = Permalloy (Py = $Ni_{1-x}Fe_x$ with x ~ 0.2). This section, describing some of these new results, is organized as follows: We first show the results with new exchange biased spin-valves (EBSVs) of the form AFM/F(pinned)/Cu/F(free) with AFM=IrMn and the F=CoFe. The data for FeMn and IrMn are generally similar, with the current having clear and similar effects upon the exchange bias, but little or no effect on the coercive field of the ‘free’ CoFe-layer. Then we extend our study to F = Py with AFMs = FeMn or IrMn. With Py, the current usually affects both the exchange bias and the coercive field of the ‘free’ layer, but the variations are not always simple and we have not yet been able to correlate them in a simple way with layer thicknesses.

4.3.2 Experiment

The experiment is the same as we used in section 4.2.2. The exchange bias for AFM=IrMn is introduced by heating the sample to ~527K and then cool down through the Néel temperature in a constant magnetic field at 18mT. We tested the EBSVs for all material combinations of AFMs (IrMn and FeMn) and Fs (CoFe and Py), and also for two F layers thicknesses combination of 10nm and 3nm. The current density *j* is defined by the contact size and the magnitude of current; a typical contact resistance of 1~2Ω and I=10mA corresponds to ~10^{12}A/m^2.

4.3.3 Results and Discussions

EBSVs with IrMn/CoFe/Cu/CoFe

For its good combination of magnetic, thermal and corrosion properties, IrMn is widely used as an AFM in magnetic recording. We measure the EBSVs with standard structure IrMn/CoFe/Cu/CoFe and inverted structure CoFe/Cu/CoFe/IrMn. The IrMn layer thickness is 8nm, Cu layer thickness is 10nm. For the F layers we tested the thickness combinations of 3nm/10nm and 10nm/10nm (pinned/free). In these samples, the GMR ratio was about 0.5%. Figure 4.11 shows the magnetoresistance curves at bias current equal 1mA for IrMn/CoFe/Cu/CoFe with pinned layer thicknesses equal 3nm and 10nm. For pinned layer 3nm, the exchange bias is about 30mT, while for pinned layer 10nm the exchange bias is only 10mT. We focus on EBSV with 3nm pinned layer: IrMn(8)/CoFe(3)/Cu(10)/CoFe(10) for its stronger exchange bias and the same layer thicknesses with standard sample (I): FeMn(8)/CoFe(3)/Cu(10)/CoFe(10) in previous section (Figure 4.6, 4.7) for comparison (all thicknesses are in nm).

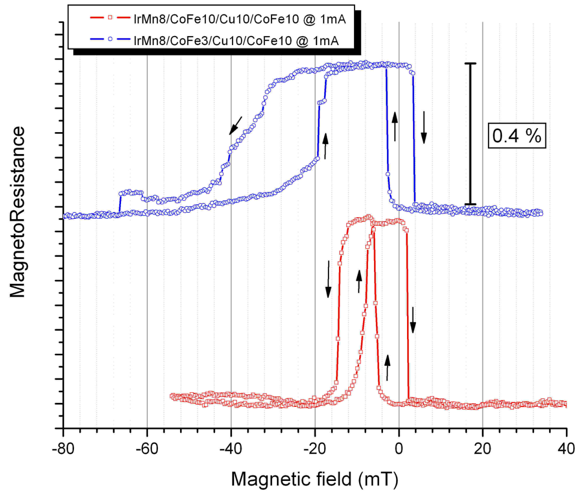

Figure 4.11 Comparison of low current magnetoresistance curves for samples structured as IrMn8/CoFe3/Cu10/CoFe10 (blue square) and IrMn8/CoFe10/Cu10/CoFe10 (red circle). (The two curves have been shifted for clarification)

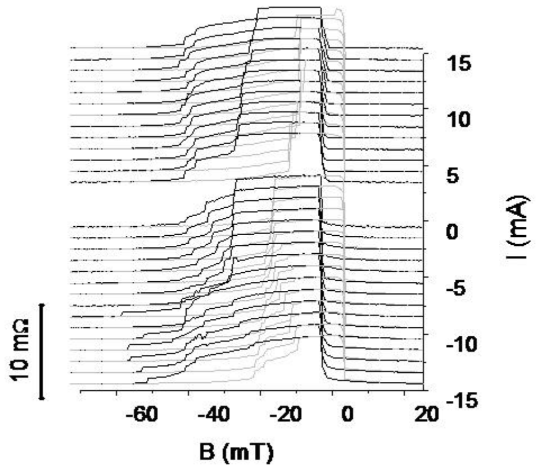

Figure 4.12 3D representation of R(B) hysteresis curves vs magnetic field B, for various currents I, for a 2.3 Ω point contact to an IrMn(8)/CoFe(3)/Cu(10)/CoFe(10) EBSV. The vertical scale size of 10 mΩ is indicated. The solid curves are 'down' sweeps (large +B to large –B). The grey curves are 'up' sweeps (large –B to large +B). Current I was stepped down from +15 to –15 mA with 1 mA steps [21].

Figure 4.12 shows R(B) hysteresis traces for different applied currents for a

2.3Ω contact to this EBSV. Figure 4.13a shows the down-field R(B) sweeps shown in Figure 4.12 in 2D gray-scale. As with FeMn, the reversal of the free CoFe(10) layer is unaffected by the applied current. Also as with FeMn, the reversal of the pinned layer shifts on average towards lower/higher magnitude fields for higher positive/negative applied currents. Figure 4.13b shows similar results for a 2.4Ω contact to an inverted EBSV structure: CoFe3/Cu10/CoFe10/ IrMn8. Again the applied current affects only the pinned layer. As with FeMn (Figure 4.7b), the directions of shifts of the pinned layer reversals in Figure 4.13b are opposite to those in Figure 4.13a. We conclude that

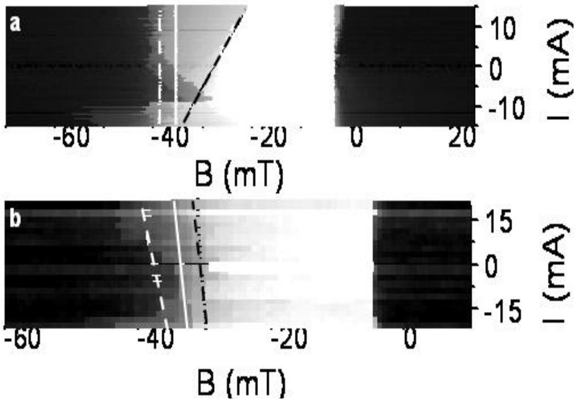

Figure 4.13 2D grey scale plots of 'down'-sweep R(B) data. White = maximum R (AP state) and black = minimum R (P state). Dashed white (30%), solid white (50%) and dashed black (70%) lines represent linear fits to the data at the indicated percentage of full scale [100% = R(AP) – R(P)]. (a) 2D grey scale plot of the 'down'-sweep R(B) data of Fig. 2a, for a 2.3 Ω point contact to a FeMn(8)/CoFe(3)/Cu(10)/ CoFe(10) EBSV. (b) 2D grey scale plot of the 'down'-sweep R(B) data for a 2.4 Ω point contact to an inverted EBSV--CoFe(10)/Cu(10)/CoFe(3)/ IrMn(8) [21].

the data for AFM = IrMn are generally similar to those for AFM = FeMn, with the current having similar effects upon the exchange bias, but little or no effect upon the coercive field of the 'free' CoFe-layer. The least-squares linear fits to the R(B) data points at the 30%, 50%, and 70% levels, respectively, give 0.01/-0.38 (30%), 0.01/-0.23 (50%), and 0.41/-0.18 (70%) T/A slopes for the exchange bias vs current dependencies in Figures 4.13a/b.

Since all of the IrMn/CoFe/Cu/CoFe data look rather similar to all of the FeMn/CoFe/Cu/CoFe data, and both sets are insensitive to whether the ‘free’ CoFe layer is 3 nm or 10 nm thick, we can explain the behaviors of the IrMn data using the same qualitative model as in Ref. [9]. It was assumed in Ref. [9] that the spin-transfer-torque (STT) on the ‘free’ CoFe was not large enough to perturb its reversals, and it was argued that the shifts in exchange bias at the FeMn/CoFe interface could be understood as effects of STT acting on the bulk of the FeMn [4], with information then transferred to the interface. Since we only detect variations in exchange bias associated with magnetic order at the interface, we have no direct information about the bulk AFM order, which is likely to be complex in both FeMn [22] and IrMn [23]. We thus conclude that STT affects magnetic order at IrMn/CoFe interfaces in a similar way to FeMn/CoFe.

EBSVs with FeMn/Py/Cu/Py and IrMn/Py/Cu/Py

So far we have described the R(B) response to high current densities in AFM/F/N/F EBSVs with two different AFM materials (FeMn and IrMn) but always the same F = CoFe. In this section we describe some of what we found in EBSVs with F = Py.

With Py, we usually find the current to affect both the exchange-bias field of the ‘pinned’ F layer and the coercive field of the ‘free’ F layer. However, the behaviors

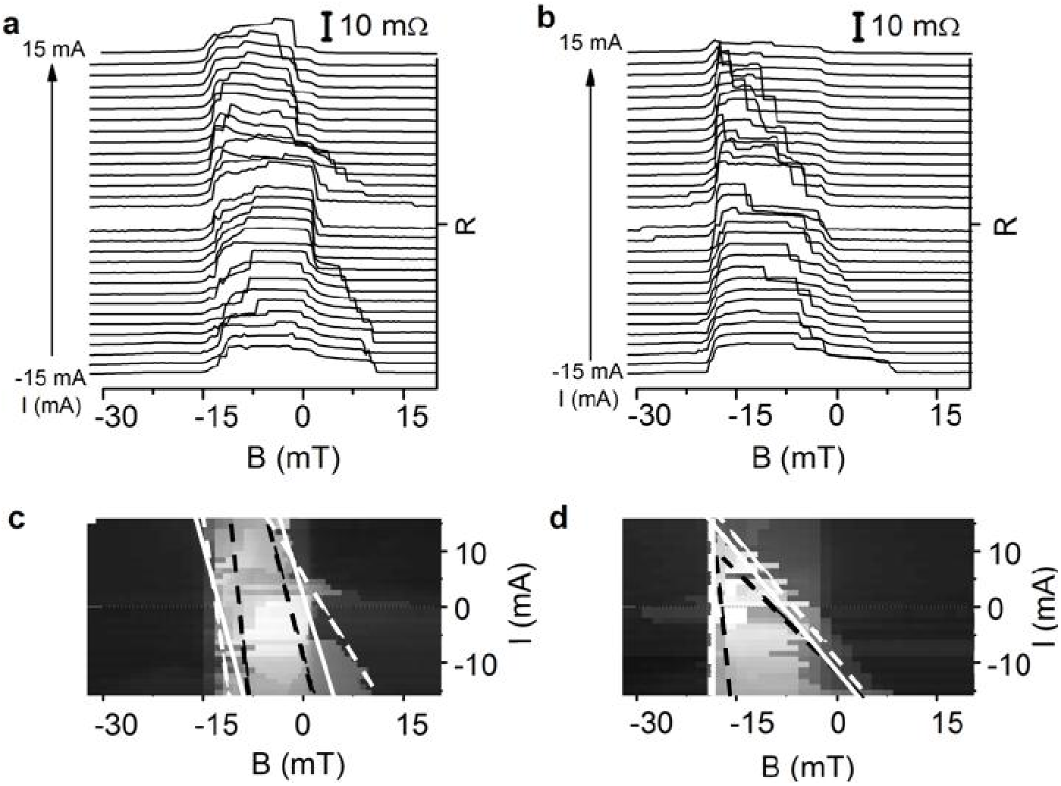

Figure 4.14 (a, b) 3 dimensional (3D) representation of resistance R(B) hysteresis curves for various applied currents I, for an 1.5 Ω point contact to a FeMn(8)/Py(10)/Cu(10)/Py(3) EBSV. The vertical scale size of 10 mΩ is indicated. Curve (b) is a ‘down’ sweep (from large +B to large –B). Curve (a) is an ‘up’ sweep (from large –B to large +B). (c, d) 2D grey scale plots of the R data of Figure 4.14a, b with white = maximum R (AP state) and black = minimum R (P state). The dashed white (30%), solid white (50%) and dashed black (70%) lines represent linear fits to the data at the indicated percentage of full scale (100% = R(AP) – R(P)). Curve (c) is for the ‘up’ sweep; curve (d) is for the ‘down’ sweep [24].

are not the same for samples with AFM = FeMn or IrMn, nor for samples with the same AFM but different thicknesses of the ‘free’ and ‘pinned’ F layers. In this section we focus on data for fixed pinned Py thickness of 10 nm. We present data for contacts to: (i) a FeMn(8)/Py(10)/Cu(10)/Py(3) spin-valve sample with a 3 nm thick ‘free’ Py layer; (ii) a FeMn(8)/Py(10)/Cu(10)/Py(10) spin valve with a 10 nm thick ‘free’ Py layer; and (iii) an IrMn(8)/Py(10)/Cu(10)/Py(10) sample with equal Py-layer thicknesses but AFM = IrMn. The data shown are representative of those found for different contact resistances to the same samples.

(i) For an FeMn(8)/Py(10)/Cu(10)/Py(3) EBSV, Figure 4.14 shows both R(B) hysteresis curves (a and b) and 2D grey-scale plots (c and d). Graphs a and c are for B swept 'up' from large - B to large +B; graphs b and d are for B swept 'down'. Contrary to what we saw with CoFe, in all four graphs, the current has relatively little effect on the pinned layer, but larger effect on the 'free' layer. In b and d, +I moves the 30%,50%, and 70% lines for the free Py layer toward more negative field and -I moves it to more positive field. But -I also broadens the transition in a way that complicates the picture. Graphs a and c show similar, but less dramatic, changes for the free layer, again complicated somewhat by broadening for -I.

(ii) An FeMn(8)/Py(10)/Cu(10)/Py(10) EBSV gives a completely different behavior of R(B) as a function of I, as illustrated in 2D grey scale plots in Figure 4.15. The applied current I now affects reversals of both the 'free' and 'pinned' layers, but the effect looks to be roughly symmetrical in I. White lines in Fig. 6 indicate now only the 50% least-squares linear fits taken independently for pinned and free Py layers for +I and -I.

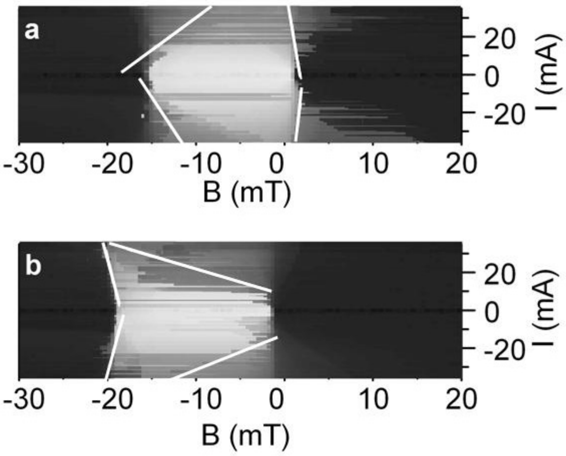

Figure 4.15 2D grey scale plots of R(B) hysteresis data vs I, for a 2.76 Ω point contact to a FeMn(8)/ Py(10)/ Cu(10)/ Py(10) EBSV. The solid white lines represent linear fits to the data at 50% of full scale taken independently for +I and -I. (a) 'up' sweep. (b) 'down' sweep, as defined in Figure 4.14 [24].

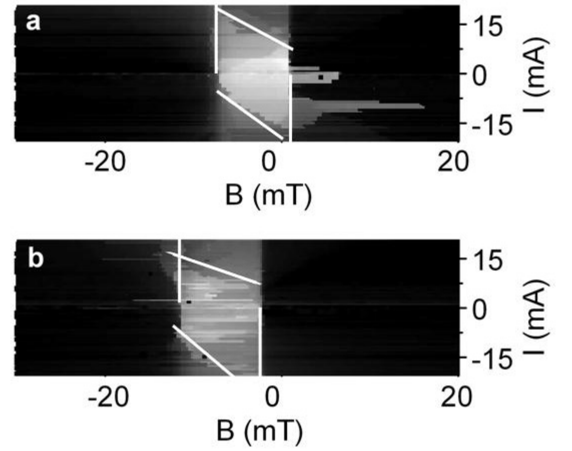

Figure 4.16 2D grey scale plots of R(B) hysteresis data vs I, for a 2.5 Ω point contact to a IrMn(8)/ Py(10)/ Cu(10)/ Py(10) EBSV. The solid white lines represent linear fits at 50% of full scale taken independently for +I and -I. (a) 'up' sweep. (b) 'down' sweep, as defined in Figure 4.14 [24].

(iii) An IrMn(8)/Py(10)/Cu(10)/Py(10) spin valve gives still different behavior, as illustrated in an R(B) 2D grey-scale plot in Figure 4.16. Now, the free layer is unaffected by -I, but +I moves the reversal to more negative fields. In contrast, the pinned layer is unaffected by +I, but -I moves the reversal to smaller negative fields. Again white lines show only the 50% least-squares linear fits taken independently for pinned and free Py layers for +I and –I.

Because the AFM/Py/Cu/Py data neither behave like the AFM/CoFe/Cu/CoFe data, nor behave similarly for AFM=FeMn and AFM=IrMn, and are not independent of the 'free' Py layer thickness, it is clear that the simple assumptions used to explain AFM/CoFe/Cu/CoFe are insufficient. The presence of effects with Py on both the 'pinned' and 'free' F-layers suggests that, unlike AFM/CoFe/Cu/CoFe, the AFM/Py/Cu/Py samples may involve strong enough STT interactions between the two F layers to affect reversals of both. The simplified picture for how the regular ferromagnetic STT and antiferromagnetic STT would affect the pinned and free F layers switching is shown in Figure 4.17. As illustrated in Figure 4.8, for pinned layer switching, the regular ferromagnetic STT favors the antiparallel state at positive

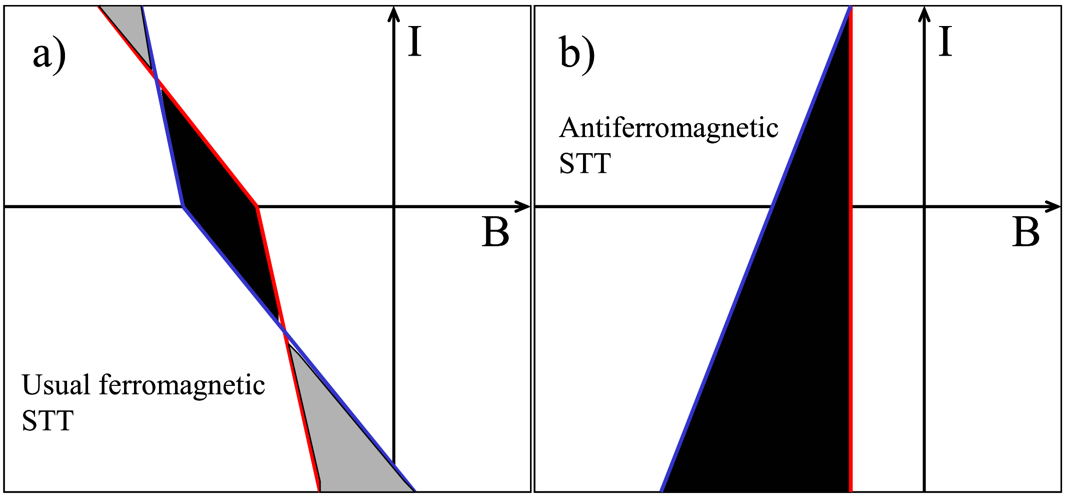

Figure 4.17 Simplified diagram for effects on pinned layer (blue line) and free layer (red line) switching by (a) usual ferromagnetic STT and (b) antiferromagnetic STT. Black and white regions are the high magnetoresistance (antiparallel) and low magnetoresistance (parallel) states. Grey region is the region corresponds to a parallel state stabilized by high current.

current and parallel state at negative state. This means the pinned layer switching would occur at lower (more negative) /higher (less negative) fields for positive /negative currents (blue line in Figure 4.17). We assume the ferromagnetic STT on pinned F layer at positive currents is generated by electrons reflected from another F which, if reflection is not perfect, will be weaker compared to that produced by the transmitted electrons, therefore the current effect (slope in B(I) phase diagram) is less pronounced at positive currents. In contrast, the positive/negative currents induce ferromagnetic STT on free layer and favor parallel/antiparallel states. So the positive current decreases the free layer switching field and negative increases it. The black region is the high magnetoresistance (antiparallel) state. All other regions are the low magnetoresistance (parallel) state. Particularly, the grey region is the superposition where the current induced STT is high enough to stabilize the two F layers at parallel state. The corresponding picture for only antiferromagnetic STT is simplified by assuming the linear dependence of exchange bias (equivalent to pinned layer switching) on the current. The free layer is far away from AFM and not affected here. In most of our experiments with F=Py, the STT from F and AFM are superimposed. As a result, it’s hard to systematize the behaviors in the three samples with Py, which portends the need for a more complex explanation. In particular, the linear behaviors that we've assumed for analyses are oversimplified, with data on more samples likely to lead to changes in the analysis assumptions. For these reasons, we feel it appropriate to be cautious in trying to interpret in any simple way the full range of data in Figures 4.12-4.16. We, thus, end this section by simply describing some potential contributions that will have to be considered in interpreting more complete data.

(1) Mutual effects of STT acting on both F-layers – the ‘pinned’ and ‘free’ layers. As noted above, these STT effects alone should tend to induce opposite changes in the reversal of the ‘pinned’ F to those seen with CoFe. From the perspective of the Slonczewski and subsequent diffusive theories of spin-torque, Py and CoFe have generally similar transport parameters [25, 26]. So we’d expect the STTs themselves to be similar for given layer thicknesses of CoFe and Py. However, CoFe and Py have magnetic differences, such as Py’s much smaller values of both coercivity and magnetocrystalline anisotropy, which can affect the reversal process.

(2) STT acting on the AFM layers, which were proposed in Ref. [9] to explain the observed (assumed linear) variations in exchange-bias of the ‘pinned’ layer. To first approximation, we’d expect such STT to be independent of the F-metal. However its effects could differ due to potential differences in domain structures in either the AFM, F, or both. Also, for an IrMn/Py interface, the majority metals on both sides are Mn and Ni. Intermixing of Mn and Ni across the interface could add still another AFM (i.e., NiMn) to the mix, further complicating the problem. Such effects can also not be completely ruled out with FeMn, where the Mn is 50%.

(3) Heating effects due to the large values of the injected currents. Such effects might be the source (or at least one of the sources) of the broadening seen in several of the figures above.

(4) The response of different 'free' F-layers could also be affected by formation of different magnetic domain structures and different domain sizes in both the F- and AFM-layers, as well as by different abilities of domain walls to move under the action of STT.

4.3.4 Summary

Following predictions that strong current densities could produce spin-transfer-torque (STT)-like effects on antiferromagnets (AFMs) [4-8] we made an attempt to observe such effects in exchange-biased spin valves (EBSVs). Our original observation [9] of the current-dependent exchange bias at a FeMn/CoFe interface was proposed as the first evidence of effects of the current on the AFM. We now confirmed those observations with a new AFM material – IrMn. We also started to extend our studies to a new F = Py. With Py, we sometimes see, for the first time, the effect of current on both the AFM/F and the 'free' F components of the EBSVs. Unfortunately, the complexity of our system and data now available makes it difficult to elucidate partial contributions from phenomena of interest. We are, thus, limited to suggesting several possibilities that will have to be examined via more complete data sets, and concluding that further studies are still needed to elucidate the dependence of these spin-transfer effects on metal combinations and layer thicknesses.

4.4 Point Contact Search for Antiferromagnetic Giant Magnetoresistance

We report the first measurements of effects of large current densities on current-perpendicular-to-plane (CPP) magnetoresistance (MR) of magnetic multilayers containing two antiferromagnetic layers separated by a non-magnetic layer. These measurements were intended to search for a recently predicted antiferromagnetic giant magnetoresistance (AGMR) similar to GMR seen in multilayers containing two ferromagnetic layers separated by a non-magnetic layer. We report on MR measurements for current injected from point contacts into sandwiches containing different combinations of layers of F = CoFe and AFM = FeMn. In addition to: AFM/N/AFM, F/AFM/N/AFM, and F/AFM/N/AFM/F structures, initial results led us to examine also AFM/F/N/AFM, F/AFM, and single F- and AFM-layer structures. At low currents, no MR was observed in any samples, and no MR was observed at any current densities in samples containing only AFMs. Together, these results indicate that no AGMR is present in these samples. In samples containing F-layers, high current densities sometimes produced a small positive MR – largest resistance at high fields. For a given contact resistance, this MR was usually larger for thicker F-layers, and for a given current, it was usually larger for larger contact resistances (smaller contacts). We tentatively attribute this positive MR to suppression at high currents of spin accumulation induced around and within the F-layers.

4.4.1 Introduction

Giant Magnetoresistance (GMR) in ferromagnetic/nonmagnetic (F/N) multilayers has been a focus of intensive study for two decades, both for interesting fundamental physics [27, 28] and important industrial applications [29], e.g., read-heads and magnetic memory. In the simplest case, GMR refers to a large change in resistance of an F/N/F trilayer when the relative orientation of the magnetizations of the two F-layers changes from anti-parallel (AP) to parallel (P). Recently a similar effect — antiferromagnetic (AFM) GMR = AGMR — was predicted in structures where F-layers are replaced by AFMs [4]. By calculating the spin transmission and reflection matrices of an antiferromagnet, Ref. [4] concluded that for unpolarized incoming current, the transmitted current will be still unpolarized, while the reflected current will be spin polarized along the antiferromagnet order parameter direction. Therefore in the system contain two AFMs: AFM/N/AFM, the multiple reflection process at each AFM/N interface will lead to a nontrivial spin current configuration which is the origin of AGMR. The magnitude of AGMR depends on the orientation of the layers opposite the N spacer in the usual way, i.e., the resistance is highest for relative angle $\theta=\pi$ and lowest for $\theta=0$. It was also predicted that a large enough current density passed through an AFM/N/AFM trilayer could change the relative orientation of their magnetizations — AFM spin-transfer-torque (STT) effect — like STT in F/N/F structures. Motivated by these predictions, we initiated a search for magnetoresistive and current-induced effects in systems involving two AFM = FeMn = $Fe_{0.5}Mn_{0.5}$ layers separated by a nonmagnetic N=Cu spacer. The predictions were made assuming ballistic transport in perfectly ordered samples. Our experiments are, thus, crucial to see if the effects predicted for idealized 1-dimensional (1D) AFMs can be seen in real samples with diffusive transport and disorder.

4.4.2 Experiment

Our multilayers are sputtered on Si substrates using sputtering system. All samples had a 50nm thick Cu underlayer to secure a closely CPP current flow, and a 5nm thick Au capping layer to avoid surface oxidation. The point contacts were made with a standard system described in Chapter 2.2. In F/N/F trilayers, the relative orientation of the magnetizations of the two Fs is controlled by an externally applied magnetic field B. To achieve well-defined AP and P states, the moment of one of the F-layers is often ‘pinned’, via exchange coupling (exchange bias) to an adjacent AFM layer, leaving the moment of the other free to reverse in much smaller B. In a simple AFM/N/AFM sample, just applying a field B is not expected to be efficient, due to the weak effect of external fields on magnetic moments in AFMs. To achieve better control of the AFMs, we also studied AFM/N/AFM layers sandwiched between two F layers to give F/AFM/N/AFM/F, with the two AFM layers differently exchange coupled to their respective F-neighbors. Applying a magnetic field to change the magnetic order of the F-layers should then also affect the order of the AFM layers. If a large current density is sent through any of these multilayer samples, spin-transfer-torque (STT) interactions between Fs and between AFMs might also affect the AFM magnetic order [4, 9]. Finally to isolate the MR observations of interest from potential spurious effects, we tested a wide variety of structures: AFM/N/AFM, F/AFM/N/AFM, F/AFM/N/AFM/F, AFM/F/N/AFM, F/AFM, and single F- and AFM-layers. All films used N=10nm of Cu, AFM=3 or 8nm of FeMn, and F=2,3,4,6, or 10nm of CoFe=$Co_{91}Fe_9$ to give different magnitudes of exchange bias at the AFM/F interfaces and to look for any thickness dependence. All possible combinations of AFMs (3/N/3. 3/N/8, 8/N/3, 8/N/8) were tested. To induce exchange bias at the F/AFM interfaces, the samples were cooled from ~463K through the Néel temperature of FeMn ($T_N \approx 400K$) in the presence of a static magnetic field (~18mT). All layer thickness are given in nm, and negative current corresponds to electrons flowing from the tip into the multilayer. We measure the sample magnetizations using a commercial, Quantum Design MPMS, SQUID (Superconducting Quantum Interference Device) magnetometer. We also measure the standard magnetoresistance curves at different bias currents.

4.4.3 Experimental Results

Figure 4.18 shows typical, room temperature, magnetization versus field (M vs B) data for sample CoFe(10)/FeMn(8)/Cu(10)/FeMn(8)/CoFe(3). The curves show reversals of the 10 nm and 3 nm thick CoFe layer magnetizations with small hystereses, shifted by exchange-bias to be centered at about 10 and 30 mT. The higher field to reverse the 3 nm thick CoFe layer shows the expected stronger exchange bias for a thinner F-layer [30, 31]. Such measurements give the change in order of the F layer magnetizations, but no direct information about order changes in the AFM layers.

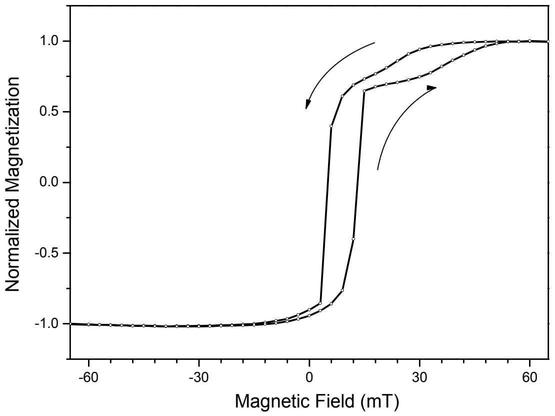

Figure 4.18 Magnetization versus magnetic field at room temperature for sample CoFe(10)/FeMn(8)/Cu(10)/FeMn(8)/CoFe(3), with layer thickness in nm.

Neither standard current-in-plane (CIP) MR measurements on our multilayer films, nor CPP MR measurements with point contacts, showed any MRs for sample of the form AFM/N/AFM and F/AFM/N/AFM with F layer thickness of only 3nm. As shown in Figure 4.19, measurement of point contact resistance R=V/I vs applied field B for a series of current I applied through a 1.3Ω contact to a sample of the form

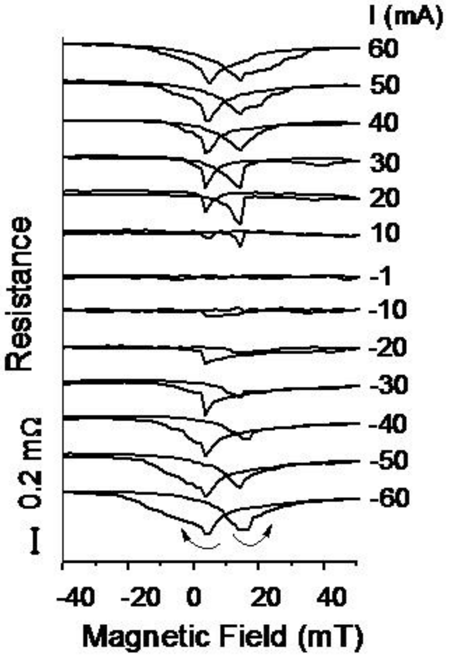

Figure 4.19 Point-contact magnetoresistance at different bias currents for a 1.3Ω point contact to sample CoFe(10)/FeMn(8)/Cu(10)/FeMn(8)/CoFe(3). Solid traces show point-contact resistance R=V/I versus applied magnetic field B for a series of bias currents I = -60 to +60 mA. Arrows indicate up and down B-sweeps. I = 60 mA corresponds to current density $j \sim 7\times10^{12}$ A/m^2. Note that a nonzero magnetoresistance appears only at high bias currents.

CoFe(10)/FeMn(8)/Cu(10)/FeMn(8)/CoFe(3) also showed no MR when I was small. However, for high I (both positive and negative), small, positive MRs appear and grow in magnitude with increasing I (sometimes tending toward saturation in magnitude above a certain value of I). For the sweeps shown, starting from high positive field, R(B) is constant at a maximum value, decreases to a minimum at B ~ 5 mT, and then grows again to its maximum value at high negative field. The reversed sweeps from high negative to high positive fields show similar behavior with minimum R(B) at about 15 mT. Note that higher fields are needed to saturate R at higher bias currents. To illustrate the last point Figure 4.20 shows 2D gray-scale plots

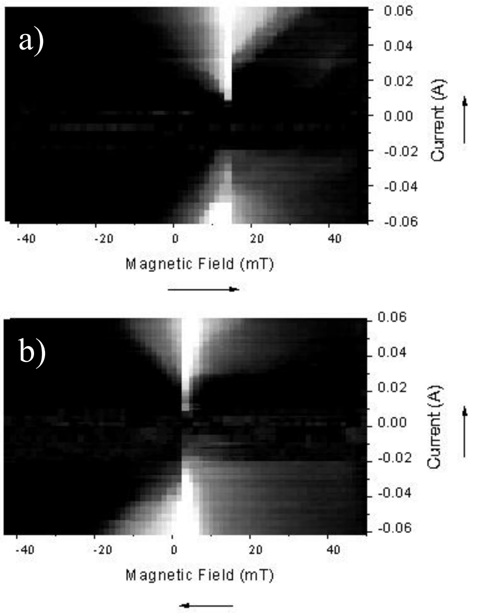

Figure 4.20 Current-dependent magnetoresistance in antiferromagnetic spin valve. 2D gray-scale plot representations of up (a) and down (b) sweeps from Figure 4.19 for CoFe10nm/ FeMn8nm/ Cu10nm/ FeMn8nm/ CoFe3nm sandwich. Lighter color indicates lower resistance with white/black corresponding to 1.292/1.3Ω. The current was stepped up from high negative values as indicated by arrows.

of separate up and down field sweeps for the data in Figure 4.19. Here lighter color indicates lower resistance. Arrows next to the axes indicate the directions for field- and current-sweeps. The field regions in which the MRs occur in Figure 4.19 correlate with those for magnetization reversals in Figure 4.18.

Similar small spin-valve MR signals (~0.02-0.12%) were seen in 28 contacts (R ranging from 0.6-3.5Ω) to F1/AFM/N/AFM/F2 type samples with 10nm thick F1 and 3nm thick F2. Values of the maximum change in contract resistance ΔR = R(max) – R(min), taken for down sweeps at I = +30 mA, are plotted vs saturation R in Figure 4.21 (open symbols) for contacts to all different samples of type F1/AFM/N/AFM/F2 — designated via F1/F2=10/3 and AFM/AFM thicknesses: 8/8, 3/3, 8/3, and 3/8.

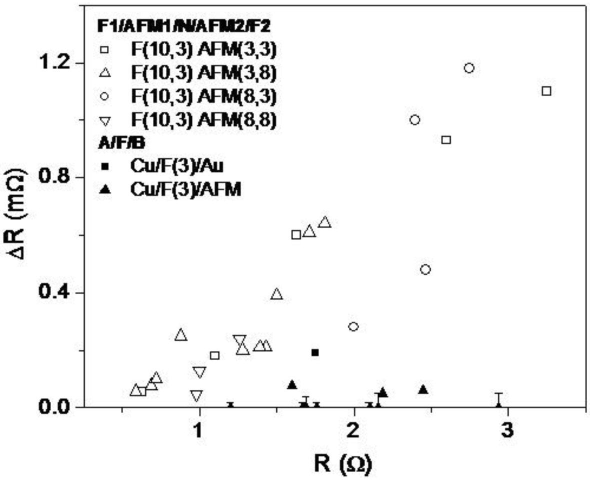

Figure 4.21 The maximum change in resistance, ΔR, versus point contact resistance, R, at saturation, recorded at I = 30 mA for down-sweeps. Open symbols show data for four different samples of type F1/AFM1/N/AFM2/F2. The legend indicates the thicknesses of the two F (F1, F2) and two AFM (AFM1, AFM2) layers in nanometers. Note that error bars are smaller than symbol sizes. For comparison, filled symbols show data for samples with a single 3 nm thick F layer sandwiched between Cu and Au layers (filled squares) or between Cu and AFM layers (filled triangles).

Overall, ΔR for a given I increases with the increasing contact resistance (decreasing contact size), and similar values of ΔR are seen for samples with different AFM thicknesses. In contrast, only one of six contacts to sample of type F1/AFM/N/AFM/F2 with both F1 and F2 =3 nm thick showed a positive MR comparable with that found in samples with at least one F(10 nm) layer. The other five contacts all produced data points below the distribution shown in Figure 4.21 with open symbols. This observation suggests that the observed MR might be associated with single F(10 nm) layers in our samples. To check this possibility, we measured an extensive number of samples that include only one F layer each (either 3 or 10 nm thick) sandwiched between Au, Cu, or AFM layers, sometimes with an extra AFM layer: AFM/F/N/AFM, F/AFM/N/AFM, N/F/AFM, and N/F/N. Figure 4.21

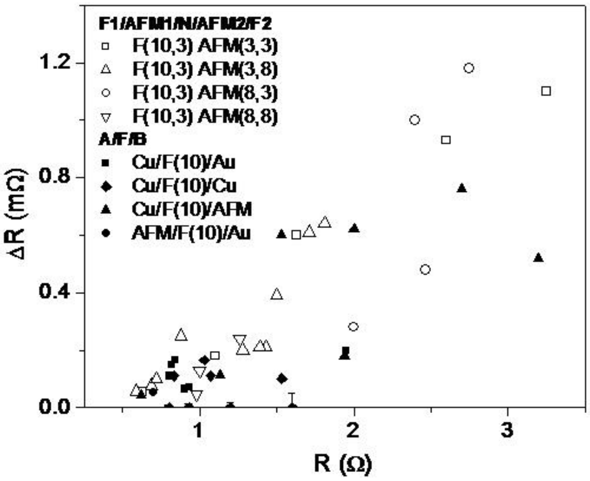

Figure 4.22 The maximum change in resistance, ΔR, versus point contact resistance, R, at saturation, recorded at I = 30 mA for down-sweeps. Open symbols show the same data for F1/AFM1/N/AFM2/F2 samples as in Fig. 2. Filled symbols show data for samples with a single 10 nm thick F layer sandwiched between Cu and Au (filled squares), Cu and Cu (filled diamonds), Cu and AFM (filled triangles), AFM and Au (filled circles). Note that error bars are smaller than symbol sizes.

(filled symbols) shows that, with one exception, contacts to samples with only one F=3 nm layer gave MRs much smaller than those for the open symbols. In contrast, Figure 4.22 shows that most contacts to samples with one F=10 nm layer (filled symbols) gave positive MRs comparable in magnitude to those of the open symbols.

4.4.4 Summary and Discussion

To summarize: (i) we observe small positive MRs (resistance is highest at saturation) in samples of type F/AFM/N/AFM/F when at least one of the Fs is 10 nm thick; (ii) the MR is present only at high current densities flowing across such multilayers (no MR at small currents); (iii) only one out of six contacts to a sample with two 3 nm thick F-layers showed comparable MR; (iv) samples of types

AFM/F/N/AFM, F/AFM/N/AFM, N/F/AFM, or N/F/N with only one F=3 nm show no MR (with exception of only one contact), but similar samples with F=10 nm show (in most cases) MRs comparable to those in (i).

The positive MR in Figure 4.19 cannot be standard GMR between the two outer F-layers, which must be negative (smallest R at large B). The absence of MR in F(3)/AFM/N/AFM samples also rules out anisotropic MR, which is independent of F-layer thickness. The observation of MR in F/AFM/N/AFM/F samples might be tentatively attributed to the AGMR predicted in Ref. [4]. In support, are a correlation of MR-shape with SQUID-measured magnetizations of our samples (not shown) and the need for high currents to change the AFM order parameters [4, 9]. However, the presence of similar MRs in samples with only a single F(10 nm) layer (no AFMs) suggests that the MR is more likely associated with Fs in our multilayers. Small positive MRs were previously seen in nanopillars of single F=Permalloy layers [32]. There they were associated with suppression at high currents of spin accumulation induced around and within the F-layer. At high Bs, the magnetization of F is uniform and the pillar resistance is higher due to an extra contribution from spin accumulation [32, 33]. Near zero B, however, the Oersted field of the applied current produces a vortex in F on a scale comparable to the spin diffusion length. This non-uniform magnetization suppresses the spin accumulation, decreasing the pillar resistance. A similar mechanism may be responsible for the positive MRs of our multilayers. If so, this would be the first evidence for such behavior in extended layers.

4.5 References

[1] L. Berger, *Phys. Rev. B* **54**, 9353 (1996)

[2] J. C. Slonczewski, *J. Magn. Magn. Mater.* **195**, L261 (1999)

[3] D. C. Ralph, and M. D. Stiles, *J. Magn. Magn. Mater.* **320**, 1190 (2008)

[4] A. S. Núñez, R. A. Duine, P. Haney, and A. H. MacDonald, *Phys. Rev. B* **73**, 214426 (2006)

[5] P. Haney, D. Waldron, R. A. Duine, A. S. Núñez, H. Guo, and A. H. MacDonald, *Phys. Rev.* B **75**, 114428 (2007)

[6] P. Haney, and A. H. MacDonald, *Phys. Rev. Lett.* **100**, 196801 (2008)

[7] Y. Xu, S. Wang, and K. Xia, *Phys. Rev. Lett.* **100**, 226602 (2008)

[8] H. Gomonay, V. M. Loktev, arXiv:0709.4172

[9] Z. Wei, A. Sharma, A. S. Nunez, P. M. Haney, R. A. Duine, J. Bass, A. H. MacDonald, and M. Tsoi, *Phys. Rev. Lett.* **98**, 116603 (2007)

[10] S. Urazhdin, and N. Anthony, *Phys. Rev. Lett,* **99**, 046602 (2007)

[11] X-L. Tang, H-W. Zhang, H. Su, Z-Y. Zhong, and Y-L. Jing, *Appl. Phys. Lett.* **91**, 122504 (2007)

[12] N. V. Dai, N. C. Thuan, L. V. Hong, N. X. Phuc, Y. P. Lee, S. A. Wolf, and D. N. H. Nam, Phys. Rev. B **77**, 132406 (2008)

[13] B. Dieny, V. S. Speriosu, S. S. P. Parkin, B. A. Gurney, D. R. Wilhoit, and D. Mauri, *Phys. Rev. B* **43**, 1297 (1991)

[14] W. H. Meiklejohn, and C. P. Bean, *Phys. Rev.* **102**, 1413 (1956)

[15] J. Bass, A. Sharma, Z. Wei, M. Tsoi, *J. of Magnetics* (Korean Magnetic Society) **13**(1), 1 (2008)

[16] A. Chaiken, G. A. Prinz, and J. J. Krebs, *J. Appl. Phys.* **67**, 4892 (1990)

[17] Paul Haney, Ph.D Thesis, The University of Texas at Austin, (2007)

[18] A. Scholl, M. Liberati, E. Arenholz, H. Ohldag, and J. Stöhr, *Phys. Rev. Lett.* **92**, 247201 (2004)

[19] H. Ohldag, A. Scholl, F. Nolting, E. Arenholz, S. Maat, A. T. Young, M. Carey, and J. Stöhr, *Phys. Rev. Lett.* **91**, 017203 (2003)

[20] M. C. Weber, H. Nembach, B. Hillebrands, and J. Fassbender, *J. Appl. Phys.* **97**, 10A701 (2005)

[21] Z. Wei, J. Basset, A. Sharma, J. Bass, and M. Tsoi, to be published on *J. Appl. Phys.* (2009)

[22] G. M. Stocks, W. A. Shelton, T. C. Schulthess, B. Újfalussy, W. H. Butler, and A. Canning, J. Appl. Phys. **91**, 7355 (2002)

[23] A. Sakuma, K. Fukamichi, K. Sasao, and R. Y. Umetsu, Phys. Rev. B **67**, 024420 (2003)

[24] J. Basset, A. Sharma, Z. Wei, J. Bass, and M. Tsoi, *Proc. of SPIE,* **7036**, 703605 (2008)

[25] W. P. Pratt Jr., S. D. Steenwyk, S. Y. Hsu, W. –C. Chiang, A. C. Schaefer, R. Loloee, and J. Bass, *IEEE Trans. Magn*. **33**, 3505 (1997)

[26] A. C. Reilly, W. Park, R. Slater, B. Ouaglal, R. Loloee, W. P. Pratt Jr., and J. Bass,

J. Magn. Magn. Mat. **195**, 269 (1999)

[27] M. N. Baibich, J. M. Broto, A. Fert, F. N. V. Dau, F. Petroff, P. Eitenne, G. Creuzet, A. Friederich, J. Chazelas, *Phys. Rev. Lett.* **61**, 2472 (1988)

[28] G. Binasch, P. Grunberg, F. Saurenbach, W. Zinn, *Phys. Rev. B* **39**, 4828 (1989)

[29] J. M. Daughton, *IEEE Trans. Magn.* **36**, 2773 (2000)

[30] J. Nogués, I. K. Schuller, *J. Magn. Magn. Mater.* **192**, 203 (1999)

[31] A. E. Berkowitz, K. Takano, *J. Magn. Magn. Mater.* **200**, 552 (1999)

[32] S. Urazhdin, C. L. Chien, K. Y. Guslienko, and L. Novozhilova, *Phys. Rev. B* **73**, 054416 (2006)

[33] P.C. van Son, H. van Kempen, and P. Wyder, *Phys. Rev. Lett.* **58**, 2271 (1987)

Vita

Zhen Wei was born in Zhoushan, Zhejiang, China, on March 2, 1980, the son of Min Wei and Suqiu Chen. He received Bachelor of Science degree in Applied Physics from the University of Science and Technology of China in July, 2003. Two months later he entered the Department of Physics of the University of Texas at Austin. In 2004, he began to work with Dr. Maxim Tsoi to study the spin-transfer-torque effect in magnetic multilayers.

Permanent address: 2501 Lake Austin Blvd. Apt N102
Austin, TX 78703

This dissertation was typeset by the author.